UC Berkeley
UC Berkeley Electronic Theses and Dissertations

Title

Interactions of Plasma-Generated Species on Porous Dielectric Thin Films

Permalink

https://escholarship.org/uc/item/9f88p32j

Author

Lee, Joe

Publication Date

2013

Peer reviewed|Thesis/dissertation

Interactions of Plasma-Generated Species on Porous Dielectric Thin Films

by

Joe Lee

A dissertation submitted in partial satisfaction of the

requirements for the degree of

Doctor of Philosophy

in

Chemical and Biomolecular Engineering

in the

Graduate Division

of the

University of California, Berkeley

Committee in charge:

Professor David B. Graves, Chair
Professor Roya Maboudian
Professor Michael A. Lieberman

Spring 2013

Interactions of Plasma-Generated Species on Porous Dielectric Thin Films

Abstract

Interactions of Plasma-Generated Species on Porous Dielectric Thin Films

by

Joe Lee

Doctor of Philosophy in Chemical and Biomolecular Engineering

University of California, Berkeley

Professor David B. Graves, Chair

Low pressure plasma processing is used extensively in the semiconductor industry for modern technology. As a result, the understanding of plasma/material interactions is very important to the improvement and design of materials and treatment methods. This dissertation focuses on the understanding of interactions between individual plasma species and materials that are used in the fabrication of the interconnect in semiconductor devices, namely porous low-*k* dielectrics.

Proper insulation of the metal lines in the interconnect relies on maintaining the integrity of the insulator's dielectric properties. As the features of the interconnect are shifting to smaller dimensions, techniques used to implement lower dielectric permittivity have also lowered the material's resistance to plasma-induced damage. As a result, plasma processing of these materials have become a major challenge for future advances in interconnect technology. This study examines specific species generated from typical plasma discharges and their effect on porous low-*k* materials.

The first part of this dissertation studies the mechanism for photon-induced effects and demonstrates the influence of emission wavelength on carbon removal from carbon-doped oxide films. VUV photons emitted from the plasma were observed to break Si-C bonds. However, oxidizing gas species must be present in the background to cause carbon removal. Depending on gas chemistry, VUV photons of different wavelengths are emitted, which affects the depth of the damage penetration into the film. Shorter wavelength emissions are absorbed by the SiO_2-like damage layer that is produced after carbon extraction, thereby preventing further removal of carbon.

The dissertation continues by examining the effects of photons and radicals individually by isolating the species to obtain separate exposures. By doing so, radicals and photons generated from O_2 plasma were observed to remove carbon in different ways, creating different carbon profiles as a function of depth. 130 nm wavelength photons are fairly transparent through the material, leading to a gradual removal of carbon throughout the modification depth. In contrast, oxygen radicals are diffusion-limited, leading to removal of carbon occurring as a front. Modeling of damage effects by these species was performed in each case, and good predictions of their behavior were obtained. However, direct plasma exposures were observed to behave

differently, exhibiting much less carbon removal than predicted by the model. Further experimentation found evidence that synergy between photon and radical species led to an effective decrease in the diffusivity of the modified material, reducing subsequent plasma damage.

Through fundamental study of plasma/material interactions, the role of photons and radicals in plasma-induced damage has been determined. As a result, treatment methods to reduce plasma damage based on inhibiting these species can be designed. These include plasma filtration techniques, densification by ion bombardment, and the use of plasmas with reducing chemistries. While the scope of this research has focused on interactions with dielectric thin films, these approaches to plasma interactions are relevant to other processes that rely on plasma processing.

To my parents, Katie, and my extended family

Table of Contents

List of Figures

Chapter 1

Chapter 2

Chapter 3

Chapter 4

Chapter 5

Chapter 6

Appendices

List of Tables

Acknowledgements

A great number of people have helped me throughout these past five years at Berkeley, and I feel very blessed to be surrounded by such support both here and everywhere else from friends, family, and colleagues.

First, I would like to thank my advisor, David Graves, for introducing and guiding me through this field of plasma and semiconductor research. Through his guidance, I have grown more as a researcher and developed how to analyze in a systematic manner. The experience I have gained in this lab and the knowledge that he has shared with continue to stay with me as I start my next endeavor.

I would like to thank Monica Titus, Dustin Nest, and Ting Ying Chung, for teaching me everything that I know about the ICP system and beam system. While these equipment are very complicated to deal with and have had their issues, it has been my favorite part of the research. I would also like to thank Dr. John Coburn and Dr. Yuki Sakiyama for their helpful advice on low pressure systems and COMSOL modeling. All the members of the Graves group, both past and present, have been enjoyable to work with and have really made my time in the D level a pleasure.

I would like to thank my collaborators at University of North Texas, Prof. Jeff Kelber, Swayambhu Behara, and Haseeb Kazi, for working together with me to understand the ion effects on low-k. Together, we have achieved goals that could not have been done by ourselves. I would like to thank Steve Volkman and Feng Pan from the Subramanian lab in EECS for letting me use the mercury probe and providing me with oxide deposited samples.

Thanks to all my friends, especially those back in Georgia, who have continued to support me. It's thanks to many of you that I decided on the path to come here. Many of you have gone off onto different paths and are all across the country, but I'm glad we still keep in touch.

Thanks to all my family, who have stood by and watched me grow, however haphazard my decisions may have been. Although my academic career has been a bit difficult to explain to my parents and relatives due to a language barrier, they have supported me enthusiastically anyways, and have done all they could to make my journey possible.

Finally, I would like to especially thank my wife, Katie. As a fellow graduate student that works down the hall, she has been beside me throughout this research and is the first person that I turn to. I am very grateful to have such a partner, both in science and otherwise.

Chapter 1
Introduction

1.1 Plasma and the Semiconductor Industry

In semiconductor processing, the number of transistors continues to double every two years as critical dimensions continue to shrink further and further. This trend, known as Moore's law, has been the roadmap for the semiconductor industry for the past 50 years. Miniaturization of transistors has led to reduced manufacturing costs by allowing more devices to fit onto a single wafer. Furthermore, power consumption is reduced and switching speeds have improved, leading to faster, more efficient processors for consumer needs. Yet, shrinking of critical dimensions to the sub-micron scale has encountered numerous challenges. As a result, the requirements for manufacturing integrated circuits have caused the semiconductor industry to make several large transitions in mainstream production in recent years to maintain this trend.

As metal lines within back-end-of-line (BEOL) interconnects shrink and become more densely-packed, inherent resistivity of the metal and capacitance between the lines become major issues for device optimization. In addition, shrinking the cross-sectional area of metal lines increases electrical resistance, thereby increasing the risk of current leakage. As a result, copper interconnects have replaced aluminum as the standard due to its lower resistivity and excellent electromigration reliability.[1] Given that the consequence of more densely-packed lines is the increase of capacitance in the dielectric layer, the solution has been to replace SiO_2 with materials with a lower dielectric constant (*k*). Most recently, another push in further lowering the dielectric constant has been achieved by the introduction of porosity in these low-*k* dielectric films. During the production of interconnects, plasmas are used for many processes, such as the formation of channels in the dielectric layer for the filling of metal lines and stripping of photoresist. However, these same processes have been known to cause damage to these porous low-*k* materials, drastically reducing their performance. This result presents a serious problem towards the advancement to the next technological node. Therefore, understanding the mechanisms for this damage is crucial to overcoming this barrier. Fundamental studies focusing on the role of individual plasma species are important to understanding how plasma/material interactions occur. Through this understanding, techniques can be engineered to fine tune the plasma and obtain optimized results when manufacturing high-quality, low cost devices.

1.2   Interlayer Dielectric and the Damascene Process

Interconnects are a series of metal lines that carry electrical current throughout the components of an integrated circuit. Presently, copper is used to form these interconnects, which are separated by an insulating layer composed of a dielectric material. In the past, aluminum interconnects were formed by etching the metal and depositing oxide in between the lines. Due to the difficulty of etching copper efficiently, a new process was needed to form copper-based metal lines, called the 'damascene process'.[2] This process involves etching of the interlayer dielectric and deposition of the metal afterwards. The initial steps are outlined in figure 1.1 to prepare the interlayer dielectric for the filling of metal lines. Photoresist is first deposited on top of the dielectric film, and using a mask, specific patterns are formed by the selective decomposition of exposed areas by ultraviolet radiation. Radiated areas are then removed by a basic solution. Anisotropic etching of the underlying dielectric layer is carried out using plasma processing. The photoresist is then stripped off, typically with O_2 plasma, before the channel is filled with copper. Many repetitions of this process are required to generate the network of metal lines that complete the BEOL interconnect.
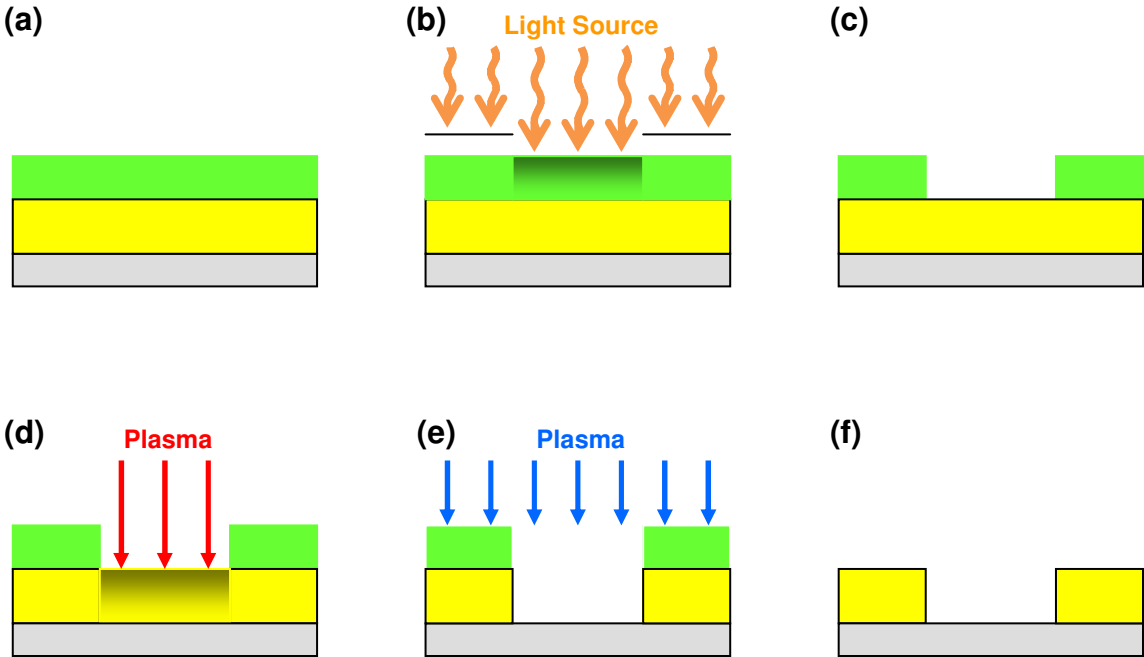
Figure 1.1   Pattern transfer using optical lithography. (a) Coating of photoresist. (b, c) Photoresist exposure through a mask and resulting pattern transfer. (d) Anisotropic etching of dielectric layer using plasma processing. (e, f) Removal of photoresist using a plasma and resulting pattern in dielectric layer.

Because the dielectric layer undergoes numerous exposures, a material with suitable properties is necessary for the fabrication of this device. In the past, SiO_2 ($k = 3.9$) was the main dielectric material due to its strong mechanical strength, chemical stability, and ease of deposition, but the miniaturization of interconnects has made this material obsolete. The characteristic time for the switching of current within interconnects is proportional to the capacitance of the dielectric layer. The capacitance can be expressed as

$$C = A \, \varepsilon_0 \, k \, / \, d \qquad\qquad (1.1)$$

where C is the capacitance of the dielectric layer, A and d are the contact area and thickness of the dielectric layer between the metal lines respectively, ε_0 is the permittivity of free space, and k is the dielectric constant. As the dimensions of the interconnect shrink, the capacitance and consequently the characteristic time increases. Materials with an inherently lower dielectric constant were subsequently developed to replace SiO_2.

The dielectric constant can be seen as how well a material can hold a charge and is dependent on the contribution of electronic, ionic, and dipolar polarization. Electronic polarization describes the movement of the electron cloud under an applied electric field. Ionic polarization relates the distortion of the nuclei between an ionic bond and the electric field, causing bonds to stretch or compress. The permanent electric dipole moments of a molecule make up the dipolar polarization. Therefore, in order to lower the dielectric constant of a material, reduction of polar/polarizable molecules, ionic bonds, or electron density is needed.[3,4]

Si-O-Si Network   **Si-O-Si Cage**
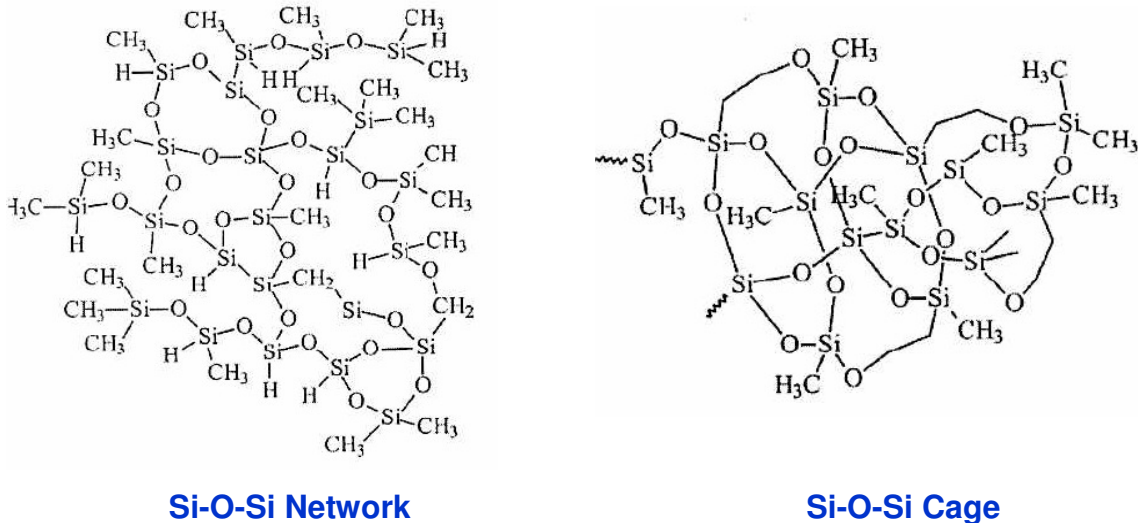
Figure 1.2 Si-O-Si network and cage structures resulting from cross-linking Si-O and Si-CH$_x$ structures. Many of the carbon compounds remain as terminating CH_3 groups.[5]

3

As a result, industry has turned to the incorporation of bonds with lower electronic polarizability that can also open the silica network to decrease density, producing a new line of "low-k" materials. SiOCH, a low-k material containing methylated species in a silica network, has received much attention as an alternative to SiO_2. The incorporation of bulky methyl groups does an excellent job in reducing the dielectric constant, but with a tradeoff. The mechanical strength and chemical stability of the organosilicate material stem from the dense tetrahedral Si-O structures. By substituting oxygen with methyl compounds in a portion of these structures, linear Si-O structures are formed with the presence of terminating –CH_3 groups. As a result, the material is now more susceptible to chemical attack and mechanical deformation due to lower bond strengths. However, the methylated structures can be cross-linked and organized into a Si-O-Si network or cage structure (Fig. 1.2) to reduce the Si-O density without majorly impacting the mechanical strength.[3,6]

To further drive down the dielectric constant, the introduction of additional free volume in the material through the use of porogens has been implemented with these organosilicate materials. While the introduction of the Si-O-Si network and cage structures inherently creates a small amount of porosity, typically the pores are isolated and less than 1 nm in size, called "closed porosity." Porogens used to create additional free volume are typically either chemically linked to the molecular network of the material or blended into a solution with the deposition precursor. The porogens are then decomposed thermally or by ultraviolet radiation and removed from the film, leaving much larger pores.[7] Through this method, porosities as high as 40% can be achieved, yet this results in high interconnectivity of the pores, called "open porosity." These "open" pores allow for easy diffusion of large molecules into the material, presenting large problems for integrated circuit production, such as plasma processing.

1.3   Plasma Discharges and Effect on Low-k

A plasma discharge is created by a gas that is electrically stimulated such that free electrons are heated well above room temperature, resulting in collisions between electrons and neutral gas species. The creation of ion and radical species at near room temperature is the direct result of these collisions. The semiconductor industry focuses more on partially-ionized plasmas in which the electron and ion density is low compared to neutral gas species.[8] Typically, the ion and radical densities are orders of magnitude lower than the neutral gas density. Inductively-coupled plasmas, used in this research, are usually generated under high vacuum in an etching system by feeding power into a gas. This power is delivered through a radio-frequency (RF) current from coils at the top of the chamber and is present to maintain the source of energetic electrons used to excite other gas species.

The unique processing ability of a partially-ionized plasma comes from its interaction with surrounding surfaces. An electric potential exists at the plasma-surface interface that contains the more mobile species, known as a "sheath." This sheath acts to keep the bulk of the plasma quasi-neutral by balancing the charges between the electrons and ions. A unique feature of inductively-coupled plasmas is the ability to separately control the ion energies. By applying a bias voltage to a sample of the material, typically a few hundred volts, plasma ions can be accelerated across the sheath region, leading to ion bombardment perpendicular to the surface.

Material is removed anisotropically due to directionality of the ions as shown in Figure 1.3. In comparison, wet etching techniques using chemicals result in poor pattern transfer known as "undercutting."
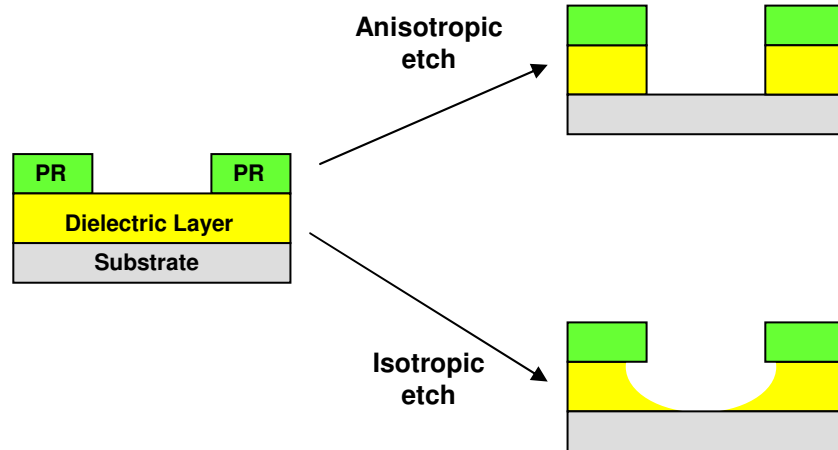
Figure 1.3. Comparison of etch profiles after anisotropic and isotropic etching.

While high energy ions are beneficial for etching small dimensions, many other species from the plasma are also present. A large amount of radical species and vacuum ultraviolet radiation (VUV, λ < 200 nm) is produced from low-pressure plasmas.[9] These species exhibit isotropic behavior, leading to deformation of patterns similar to that observed in wet etch techniques. VUV photons are primarily generated by electron impact excitation of neutral species. These photons may be reabsorbed, re-emitted, quenched, or interact with surfaces.[10] Furthermore, the type of gas chemistry and the plasma parameters, such as power and pressure, greatly influence the type and level of emissions that are generated. In the case of VUV photons, the wavelength of emissions is determined by the gas chemistry and how the gas atoms return back to ground state from an excited state. Reactive radical intermediates also interact differently with material substrates depending on the gas molecule and level of dissociation. Often in semiconductor processing, mixtures of different gases are tailored to obtain specific results, so the interactions within the plasma become extremely complex and difficult to characterize.

This collective mixture of ions, electrons, radicals, photons, and neutral molecules that make up a typical plasma discharge has been seen to cause damage to organosilicate low-k materials, presenting serious problems for the semiconductor industry as plasma processing is used for etching, stripping, adhesion promotion and cleaning. Typical findings from these studies show that after plasma exposure, a loss of hydrophobic methylated species occurs leading to post-exposure adsorption of water vapor. Water vapor (k = 80) has a drastic effect on the electric performance of integrated circuits. Furthermore, the methylated species are potentially replaced by hydrophyllic hydroxyl groups, causing irreversible damage to the material.[11-19] These issues are fairly well-known in the semiconductor industry and much effort has been spent in recent years to understand why this damage occurs and how to minimize it.

1.4   Plasma Species Separation

Many studies in the past have attempted to identify the source of the damage by varying plasma conditions. Some parameters such as gas chemistry, pressure, exposure time, and bias power can be tuned in order to obtain more desirable effects. However, plasma discharges are complex in nature and remain very difficult to fully understand. Due to the multitude of interactions occurring simultaneously, attributing mechanisms of damage to the specific components of the plasma remains a considerable task. From various studies, oxygen-containing plasmas have been suspected to cause damage by oxidation of methylated species, thus studies have turned to plasmas using less reactive gases (H_2, N_2, and NH_3).[20-25] Results from these plasma chemistries have been conflicting, possibly due to a limited ability in characterizing the conditions of these discharges. While the choice of plasma chemistry appears to have an impact on the extent of damage and water adsorption, even plasmas composed of chemically neutral species such as argon have been shown to affect low-*k* materials, so factors other than gas chemistry appear to play a major role.[26-28]

In recent years, studies focusing on the separation of plasma components have shown progress in revealing the effects of individual species on various materials. Using various techniques, exposed samples are shielded from particular species coming from the plasma. However, many of these studies mainly focus on the role of ion bombardment and radical attack of low-*k* materials.[29-34] However, VUV photons have been shown to break down small amounts of organic impurities in SiO_2 films during photochemical treatments.[35] Low-*k* films that are doped with methyl species can similarly be photolyzed, resulting in the creation of an electron-hole pair that becomes a Si dangling bond. These dangling bonds can interact with H_2O to form silanol, making the material more hydrophyllic.[36] Similar mechanisms have been reported to occur in gate oxide films with photon energies greater than 8.8 eV.[9,37-38] Taking these points into consideration, the photon effects cannot be ignored like they have been in the past. These studies show the importance and potential of characterizing the effects of individual species in a plasma discharge. By doing so, a better understanding of how damage occurs can lead to more efficient methods to achieve the processing requirements needed for future technology nodes. Examination of individual plasma species and their effects will be performed in two separate systems: a vacuum beam system and an inductively-coupled plasma chamber.

1.4.1   Vacuum Beam System Studies

Studying plasma-surface interactions in a plasma chamber is very difficult. In addition to the components in a plasma discharge, etch products may become part of the discharge and change the plasma chemistry. These new products may then inadvertently interact with the substrate as ions or radicals. A high vacuum beam system allows the study of various types of exposures in a controlled environment. Well-characterized sources of beams (VUV photons and ions) can be designed in a way that their stability is not affected by reaction products, which allows for the study of plasma species in a decoupled environment. A summary of the difference between the two systems is shown in figure 1.4. The specific setups for each system will be further explained in the Experimental Setup section in Chapter 2.
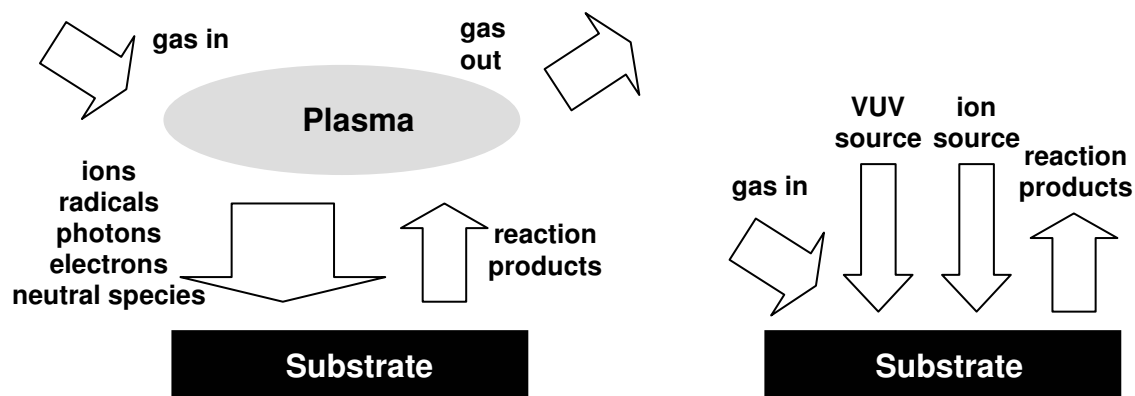
Figure 1.4. Schematic of a plasma discharge (left) versus processes in the vacuum beam system (right). A plasma discharge is composed of many species that are simultaneously generated and reaction products from the substrate can be incorporated in the plasma. The VUV and ion sources on the vacuum beam system can be controlled, and reaction products do not affect stability.

The beam system has been implemented in the past to trace possible mechanisms for plasma damage. In addition to the VUV and ion sources used in this study, other sources have been used to provide much insight on plasma/material interactions. Goldman et al. looked at oxygen radical effects and Ar^+ ion pretreatments on porous low-*k* SiOCH films using a radical source and ion source equipped to the beam system.[29] Nest et al. examined roughening of 193 nm photoresist due to simultaneous exposure to VUV photons and high energy ions.[39] The vacuum beam system has become a versatile tool for the study of individual plasma species, especially since it can be configured for specific purposes. One major drawback of this system is the relatively low flux of the emissions compared to plasma exposures. Furthermore, the generation of some types of plasma species is limited, so one has to ensure that these generated species are representative of those found in a typical plasma discharge. For this reason, vacuum beam studies are compared back to plasma exposures.

1.4.2   Inductively-Coupled Plasma Studies

In addition to vacuum beam studies, analysis of plasma discharges is necessary to demonstrate that behavior observed from the various sources is consistent with normal plasma emissions. In order for exposures to be comparable, the internal parameters of the emission, like flux and energy, has to be similar. As a result, one has to take caution to carefully characterize the emissions of plasma species and choose appropriate plasma conditions to implement. The emission of plasma species is greatly affected by not only power input and gas pressure, but also the geometry and size of the chamber, which affects the loss of species to the walls. Because of this, plasma exposures can vary from system to system, despite keeping a majority of the settings the same. However, if the internal parameters are measured, the settings can be tuned such that the bombardment of plasma species is similar.

Internal plasma parameters are typically measured using *in-situ* detectors while the plasma is 'on.' These detectors may include temperature sensors, residual gas analyzers, optical

emission and VUV spectrometers, and Langmuir probes, to name a few. The benefits of these detectors in the plasma system are that the plasma characteristics are known and disturbances in the plasma can be immediately detected. For example, impurities in input gases can drastically change the type of emission but typically demonstrate specific emission behaviors that are easily detected. In this manner, it is possible to achieve plasma emissions that are relatively the same from exposure to exposure regardless of the settings on system controls. However, monitoring of plasma characteristics in this manner is generally limited to line-of-sight measurements, and particular care has to be taken not to disturb the plasma by introducing intrusive probes that could affect loss of species in the surfaces. By accurately examining what species are bombarding the sample material during plasma exposures, better prediction of how the material will be modified can be obtained when the plasma conditions are changed.

1.5   Dissertation Outline

The goal of this study is to examine the fundamental effect of individual plasma species on porous low-*k* dielectric films. By focusing on the role of photons, radicals, and ions generated from the plasma discharge, the reaction mechanisms and parameters that affect how chemical modification occurs will be investigated using two different approaches. Studies in the vacuum beam system attempt to single out the effects of VUV photons and ion bombardment. Studies in the inductively-coupled plasma system will examine the relative contribution of plasma-induced damage caused by either VUV photons or radical species, and further examine the possibility of damage reduction by high energy ions. Chapter 2 describes in detail the experimental setups for the vacuum beam system and the inductively-coupled plasma system. Also, characterization techniques of material properties for the low-*k* films, along with equipment used to characterize plasma discharges under various gas chemistries and conditions will be included. This dissertation then focuses on the role of VUV photons generated from a lamp and covers the mechanism and factors for carbon removal from the low-*k* material in Chapter 3. Chapter 4 relates these findings to VUV radiation found in typical plasmas, revealing that VUV wavelength plays an important role. The main contributors of carbon removal, photons and radicals, are separated from the plasma and individually studied in Chapter 5, with models formulated to predict their effects under a variety of conditions. Lastly, Chapter 6 will investigate the effect of high energy ion bombardment in plasmas and possible methods to prevent subsequent plasma damage.

Chapter 2
System Diagnostics and Characterization Tools

2.1 Abstract

This chapter introduces the reader to the systems used for treatment of porous low-k films in this study. Detailed explanation of the beam sources used in the vacuum beam system and corresponding emission parameters will be provided. Diagnostic tools used to characterize plasma emissions in the inductively-coupled plasma system will be detailed next. Lastly, techniques used to characterize the material properties of the low-k films will be explained.

2.2 The Vacuum Beam System

The vacuum beam system was designed for controlled analysis of plasma species and interactions with materials. This system was originally built by previous graduate student, Yoshie Kimura, and modified by former graduate students Dustin Nest, Mark Goldman, and Ting-Ying Chung. A schematic of the system for this study is shown in figure 2.1. Further details of the vacuum beam system, along with additional functionalities, can be found in the dissertations of the respective students mentioned above.[40-43]

The main chamber, measuring roughly 40 cm x 20 cm x 20 cm, is maintained at a base pressure of ~5.0×10^{-8} Torr by a Seiko Seiki STP H2000C turbo pump, backed by a mechanical roughing pump. Pressure is measured in the chamber using an ion gauge (MDC Vacuum Products). A sample holder is used in conjunction with a magnetically-coupled load-lock transfer arm to allow for sample transfer and processing without breaking vacuum of the main chamber. A small wafer piece, measuring roughly 1.5 cm x 2 cm, can be attached to the sample holder using thermal paste and secured. The sample holder can then be attached to the transfer arm and pumped down with a TV301 Navigator turbo pump (Agilent Technologies), backed by a second roughing pump, before being transferred to the main chamber. The pressure of the transfer arm can also be monitored by an additional ion gauge (MDC Vacuum Products). Once inside the main chamber, the sample holder is placed onto the rotatable dock. A thermocouple (Omega Engineering, Inc.) on the underside of the sample holder monitors the temperature of the sample, while an external water bath is connected to the dock for temperature control. A gas line

on the side of the chamber acts as a gas inlet through a leak valve, with a maximum operating pressure of 10^{-4} Torr.
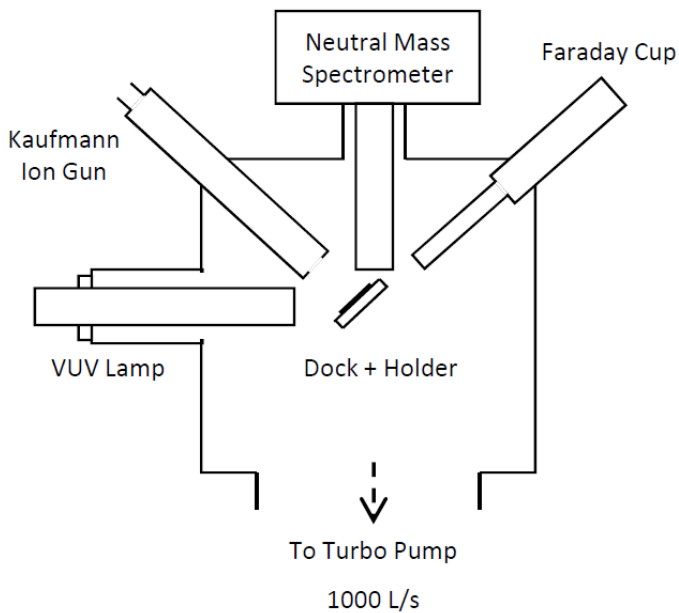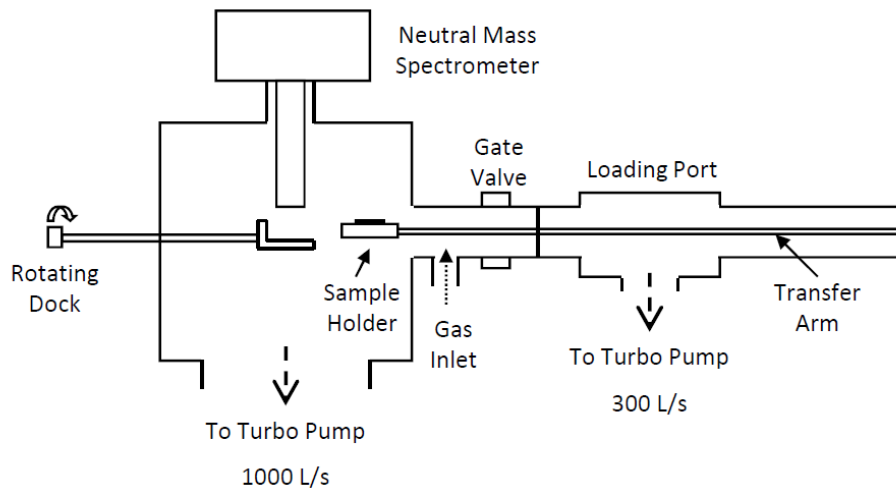
Figure 2.1 Two cross-sectional side views (90° rotation) of the vacuum beam system and equipped beam sources used in this study. Samples are docked in the main chamber using a load-lock transfer arm.

2.2.1 Vacuum Ultraviolet (VUV) Lamp

Emission of high intensity 147 nm radiation is obtained using a closed-volume Xe lamp source (Resonance Ltd.). An internal RF source excites the Xe gas within the closed volume using a frequency of 100 MHz. The other end of the lamp is bound by a MgF_2 window, which allows for 147 nm radiation to escape. Since the gas chemistry, gas pressure, and input power are fixed, the photon emission from the lamp cannot be manipulated. However, the VUV photon flux to samples can be controlled to a small degree by adjusting the working distance. The lamp has been mounted such that the working distance can be adjusted by approximately 1 inch.

Absolute calibration of the VUV photon flux was conducted by a NIST-calibrated CsI diode (Resonance Ltd.). Between operating distances of 6.94 cm and 4.40 cm from the MgF_2 window to the sample, the photon flux ranged between $0.89 - 1.90 \times 10^{14}$ photons/(cm^2·s) respectively. Typically, exposures to samples were performed at a working distance of 4.40 cm but at an incident angle of 45º, giving an effective photon flux of 1.34×10^{14} photons/(cm^2·s). Measurements of photon flux were obtained by a VUV spectrometer (Resonance Ltd.). Further description of the characterization of the Xe VUV lamp can be found in the dissertation of Dustin Nest.[42]

2.2.2 Ion Source

A Kaufman-type ion gun (Commonwealth Scientific Corporation) is used to mimic the effect of ion bombardment from plasma treatments. Ar gas is fed into the discharge chamber of the ion gun. With the absence of a differentially pumped region, the pressure of the main chamber in the vacuum beam system typically increases to ~1×10^{-4} Torr. The cathode of the ion gun is composed of a three-turn tungsten wire, 0.013 cm in diameter, which had to be replaced regularly to ensure stable operation. A discharge between the anode and cathode generates positively-charged ions which are accelerated by the negatively-biased screen grid, thereby exiting the ion gun at a higher energy. The anode potential was set to obtain 150 eV ions for all measurements.

The ion flux can be measured by lowering a Faraday cup (aperture size ~ 4.55×10^{-4} cm^2), mounted opposite of the ion gun, into the direct path of the ion beam. This Faraday cup is connected to a picoammeter (Keithley Instruments), which displays the ion current value. A value of approximately 22 nA translates to an ion flux of 2.7×10^{14} ions/(cm^2·s). One difficulty with the operation of this ion gun was that the current could only be measured when the Faraday cup was in the direct path of the ion beam. This meant that the current could not be measured during exposure to samples, which blocked the beam of ions. For each exposure, the sample was rotated such that the ions would impact normal to the sample surface. Ion current values were measured before and after exposures in order to record the drift in the ion current. Additionally, sample charging of the samples was minimized by a separate neutralizing filament during operation of the ion gun. The neutralizing filament is composed of a tungsten wire, 0.025 cm in diameter, emitting low energy (-5V) electrons at ~6 A of current.

2.2.3 Mass Spectrometry

A Model HAL-301 Positive Ion Counting Residual Gas Analyzer (Hiden Analytical) is also equipped on the vacuum beam system. In this study, the quadrupole mass spectrometer (QMS) was mainly used to examine the background for emission products during the exposures of the low-k films to VUV radiation. The ionizer and quadrupole assembly can be lowered to the sample, and the signal received is directly proportional to the neutral number density in the ionizer.[44] The QMS has a 70 eV electron filament that is used to ionize neutral gas species within the main chamber. These ionized species are accelerated and separated by their mass-to-charge ratio using four voltage-tuned metal rods. However, one has to keep in mind that the ionizing electrons emitted from the filament can also dissociate gas molecules into atomic ions. For this reason, the signals need to be corrected using a technique called threshold ionization mass spectrometry (TIMS), which is detailed further in the dissertations of Mark Goldman and Ting-Ying Chung.[41,43] For the purpose of this study, quantification of emission species was not necessary, so comparison of the background signals before and during VUV exposure was enough to detect key compounds that were removed from the low-k films, ultimately allowing for an understanding of the bond scissioning mechanisms caused by VUV radiation.

2.3 Inductively-Coupled Plasma System

The inductively-coupled plasma (ICP) system used for plasma treatment studies on porous low-k films was originally built by former graduate student Harmeet Singh. This system has been previously used and modified by former graduate students Cheng-Che Hsu and Monica Titus for studies of material modification under various plasma chemistries.[45,46] The system consists of a cylindrical, stainless steel central chamber, 20 cm in diameter and 10 cm in height, with adjacent analysis chambers located on either side. Figure 2.2 shows the cross-sectional side views of the ICP system, rotated by 90 degrees. The plasma chamber is pumped down using various turbomolecular pumps to achieve high vacuum, typically at a base pressure of ~1×10^{-7} Torr as measured by ion gauges (MDC Vacuum Products). The main chamber is equipped with a 1000 L/s Seiko-Seiki turbo pump, backed by a mechanical roughing pump. The side chambers are equipped with smaller turbo pumps, which will be detailed later. The process gas enters near the top of the chamber and pressure is modulated by the inlet flow rate, adjusted with a mass flow controller unit. The main chamber pressure was measured with a MKS Baratron (type 660) capacitance manometer gauge.

Radio frequency (RF) power supplies (ENI Power Systems) are connected to the ICP system in various areas to manipulate the plasma density and ion energy. First, 13.56 MHz RF power is delivered to a five-turn planar coil, which goes through an alumina dielectric window at the top of the chamber. A Faraday shield is placed between the coil and the dielectric plate to minimize capacitive coupling. By controlling the set power and gas pressure, the plasma density can be controlled. While power delivered to the coil maintains the plasma density, it does not have enough energy to initialize the plasma discharge. A "spark of electrons" is needed to ignite the plasma, which is provided by a second 13.56 MHz RF power source delivered to the stainless steel electrode plate at the bottom of the chamber. After the plasma ignites, power to the electrode is immediately turned off. A third RF power supply is connected to the transfer arm to allow for biasing of the sample holder. This biasing accelerates the positively-charged ions from

the plasma towards the sample holder, allowing for higher energy ion bombardment. By adjusting the power delivered, independent control of the ion energy can be achieved.

Numerous sampling ports are located around the ICP chamber, which are equipped with various diagnostic tools to measure the plasma emissions. These diagnostic tools include a vacuum ultraviolet (VUV) spectrometer, an optical emission spectrometer (OES), and a wall-mounted ion current probe. The side analysis chambers are equipped with an ion mass spectrometer and a neutral mass spectrometer.
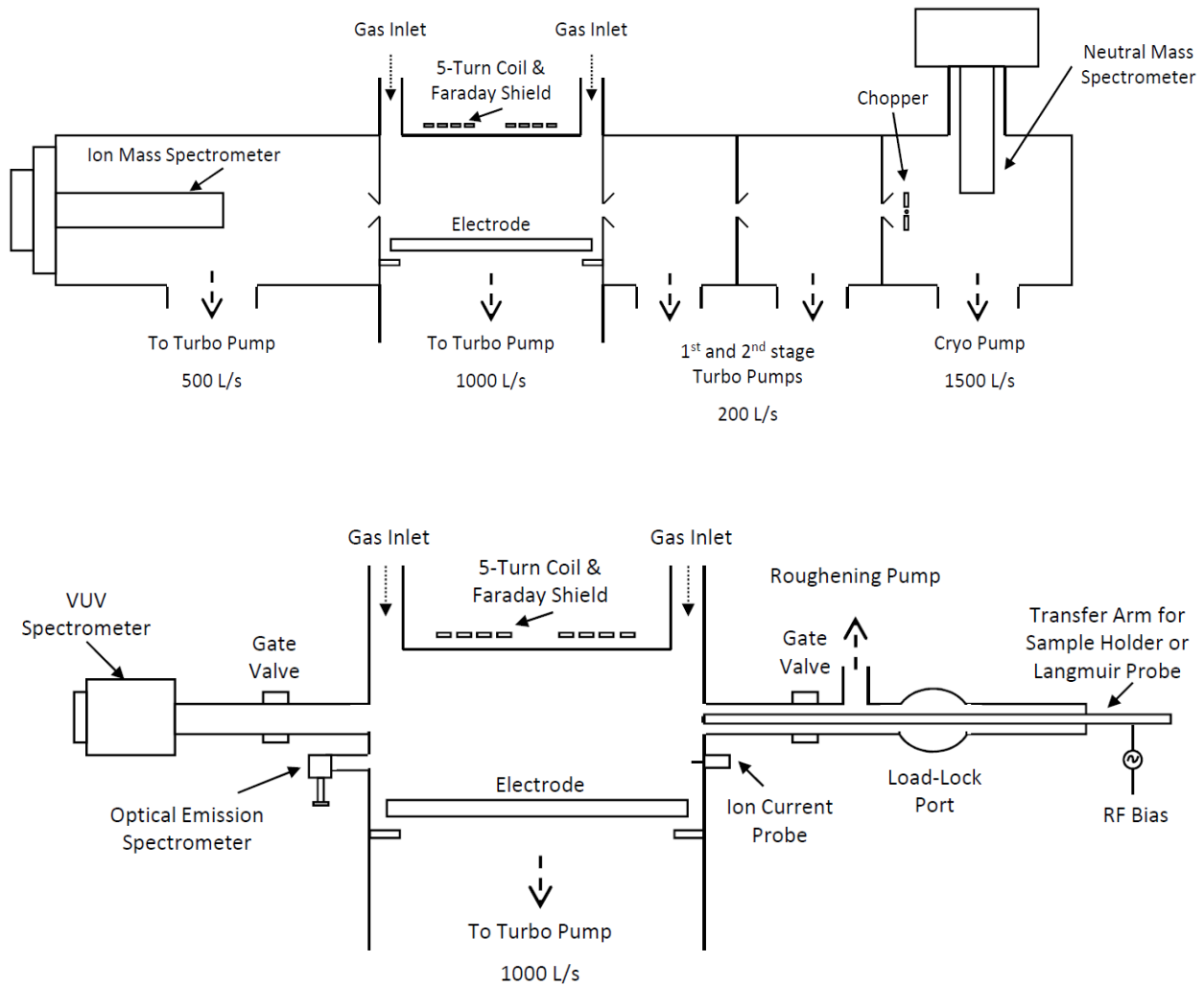
Figure 2.2 Two side views (90º rotation) of the inductively-coupled plasma system and diagnostic tools.

2.3.1   Sample Holder

A sample holder can be mounted on a sampling port to transfer samples ($1 - 2$ cm^2) into the main chamber for plasma treatments. Samples are mounted with kapton tape onto the sample holder via the load-lock port, which is pumped down before the samples are translated into the main chamber. The samples sit flush to the chamber wall and control of temperature and bias can be performed during plasma treatment. Temperature control is achieved using an external Neslab RTE-111 water bath. However, thermal paste (Apiezon H Hi Temp Vacuum Grease) must be applied between samples and the holder to ensure good thermal contact. For bias control, a 13.56 MHz RF power supply is used. Measurements of the ion energy can be performed with a high voltage probe connected to a Tektronix TDS 2022B oscilloscope, which records the bias in the form of a wave function. Estimations of ion energy, E, can be calculated by the following equation:

$$E = \frac{A}{\sqrt{3}} + \Phi_p \qquad\qquad (2.1)$$

where A is the difference between the minimum and maximum values for the wave function measured by the oscilloscope and Φ_p is the plasma potential, measured by a Langmuir probe.

An additional attachment is also available to allow for filtration of certain plasma species as shown in figure 2.3. A copper plate with groves covers the original sample holder, which allows for the docking of a second copper plate, fitted to slide into place. A Teflon cap can then be screwed onto the second copper metal plate to house a sample within an isolated region. Filters can be used to block out certain plasma species, allowing for single component exposure. For example, a MgF$_2$ window can be placed to allow transmission of only photons to the sample. Modifications of the Teflon cap can be implemented to block out other plasma species, such as radicals. Further details of this attachment will be covered in Appendix A.
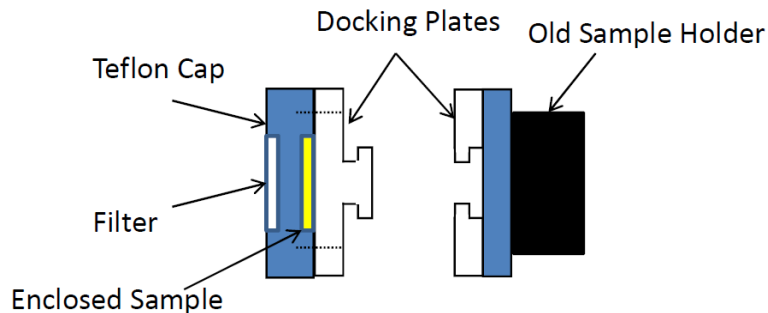
Figure 2.3 Additional attachment to the sample holder. The Teflon cap allows for placement of a filter to block out certain plasma species. The sliding plates allow for easy docking of the enclosed sample. Different configurations of the Teflon cap can be used for specific purposes.

2.3.2   Langmuir Probe

The Langmuir probe can be introduced into the plasma chamber to measure the electron density (T_e), electron temperature (n_e), and plasma potential (Φ_p). This probe is inserted in place of the sample holder and can be translated to access different radial positions, ranging from the center to the edge of the plasma discharge (r = 0 cm to 7.5 cm). The Langmuir probe was designed by previous student Harmeet Singh according to the guidelines given by Godyak *et al.*, which allows for measurement of parameters without significant disruption of the plasma.[47,48] Measurement of plasma parameters is performed by doing a voltage sweep, V_p, on a platinum wire (125 μm in diameter, ~5 mm in length) located at the end of the probe, which collects the electrons as a current reading, I_p. Calculation of the electron energy probability function (EEPF) and electron energy density function (EEDF) can be performed using the second derivative method.[47,48]
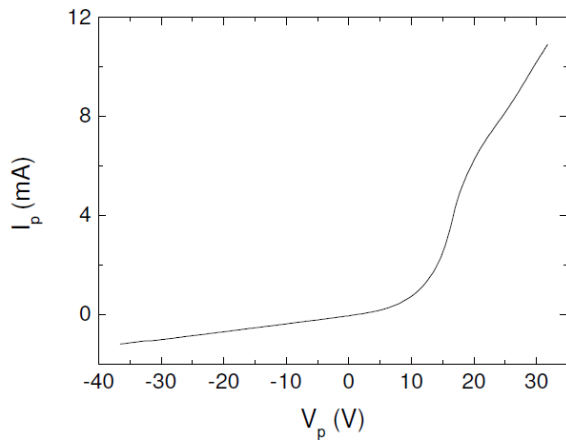
Figure 2.4 Langmuir probe voltage sweep.
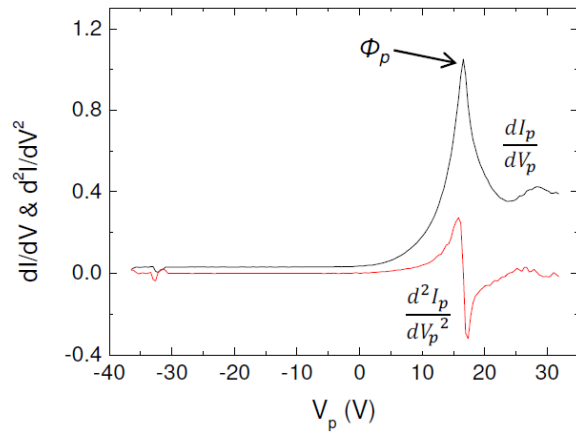
Figure 2.5 The first and second derivative of the Langmuir probe voltage sweep.
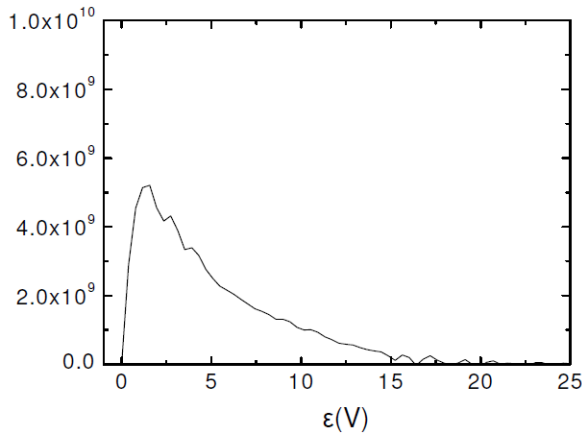
Figure 2.6 The electron energy distribution function (EEDF) vs. electron energy. Integration of the curve yields electron density, n_e.
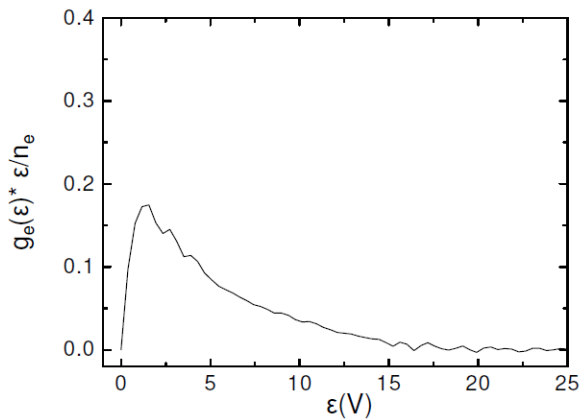
Figure 2.7 Integration of curve yields the average electron energy, $<\varepsilon>$.

15

Using the I_p-V_p curve from figure 2.4, the first and second derivatives can be obtained (Figure 2.5). The maximum of the first derivative yields the plasma potential, while the second derivative is used to obtain the EEPF and EEDF in the equations below.

$$g_p(\varepsilon) = \frac{2m}{e^2 A} \left(\frac{2e}{m}\right)^{\frac{1}{2}} \frac{d^2 I_p}{dU_p{}^2} \tag{2.2}$$

$$g_e(\varepsilon) = \frac{2m}{e^2 A} \left(\frac{2e}{m}\right)^{\frac{1}{2}} \frac{d^2 I_p}{dU_p{}^2} \sqrt{\varepsilon} = g_p(\varepsilon)\sqrt{\varepsilon} \tag{2.3}$$

where ε is the electron energy (eV), m is the mass of an electron (kg), e is the charge of an electron (C), A is the surface area of the probe, and U_p is the probe potential with respect to the plasma potential ($U_p = \Phi_p - V_p$). Integration of the EEDF (Figure 2.6) yields the electron density, n_e, and the electron temperature is defined as 2/3 of the average electron energy, <ε>, which can be calculated by integration of the curve in figure 2.7.

$$n_e = \int_0^\infty g_e(\varepsilon) d\varepsilon \tag{2.4}$$

$$< \varepsilon > = \frac{1}{n_e} \int_0^\infty \varepsilon g_e(\varepsilon) d\varepsilon \tag{2.5}$$

2.3.3   Ion Current Probe

Positive ion current is collected using a 0.4 cm^2 wall-mounted, planar ion current probe that is DC-biased to -40 V. During a plasma discharge, the ion current is measured with an Agilent 34410A 6½-digit multimeter. Readings from the multimeter can be transferred using the IntuiLink toolbar in Excel to monitor plasma stability. Using calibrated parameters for the ion current probe, the current received can be converted into an absolute value for the ion flux.

Figure 2.8 shows the ion current for Ar plasma at plasma conditions of 10 mT and 70 W from start to finish. To ignite the plasma, it is necessary to bias the bottom electrode. As a result, there is a sudden spike in the ion current. After the plasma ignites, the bottom electrode is turned off, and the ion current remains fairly steady over the duration of the discharge. The ion current immediately drops when power to the coils is turned off, extinguishing the plasma.
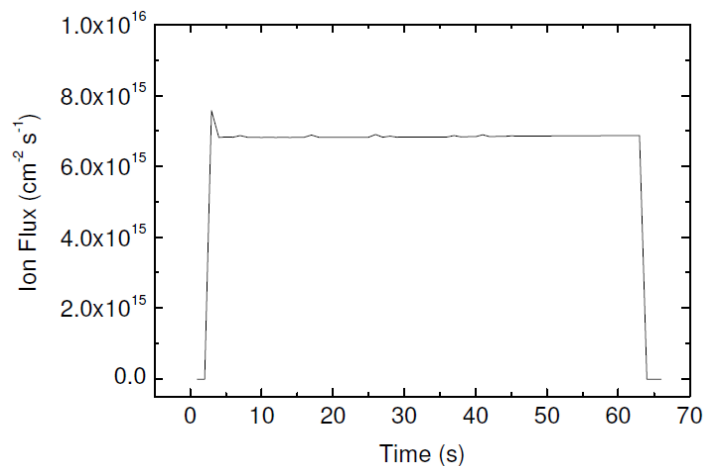
Figure 2.8 Ion flux as measured by the ion current probe for Ar plasma at 10 mT and 70 W. An initial spike in the current occurs when the plasma is ignited by the bottom electrode. Current remains relatively stable after bottom electrode is turned off and plasma is maintained by power through the coils.

2.3.4   Vacuum Ultraviolet Spectrometer

Plasma generated VUV emissions are monitored with a Resonance LTD VSFS92 VUV spectrometer mounted on a side-wall port, opposite of the sample holder. The spectrometer is comprised of a concave holographic grating (1,800 grooves/mm) and a linear CCD detector (0.2 × 28 mm). To minimize ion damage, the VUV spectrometer rests a distance away from the main chamber through a connecting branch. A gate valve is located on the connecting branch, which can be closed to isolate the VUV spectrometer from the main chamber. The region around the detector is pumped down directly by the turbomolecular pump in the main chamber.

A dial located on the spectrometer hardware can be adjusted to change the grating, thereby providing a different wavelength collection window (25 nm to 450 nm). For these studies, the dial was set to 150, which corresponds to a wavelength range of 100-200 nm. Measurements of the signal intensity and data collection were performed via Labview software. The integration time was adjusted to prevent flooding of the detector signal and was typically at a value of 4000 ms. Figure 2.9 shows the intensity of various emissions originating from Ar, O_2, and NH_3 plasma. Calibration of the signal intensities to absolute VUV fluxes, along with solid angle correction for the detector position, is documented elsewhere.[41,46]
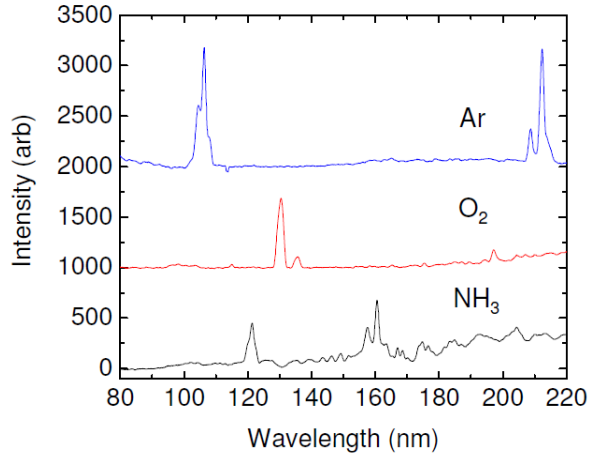
Figure 2.9 VUV emissions as detected by the VUV spectrometer for Ar, O_2, and NH_3 plasmas.

2.3.5 Optical Emission Spectrometer

An Ocean Optics PC2000-UV-VIS-ISA optical emission spectrometer (OES) is equipped to the plasma system to detect emissions from the plasma in the range of 200-850 nm. Emission from the plasma exits the viewing port at the side of the chamber and is focused with a collimating lens, where it travels through an optical wire to the spectrometer (connected by an ISA port to the PC). A 2048 element, linear CCD array collects the electromagnetic spectrum with a 1.5 nm FWHM resolution. While the OES can capture the full spectrum in 1 ms, the integration time needs to be adjusted to achieve high signal-to-noise ratio.
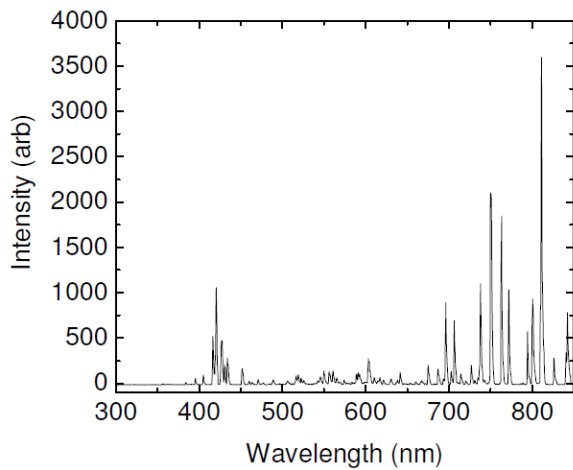
Figure 2.10 The optical emission spectrum of Ar plasma. Characteristic peaks at 420.0 nm and 811.5 nm are examined for stability.
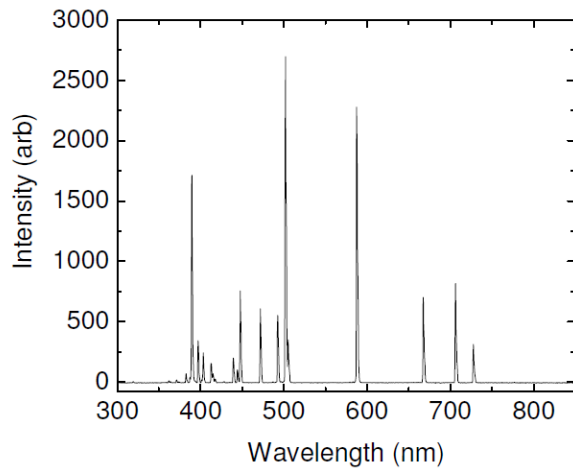
Figure 2.11 The optical emission spectrum of He plasma. Characteristic peaks at 501.6 nm and 587.6 nm are examined for stability.

18

In these studies, the OES was used mainly to monitor the stability of the plasma, as could be observed by the temporal evolution of the emission peaks.[45] In addition, the spectra can be analyzed for changes in plasma chemistry, such as impurities or reaction products in the plasma. Since spectra are captured fairly quickly, shifts in the plasma chemistry can also be detected easily when transitioning from one chemistry to the next. For example, ignition of He plasma in the ICP system is difficult and requires transitioning from another plasma, such as Ar plasma. After Ar plasma is ignited, He gas is slowly fed in, while the Ar gas is slowly turned off. As shown in figures 2.10 and 2.11, the optical emission spectra will change from Ar to He. When the plasma discharge has fully converted to He plasma, the characteristic peaks for Ar will no longer be observed. The optical emission spectrum provides a good method to indicate the components within the plasma discharge through various emission peaks unique to each plasma chemistry.

2.3.6 Mass Spectrometry

On the side chambers, mass spectrometers are equipped to monitor the ion and neutral concentrations of plasma species. As shown in figure 2.2, a UTI-300C quadrupole mass spectrometer (QMS) is equipped within a region where it is differentially pumped by a 500 L/s turbomolecular pump (Pfeiffer Balzers TPU-510 with TCP-380 controller). The base pressure is maintained in the range of $10^{-8} – 10^{-7}$ Torr. At the other end, a Hiden Analytical PIC300 QMS is mounted. Three separate differentially-pumped regions separate the QMS from the main chamber. The first two regions are pumped down by 200 L/s turbomolecular pumps (Pfeiffer TPU-170 with TCP-310 controllers), while the 3rd stage is pumped down by a 1500 L/s cryogenic pump (On-Board 8F, CTI-Cryogenics, Helix Technology Corp.). Descriptions of these mass spectrometers are further detailed in the dissertations of Singh[44] and Hsu[45].

While the ion and neutral mass spectrometers were not used in this study, it is notable that they are useful when studying more complex plasmas, such as plasmas with gas mixtures or contaminants. Specifically, the concentrations of specific plasma species can be determined, which is beneficial when the gaseous species have different ionization potentials. Furthermore, mass spectrometry in this system only works when the plasma is under a collision-less regime, limiting the detection of the species by the QMS to low operating pressures (< 40 mTorr).

2.4 Porous Low-*k* Dielectric Films

The porous low-*k* material used for the following results is an organosilicate glass called SiOCH which is composed mainly of a silicon dioxide network with terminating methyl (-CH_3) groups. Films of this material are typically generated by plasma-enhanced chemical vapor deposition (PECVD). Depending on the gas recipe, the type of sacrificial porogen used, and the type of UV cure, the resulting properties of the film can be manipulated.[5,49] The formation of ethyl (Si-CH_2-Si) links within the material and the average pore diameter are heavily affected by such specifications. As a result, the mechanical and dielectric properties of the film can be manipulated in various ways.[50-52] Furthermore, resistance to chemical change can also result from differences in the film properties.

The two types of porous-SiOCH material used in this study were supplied by Novellus, Inc. (now Lam Research). These two materials are called p-ULK and d-ULK. While the two materials are similar in chemical structure and have similar dielectric constants, the key difference is the type of porosity within the films. P-ULK uses a sacrificial porogen to create open porosity, leading to high pore interconnectivity and high diffusivity. D-ULK instead contains a higher amount of nanoporosity, resulted from the removal of methyl bonds during the UV cure process to create high amounts of closed porosity. As a result, d-ULK has a much lower diffusivity. The properties of the two materials are shown below in Table 2.1. For this study, p-ULK went through much faster rates of chemical modification by plasma species. As a result, p-ULK was studied more extensively to quantify the extent of modification. In addition, the influence of various plasma treatments and their effect on respective damage mechanisms would be more clear. The sections below will detail techniques used to characterize the porous-SiOCH films and investigate the effects of plasma treatment.

Table 2.1. Properties of p-ULK and d-ULK SiOCH films.

Material	k Value	Diffusivity ($\mu m^2 \cdot min^{-1}$)	Film Thickness (nm)
p-ULK	2.4 - 2.54	1500	220-300
d-ULK	2.55	250	500

2.4.1 Fourier-Transform Infrared Spectroscopy

Bulk characterization of chemical bonds in the porous-SiOCH films were performed with *ex-situ* FTIR spectroscopy (Excalibur FTS-3000, Agilent Technologies). The stretching and bending vibrations for characteristic bonds can be found in the mid-infrared radiation (600-4000 cm^{-1}) region, which makes it easy to track chemical changes to this material. Furthermore, the characteristic peaks for carbon-doped silicon dioxide materials are well-established in literature.[3,5,53-55] Infrared radiation is emitted from a ceramic source that travels to the interferometer, through the sample compartment, and then is picked up by a cryogenic mercury cadmium telluride (MCT) detector. The interferometer allows for the simultaneous measurement of all wavelengths present. A Fourier transform is needed to convert this received signal to a frequency spectrum, allowing for analysis of chemical bonds present. Sample acquisition and analysis were performed with Resolutions Pro (Agilent Technologies) software.
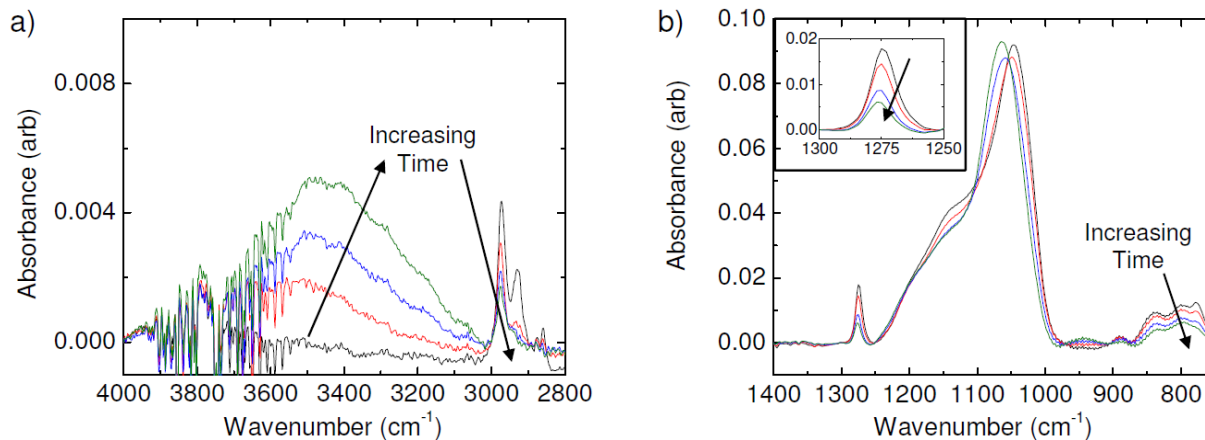
Figure 2.12 The characteristic peaks observed in the FTIR spectrum for a sample of the porous low-*k* film (p-ULK). With increasing treatment time to plasma, the peak intensities change as indicated by the arrows.

Figure 2.12 shows the resulting peaks that are observed for a sample of the porous low-*k* film. The measurement shows an arbitrary intensity of vibrational modes detected within the sampling area (~1 cm in diameter circle) of the film. Since the porous low-k films were deposited on a Si substrate, the signal from Si wafer-only spectra must be subtracted to obtain the film-only spectra. All spectra were also truncated and baseline corrected to examine the absorption bands between 500 cm^{-1} and 4000 cm^{-1}. The main peaks of interest are the Si-O-Si network and cage structure (1200-1000 cm^{-1}), Si-C bending (1280 cm^{-1}), and SiOH/H$_2$O broad region (3800-3000 cm^{-1}). Other peaks that signify the CH$_3$/CH$_2$ stretching modes (3000-2900 cm^{-1}) and the Si-CH$_3$ bending and rocking modes (860-750 cm^{-1}) tend to be less noted due to the multiple, convoluted peaks. The loss of methylated species within the silicon dioxide network and the uptake of water have been noted to be the major reasons for increases in the dielectric constant, so the change of Si-C/Si-O and the increase of SiOH/H$_2$O are major indicators of damage to porous low-*k* films.[3,5-6] After plasma treatments of various times, the chemical peaks are observed to shift, indicating losses or gains of certain bonds. By comparing these changes in a FTIR spectrum before and after plasma treatment, the amount of carbon loss and the relative amount of water uptake can be quantified. As a result, many of the future discussions will involve looking at fractional carbon content and net water gain as compared to the pristine film.

FTIR spectroscopy can also be combined with HF stripping in order to examine regions of the low-*k* films that are damaged by plasma treatment. Dilute solutions of HF (~1%) in water are observed to remove carbon-depleted oxide, but not the pristine low-*k* material.[56] The remaining film after the HF strip retains properties of the original, untreated film. As a result, the thickness of the damaged layer can be estimated by comparing the ratio of the FTIR peaks after the HF strip to the original sample. This technique allows for a simple estimation of damage penetration caused by the plasma species.

2.4.2 Mercury Probe

Simple characterization of the dielectric properties of the low-*k* films were performed by a Model 802-150 three-function mercury probe (Materials Development Corp.). The measurements were carried out with the aid of Feng Pan and Steve Volkman from Prof. Subramanian's group. Measurements consisted of depositing a drop of mercury onto the surface of the low-*k* film that forms a metal-oxide-semiconductor (MOS) structure in which the capacitance-voltage characteristics can be examined. This method removes the need to sputter aluminum contacts onto the surface of the film. By connecting the mercury probe to a Model 4285A Precision LCR Meter (Hewlett Packard), the capacitance of the film can be measured. With known values for the film thickness and the mercury contact size, the dielectric constant can thus be calculated. Values for the dielectric constant obtained through this method were in agreement with values obtained from Novellus, the supplier of the low-*k* films.

Chapter 3

VUV Photon/O$_2$ Gas Effects on Porous Low-*k* Dielectric Films

3.1   Abstract

Damage incurred during plasma processing, leading to increases in dielectric constant, *k,* is a persistent problem with porous low-*k* dielectric films, such as SiOCH. Although most of the proposed mechanisms of plasma-induced damage focus on the role of ion bombardment and radical attack, plasma-generated vacuum ultraviolet (VUV) photons can be shown to play a role in creating damage leading to increases in the dielectric constant of this material. Using a vacuum beam apparatus with a calibrated VUV lamp, 147 nm VUV photons impacting SiOCH results in post-exposure adsorption and reaction with water vapor from the atmosphere to form silanol bonds, thereby raising the dielectric constant. The vacuum beam photon fluences are representative of typical plasma processes, as measured in a separate plasma tool. Furthermore, the level of damage increases synergistically under simultaneous exposure to VUV photons and O$_2$, which can be explained from the study of residual gas emissions during the exposure. Fourier-transform infrared (FTIR) spectroscopy (*ex-situ*) and mass spectrometry (*in-situ*) indicate that O$_2$ reacts with methyl radicals formed from scissioned Si-C bonds to create CO$_2$ and H$_2$O, the latter combining with Si dangling bonds to generate more SiOH groups than with photon exposure alone. In addition, sample near-surface diffusivity, manipulated through ion bombardment and sample heating, can be seen to affect this process. These results demonstrate that VUV photo-generated surface reactions can be potent contributors to low-*k* dielectric SiOCH film plasma-induced damage, and suggest that they could play analogous roles in other plasma-surface interactions.

3.2   Introduction

Low-*k* organosilicate (SiOCH) porous dielectrics have received much attention as a replacement for SiO$_2$ for Cu interconnects. However, the electrical and mechanical properties of these materials can degrade when exposed to plasmas. Plasmas are used for etching, stripping, adhesion promotion and cleaning, and this represents a potentially serious problem as silicon

technology shrinks to the 22nm node and below.[11,12,16] Understanding the source of this damage is of great importance to the successful integration of this material into future processing. During plasma etching processes, the dielectric film is subjected to a combination of vacuum ultraviolet (VUV) photons, ions, electrons and radicals. Most previous studies have attempted to identify the source of damage of this problem by measurements made under typical plasma conditions. Furthermore, these studies mainly focus on the role of ion bombardment and radical attack in film damage.[29,33] By contrast, Jinnai *et al.* inferred the importance of VUV photons on the low-*k* dielectric constant in a neutral beam system.[57] VUV photons have been shown to break down small amounts of organic impurities in SiO_2 films during photochemical treatments.[35] SiOCH films that are doped with methyl bonds can similarly be photolyzed, resulting in the creation of an electron-hole pair that becomes a Si dangling bond which can interact with H_2O to form silanol.[36] Similar mechanisms have been reported to occur in gate oxide films with photon energies greater than 8.8 eV.[9,37,38] Furthermore, the choice of gas chemistry in a plasma has been shown to result in different levels of silanol formation and therefore change in *k*.[26,27] This suggests that plasma neutral chemistry may couple with VUV effects to alter dielectric property changes.

In the present chapter, using Fourier Transform infrared (FTIR) spectroscopy pre- and post-exposure, 147 nm VUV photons are shown to scission Si-C bonds in SiOCH, leading to the formation of SiOH groups. The addition of a flux of molecular O_2 to this VUV radiation significantly increases this effect, strongly implying that potentially important plasma-generated damage mechanism are due to VUV photon-neutral synergism and sample/gas diffusivity.

3.3 Experimental Setup

Samples (~1 cm^2) of p-ULK (*k* = 2.54) consisted of a ~300 nm thick SiOCH film deposited onto a Si(100) substrates by plasma-enhanced chemical vapor deposition (PECVD), which were obtained from Novellus, Inc. The samples were placed onto a stage inside a stainless steel vacuum vessel (figure 3.1) equipped with a 2000 L s^{-1} turbo pump, which maintains a background pressure of 8×10^{-8} Torr. At this condition, water vapor is the main contribution to the pressure. The stage can be rotated such that a sample is oriented at an angle facing either towards or away from the VUV source. Exposures with 147 nm VUV radiation were performed using a Xe excimer lamp from Resonance Ltd. at 45 degrees from sample normal. The photon flux at the sample for all experiments was calibrated to be 1.3×10^{14} photons/(cm^2 s) (+/- 10%).[39] Before exposures to VUV radiation, oxygen can be introduced to a background pressure of up to 1×10^{-4} Torr. Exposure to VUV radiation led to negligible sample heating, so all experiments were performed at room temperature (~22 C^o), unless otherwise noted. The wavelength of VUV radiation from the Xe source (λ = 147 nm) is noted to be similar to that seen in typical oxygen plasmas (λ = 130 nm). Woodworth *et al.* reports that 147 nm photons penetrate amorphous SiO_2 to a depth of ~5000 nm. Since SiOCH is composed of mostly SiO_2, relatively little photon absorption is anticipated in the thin film samples.[9] Yet, these photons are reported to have enough energy to break Si-C bonds.[57] Furthermore, other studies have shown comparable effects between the Xe source and plasma exposures at similar VUV fluences.[10]
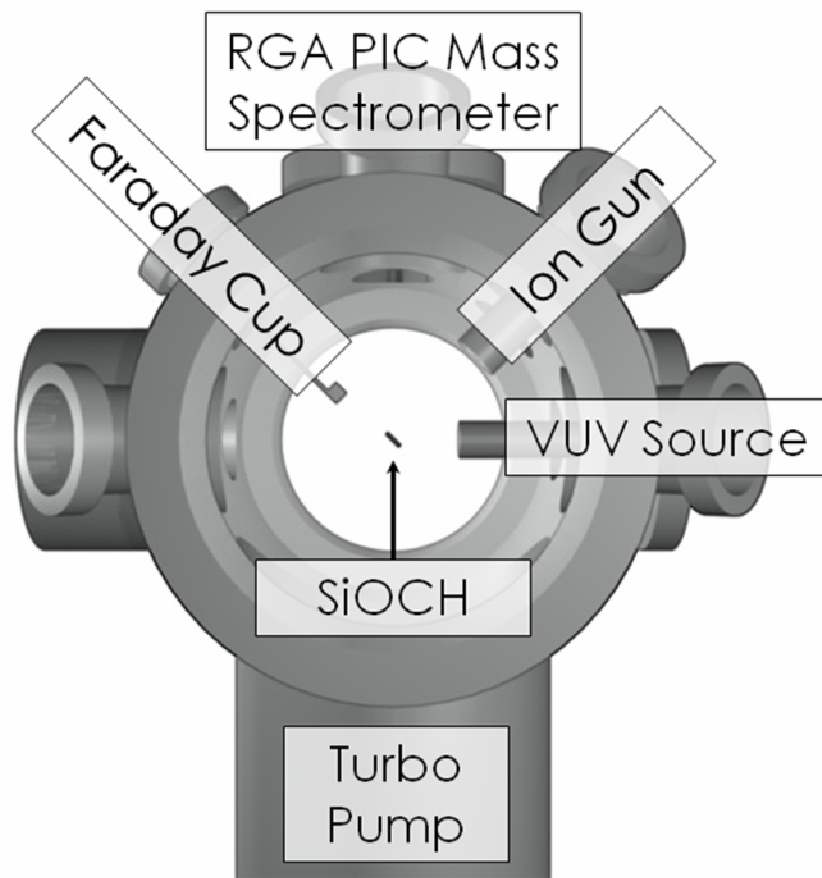
Figure 3.1 Experimental setup of process chamber. All samples have been rotated such that the angle of incidence of ions is normal (0°) and photons is 45°. Not shown: water bath/thermocouple connection for direct sample heating and temperature output.

Exposure of samples to ions came from a Kaufman ion gun (Commonwealth Scientific) in which generated Ar ions are accelerated to 150 eV before striking the sample at normal incidence. The current is measured using a faraday cup that is translated into the path of the ions, measuring a typical ion flux of 2.7 x 10^{14} ions/(cm^2 s). A neutralizing filament was present in the chamber to emit low energy electrons for neutralizing positive charge buildup on the sample surface.

After exposure, *ex-situ* FTIR spectra were obtained for the p-ULK samples to measure bulk modifications in chemical bond structure in the region of 4000-500 cm^{-1}. Characterization of the chamber background gas was performed using a Hiden Analytical Model HAL-301 Positive Ion Counting Residual Gas Analyzer (PIC-RGA) operated at an electron energy of 70 eV.

3.4   Results and Discussion

Figure 3.2 shows the FTIR spectra of the p-ULK samples following various exposures.[5] VUV exposures were for a period of 1 hr, and O_2 background pressure, when applied, was at 10^{-4} Torr. Exposure to O_2 alone does not further oxidize the film, while exposure to VUV radiation in vacuum was enough to break a portion of sp^3 CH_3 bonds at 2980 cm^{-1} and generate a small amount of SiOH, shown by the broad peak at 3500 cm^{-1}. The presence of oxygen during VUV radiation generated greater loss in the sp^3 CH_3 peak and much larger growth in the SiOH peak, suggesting that O_2 interacts synergisticly with VUV photons in creating SiOH.
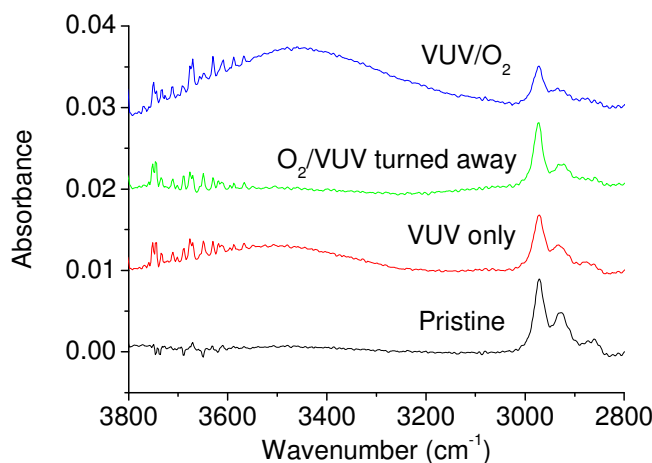
Figure 3.2 Comparison of FTIR spectra for various exposures. The sample can be oriented either towards or facing away from VUV exposure.
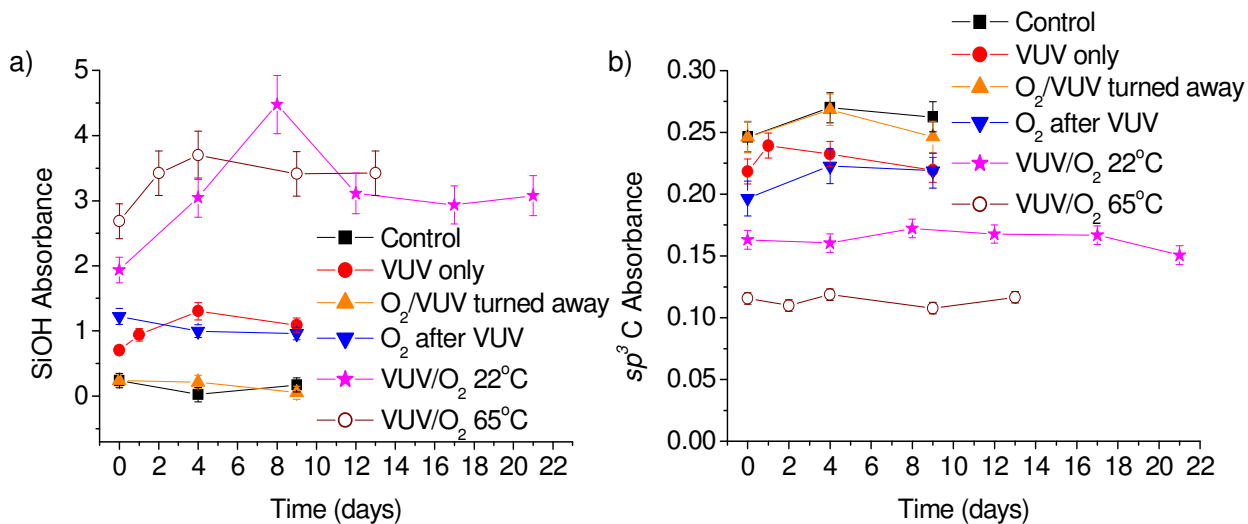
Figure 3.3 a) SiOH and b) sp^3 carbon integrated FTIR peak values as a function of time (days) of the pristine p-ULK film subjected to various exposures.

The possibility that photons were photolyzing O_2 to create O was explored by facing the sample away from the VUV radiation.[58] With this sample orientation (cf. figure 3.2), negligible sp^3 carbon loss is seen and no SiOH is generated, leading to a conclusion that photo-generated oxygen radicals did not have a significant effect on the experiments. This observation is further supported by O_2 photodissociation estimates based on known cross sections[59] and by a comparison of the mass spectra at 16 amu (O^+) obtained by the PIC-RGA that show negligible generation of oxygen radicals.

From figure 3.3a, the generation of SiOH bonds in the film for several days after exposure is evident for simultaneous VUV/O_2 irradiated samples. After each exposure, the samples were removed from the vacuum chamber and stored at atmospheric conditions (22°C, ~50% humidity). FTIR spectra were gathered until saturation of the SiOH integrated peak was observed. The simultaneous exposure of VUV radiation and oxygen can be noted to increase the duration required to fully saturate the sample. The SiOH peak appears to decline slightly before reaching a stable value. During this period of saturation, no significant change occurs in the sp^3 CH_3 peak. This suggests that Si dangling bonds generated from VUV exposure are rather long-lived.[11,12,16] Sample heating during exposure (65°C) is also seen to have effects on damage generation, especially in loss of sp^3 carbon. Furthermore, sequential exposure of O_2 after VUV exposure does not increase damage significantly, but instead remains similar to a VUV only exposed sample. Simultaneous exposure of VUV photons and oxygen is therefore necessary to observe the enhanced level of damage. Furthermore, such exposures increase the material hydrophillicity, allowing for water vapor to enter the film easily.
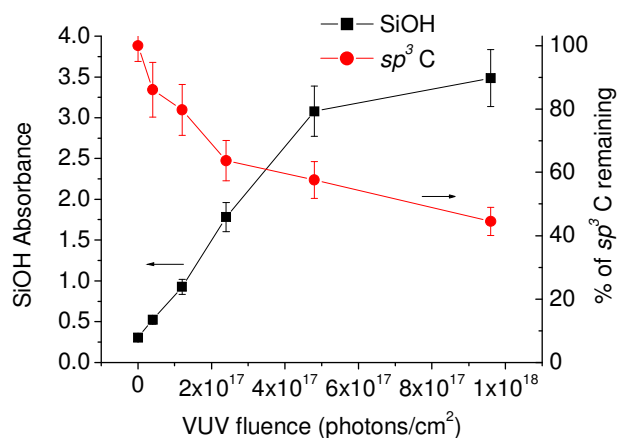
Figure 3.4 SiOH and sp^3 carbon integrated peak absorbances for varying VUV fluences.
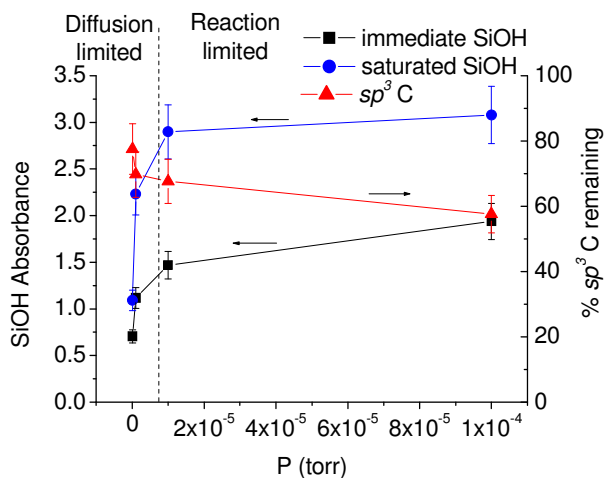
Figure 3.5 SiOH integrated peak absorbances for constant VUV fluence and varying oxygen background pressures for the p-ULK film immediately after exposure and after fully saturating for several days. Corresponding sp^3 carbon peaks are shown for each case.

Background pressure of oxygen and VUV fluence also determined the rate and extent of carbon loss and silanol generation. Figure 3.4 displays the FTIR integrated peak values of SiOH and sp^3 carbon upon VUV exposure of different fluences at a constant pressure of 10^{-4} Torr. SiOH generation can be seen to occur even at low fluences with the xenon photon source. Typical plasma exposures can reach these photon fluence levels in a short span of time (< 1 min).[10] The amount of carbon loss and silanol generation indicates that 147 nm photons can penetrate fairly deep into the film, thereby depleting a large amount of carbon. At later points, further carbon loss may be controlled by oxygen diffusion into the deeper portion of the bulk.

Figure 3.5 shows p-ULK samples that were exposed for a period of 1 hr of VUV radiation, corresponding to a VUV fluence of 4.8×10^{17} photons/(cm^2 s), at various background pressures of O_2. FTIR spectra of the SiOH integrated peak values were recorded as a function of O_2 pressure. At low pressures, the changes for sp^3 carbon and SiOH increases dramatically with O_2 pressure increase. At higher O_2 pressures, the level of damage appears to be less sensitive to O_2, suggesting that the reaction sites are all saturated with O_2. Both diffusion- and reaction-limited regions for damage change can be seen. While the presence of molecular oxygen appears to play a large role in photon-induced chemical change, the mechanism for this behavior has not been previously investigated. Observations from residual gas emissions for VUV exposed samples in the vacuum beam system at a pressure of 10^{-7} Torr (figure 3.6) only show increases at mass-to-charge ratios of about 15 amu, with lower values at 12, 13, and 14 amu that denote the ionizer cracking pattern. These increases are likely from scissioning of the Si-CH$_3$ bond, creating methyl (CH$_3$) radicals. With the addition of molecular O_2, these signals disappear. It is likely that these methyl radicals are consumed to form other products, such as H_2O and CO_2.[60] The direct and unambiguous detection of these latter products by mass spectrometry is difficult due to the relatively small amount that originates from the samples compared to the chamber background. However, these reaction products create an irreversible reaction path for carbon removal.
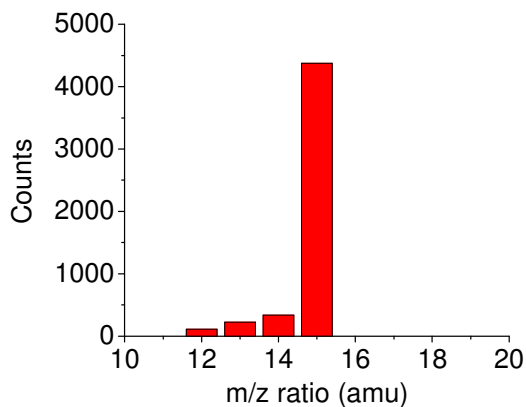
Figure 3.6 Gas emissions captured by the mass spectrometer from the p-ULK sample during exposure to VUV radiation in the vacuum beam system. Without the presence of O_2, Si-C content in the films is lost through photo-dissociation of the Si-C bond, forming methyl radicals.

Ion bombardment was used to manipulate the diffusivity to observe effects in SiOH generation and sp^3 carbon loss. As shown by Goldman *et al.*, ion bombardment appears to cause surface densification, limiting diffusion into the porous film. This results in limitation of silanol generation to the surface region instead of penetration throughout the bulk.[29] Figures 3.7a and 3.7b shows the post-exposure SiOH and sp^3 carbon integrated peaks following ion bombardment alone and ion bombardment coupled with subsequent VUV/O_2 exposures. Ion bombarded samples were treated with 150 eV Ar ions for 1 hr, resulting in a fluence of 9.9 x 10^{17} ions cm^{-2}. During ion exposure, the sample temperature increased ~5°C. While the Ar ion exposure itself decreases the sp^3 carbon content, SiOH formation is small. Exposure to VUV/O_2 after ion bombardment results in less damage compared with VUV/O_2 in the absence of ion bombardment. These observations appear consistent with the interpretation that ion bombardment reduces near-surface diffusivity.
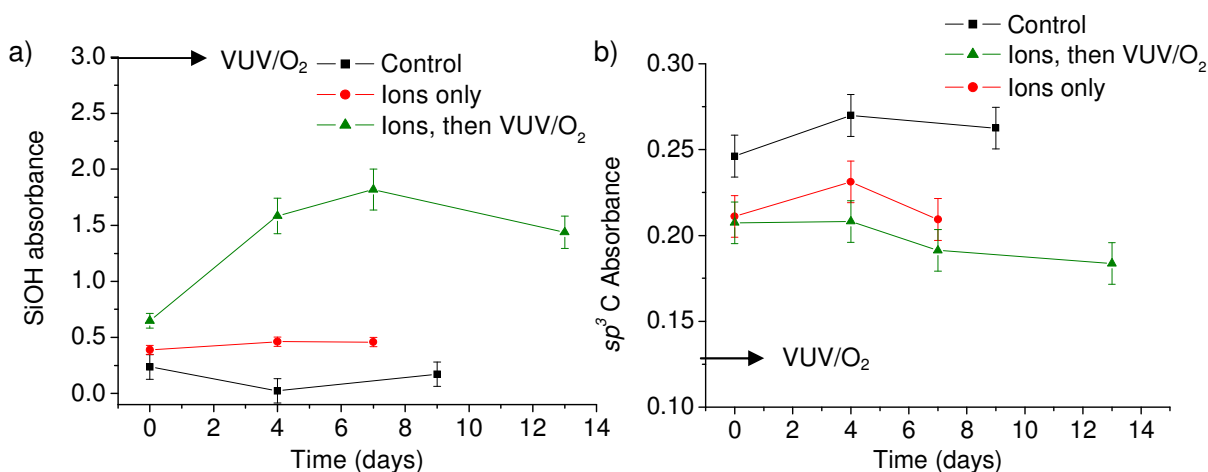
Figure 3.7 a) SiOH and b) sp^3 carbon integrated peak values post-exposure for ion bombardment experiments. Comparison with VUV/O_2 only experiment is shown.

Based on these observations, the enhanced level of damage from simultaneous VUV/O_2 exposure is proposed to be caused by to the reaction of O_2 with a methyl intermediate desorbing due to broken Si-C bonds (figure 3.8). The methyl intermediate reacts to generate CO_2 and H_2O within the pores. The H_2O liberated goes on to combine with the Si dangling bond, forming SiOH during exposure.[35] A lack of oxygen in the pores allows methyl to recombine with VUV-generated Si dangling bonds, because methyl radicals are less volatile than CO_2 and H_2O. Upon recombination, the reactive sites are once again occupied, preventing the formation of silanol. However, SiOH bonds created during the exposure are also subjected to VUV radiation effects due to significant absorption coefficients for higher energy (>8 eV) photons, recreating Si dangling bonds.[61,62] Post-exposure generation of silanol is then apparently due to atmospheric H_2O reacting with remaining Si dangling bonds. An ion pre-treated sample forms a diffusive barrier that blocks O_2 transport into the porous film, allowing for more Si-CH$_3$ re-formation. Based on this proposed mechanism, diffusion of O_2 and H_2O into the p-ULK film is very important in determining the extent of damage caused by VUV/O_2 exposure, and subsequently O_2 plasma. However, the use of an oxygen plasma produces photons of a lower wavelength (λ =

130 nm). It would be expected that the extent of damage may saturate sooner compared to the xenon source because the penetration depth is predicted to be significantly lower (~200 nm).[9] This will be explored in the next section.
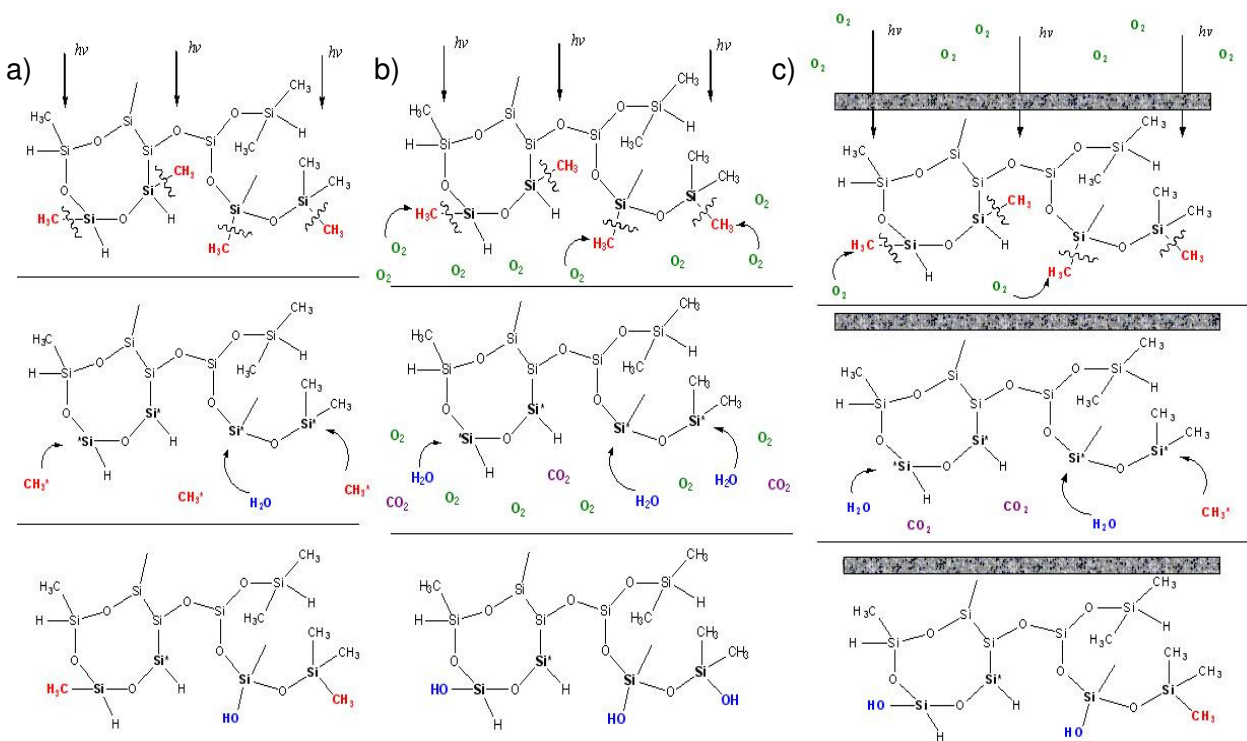
Figure 3.8 Proposed mechanisms for a) VUV radiation only, b) VUV/O_2 exposure, and c) ion pre-treatment before VUV/O_2 exposure. VUV radiation scissions Si-CH$_3$ bonds, creating Si dangling bonds. Broken methyl compounds will react with any available O_2, creating CO_2 and H_2O. Si dangling bonds can combine with H_2O, forming SiOH, or recombine with methyl.

3.5   Conclusions

In summary, FTIR spectra of p-ULK (k = 2.54) films show that Si-C bonds are broken after exposure to 147 nm VUV radiation, creating Si dangling bonds. Furthermore, a high level of SiOH generation and sp^3 carbon loss can be seen when films are exposed to VUV radiation in the presence of O_2. Results suggest that O_2 molecules are interacting with methyl radicals created by VUV radiation, increasing the concentration of H_2O at the reaction site and leading to a greater formation of SiOH. Furthermore, some SiOH bonds generated during exposure are themselves broken, recreating Si dangling bonds. Ambient atmospheric water vapor reacts with remaining Si dangling bonds, leading to an extended period of post-exposure formation of SiOH. Ion pre-treatments that decrease sample near-surface diffusivity also appear to reduce damage by limiting the transport of oxygen, water vapor, and intermediates. The results presented show that VUV photo-generated surface reactions can play an important role in plasma-induced damage of low-k dielectric SiOCH films. Furthermore, the VUV-induced effects are synergistic with molecular O_2. The mechanism for this behavior shows that oxygen is needed to form volatile leaving products.

Chapter 4
The Role of VUV Radiation in Ar/O$_2$ Plasmas

4.1   Abstract

The degradation of porous low-k materials, like SiOCH, under plasma processing continues to be a problem in the next generation of integrated-circuit fabrication. Due to the exposure of the film to many species during plasma treatment, such as photons, ions, radicals, etc., it is difficult to identify the mechanisms responsible for plasma-induced damage. Using a vacuum beam apparatus with a calibrated Xe VUV lamp, 147 nm VUV photons and molecular O$_2$ are shown to damage these low-k materials.   Using Fourier-transform infrared (FTIR) spectroscopy, VUV/O$_2$ exposure is shown to cause a loss of carbon species, resulting in a hydrophilic, SiO$_x$-like layer that is susceptible to H$_2$O absorption, leading to an increased dielectric constant. The effect of VUV radiation on porous SiOCH films, as observed in the vacuum beam apparatus, can be seen to extend to Ar and O$_2$ plasma exposures also. Measurements of dielectric constant change using a mercury probe show consistency with chemical modification inferred from FTIR analysis.   Furthermore, the extent of chemical modification appears to be limited by the penetration depth of the VUV photons, which is dependent on wavelength of radiation. The creation of a SiO$_x$-like layer near the surface of the material, which grows deeper as more carbon is extracted, introduces a dynamic change of VUV absorption throughout the material over time. As a result, the rate of carbon loss is continuously changing during the exposure.   A model is presented that attempts to capture this dynamic behavior and compares the model predictions to experimental data through a fitting parameter that represents the effective photo-induced carbon removal. While this model accurately simulates the carbon loss through VUV exposure by the Xe lamp and Ar plasma, the carbon loss from VUV photons in O$_2$ plasma is only accurately depicted at longer exposure times. Other species, such as oxygen radicals or ions, may play a major role in chemical modification at short times near the surface of the material, while VUV photons contribute to the majority of the damage in the bulk.

4.2   Introduction

Plasma etch and strip processes are important techniques for the treatment of porous low-*k* dielectrics used in the semiconductor industry. While dry-etching processes are essential for fabricating structures at the nanometer scale, plasmas also tend to degrade the mechanical and chemical properties of these low-*k* materials.[3,21] Since plasmas combine the effects of many chemically distinct ions, electrons, photons, radicals, and other reactive species, deciphering the sources of this material degradation can be a difficult task. As a result, many studies have focused on the characterization of changes in material properties through controlling plasma parameters such as gas chemistry, pressure, exposure time, and bias power.[11,22,26,27,63] However, depending on the individual plasma conditions and chamber design in each experiment and the type of porous low-*k* material used, the modification of the material may be different, complicating the comparison of results between studies. Recent studies have attempted to isolate particular components of the plasma discharge, hoping to pinpoint the source of the plasma modification.[29,33,57,64,65] Through these studies, vacuum ultraviolet (VUV) photons and reactive radical species have been shown to be major sources of damage to porous low-*k* materials, providing a guide to understanding how undesirable plasma modification occurs and, if possible, prevented.

In the previous chapter, VUV photons generated from a VUV lamp were shown to damage the porous SiOCH low-*k* material, and upon the addition of un-dissociated molecular oxygen in the background, the chemical modification increased. This was thought to have occurred through a synergistic VUV photon and molecular oxygen relationship, without the presence of oxygen radicals.[66] The extent of chemical modification, through loss of Si-C bonds and growth of silanol (Si-OH) groups, was seen to be significant. In this section, *ex-situ* Fourier-transform infrared (FTIR) spectroscopy and mercury probe measurements were used to examine chemical and electrical property changes due to VUV/O_2 exposure versus well-characterized argon and oxygen plasma discharges. Through this comparison, the wavelength of the VUV photons can be concluded to be an important factor for the rate and depth of chemical modification in the porous low-*k* material. The absorption of VUV photons generally changes over time as the low-*k* material becomes progressively carbon-depleted at the surface, thereby affecting the transmission of photons into the material. This process is also a function of the wavelength of the photons impacting the material. Lastly, a model showing the evolution of photon flux through the p-ULK film and its effect on the decrease of Si-C content over time has been proposed.

4.3   Experimental Setup

Samples of porous SiOCH material, called p-ULK ($k = 2.4$), were used in this study. The films (~220 nm thick), deposited onto a Si(100) substrate by plasma-enhanced chemical vapor deposition (PECVD), were obtained from Novellus, Inc. The porous-ULK material contains one set of small pores from methyl moieties and a second set of larger pores from porogen extraction during the cure process. As a result, the porous-ULK has high pore interconnectivity, which allows for reactive species to easily diffuse into the pores and chemically modify the material.[67]

These samples were placed into two different processing chambers: a vacuum beam system and an inductively-coupled plasma (ICP) system. Exposures performed in the vacuum beam system have been described in the previous chapter.[66] Briefly, the samples (~1 cm^2) were attached to a copper block with thermal paste and secured onto a sample holder. The thermal paste allowed for good contact in maintaining constant temperature of the sample through an external water bath. This sample holder was placed into a transfer-arm region and pumped down before being translated into a stainless steel vessel at 8×10^{-8} Torr. Exposures of 147 nm radiation were performed using a Xe line source manufactured by Resonance Ltd., which has a measured photon flux of 1.3×10^{14} photons/cm^{2}s.[39] During the VUV exposure, O_2 gas was introduced into the chamber at a constant pressure of 10^{-5} torr. An absence of oxygen radicals during these exposures was observed, so chemical modification was purely due to a VUV/O_2 synergistic mechanism.[66] A Hiden Analytical Model HAL-301 Positive Ion Counting Residual Gas Analyzer, operated at electron energy of 70 eV, was used to examine desorption of species from the p-ULK sample during VUV radiation.
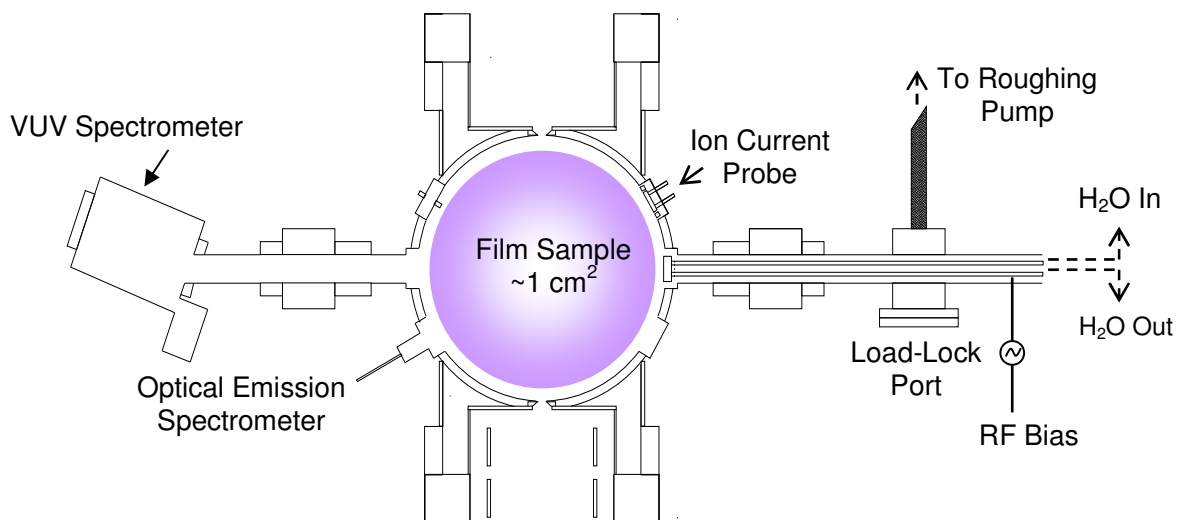
Figure 4.1 Top-down view of the ICP system and diagnostic tools. Plasma conditions are monitored with a VUV spectrometer, optical emission spectrometer, and ion current probe. The samples are placed into the load-lock port and inserted into the main chamber. RF biasing and temperature control is accomplished through the sample holder.

The inductively-coupled plasma (ICP) system, also described in detail previously, consists of a cylindrical, stainless steel chamber, 20 cm in diameter and 10 cm in height.[68] The system schematic is shown in figure 4.1. The ICP system is maintained at a base pressure of 10^{-7} Torr. A Faraday shield between the coil and dielectric plate prevents capacitive coupling. Some advantages of this ICP system are the ability to characterize the plasma conditions (photon flux, ion flux, optical emission, etc.) through instruments attached to the sampling ports on the system.

An optical emission spectrometer (Ocean Optics PC2000-UV-VIS-ISA) is used to monitor emission lines to ensure plasma stability throughout the experiments. The chamber wall ion flux was recorded using a multimeter (Agilent 34410A 6 1⁄2 Digit). The VUV emission lines were recorded using a calibrated Resonance LTD VSFS92 VUV spectrometer. For the purposes of this section, the main focus will be on the effects of VUV radiation, so all plasma exposures were unbiased to minimize the effects of ions. Biasing of the sample holder allows for the introduction of high energy ions, which will be explored in Chapter 6. The faraday shield between the coil and the top dielectric plate minimizes any capacitive coupling from the powered coil, so ion energy impacting the sample is from the floating potential only. This was estimated to be in the range of 15-20 eV for the conditions used in the present experiments. Film samples (~1 cm^2) were placed on a temperature-controlled holder in the load-lock port, and this holder was translated so that the sample was in line with the chamber wall. An external water bath maintained the sample at a constant temperature of 25°C throughout the exposure. Exposures of the sample to Ar, Ar/O$_2$, and O$_2$ plasmas were performed, and table 4.1 summarizes the plasma conditions used in the comparison with exposures in the vacuum beam system. The main wavelengths of VUV radiation emitted by Ar plasma were 104 and 106 nm, while O$_2$ plasma emission is dominant at 130 nm. Ion flux to the substrates was shown to be higher than the total VUV flux of the plasma discharges. Yet, the relatively low energy ions impacting the surface are seen to have little effect on the material due to their relatively low penetration depth.[11]

The bulk chemical effects on the p-ULK samples were examined using *ex-situ* transmission Fourier-transform infrared (FTIR) spectroscopy (Digilab FTS-3000). The integrated FTIR peak was used for the comparison of results. Primarily, the changes in the Si-C peak (1270 cm^{-1}) and the broad Si-OH stretch (3800-3000 cm^{-1}) were examined. These peaks are important indicators of chemical modification and subsequent moisture uptake, both of which drastically affecting the dielectric properties of low-*k* materials.[69,70] A capacitance-voltage (C-V) measurement was also carried out using a Model 802 MDC Three Function Mercury Probe to compare dielectric changes in the p-ULK films to chemical modification.

Table 4.1 ICP conditions used for exposures of p-ULK films and comparison with vacuum beam experiments. Ion flux and VUV flux of varying wavelengths are shown.

Plasma Species	Pressure (mT)	Power (W)	VUV flux (104 nm) ($\times 10^{15}$ cm^{-2} s^{-1})	VUV flux (106 nm) ($\times 10^{15}$ cm^{-2} s^{-1})	VUV flux (130 nm) ($\times 10^{15}$ cm^{-2} s^{-1})	Total Ion flux ($\times 10^{15}$ cm^{-2} s^{-1})
Ar	10	70	1.07 ± 0.35	2.00 ± 0.14	0	5.41 ± 0.05
Ar/O$_2$ (10%)	10	70	0.74 ± 0.03	1.37 ± 0.07	0.22 ± 0.01	3.87 ± 0.03
Ar/O$_2$ (25%)	10	70	0.58 ± 0.02	1.01 ± 0.04	0.35 ± 0.01	3.57 ± 0.02
Ar/O$_2$ (50%)	10	70	0.34 ± 0.01	0.49 ± 0.02	0.37 ± 0.01	3.00 ± 0.01
O$_2$	10	150	0	0	1.11 ± 0.01	5.12 ± 0.01

4.4 Results and Discussion

4.4.1 VUV Characterization

By performing plasma exposures on p-ULK films, the chemical modification by VUV radiation and oxygen species can be studied and compared to previous studies performed in the vacuum beam system. Several control parameters were examined in order to focus on the primary effect of VUV radiation. First, characterization of VUV emissions was necessary in order to determine differences between plasma treatments and vacuum beam experiments. Calculated VUV fluxes were estimated from the VUV spectrometer and are subject to detector/grating efficiencies at different wavelengths. Note that the VUV fluxes are typically much higher in the plasma compared to the Xe source equipped on the vacuum beam system. Because of this, the chemical modification needs to be based on a resulting total VUV fluence or dosage (i.e. the product of flux and time) for comparison.
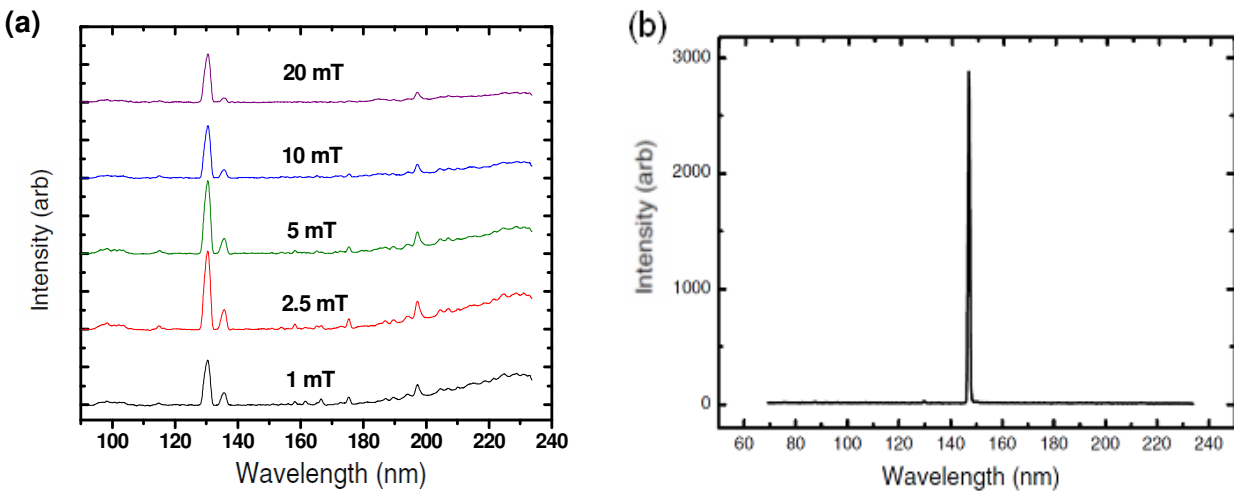
Figure 4.2 The VUV spectrum for *(a)* O_2 plasma at 150 W at various pressures shows a dominant peak at 130 nm. Ionized, excited species produce an emission band between 180-240 nm and is minimized at higher pressures. In contrast, the sole emission line for the *(b)* Xe source is at 147 nm.

Figure 3(*a*) shows the spectra of VUV emission lines for O_2 plasma for five pressures at 150 W. For all pressures, the dominant 130 nm emission line can be seen, with a smaller emission line at 135 nm. For lower pressures, significant emission occurs at wavelengths of 160-230 nm. These emissions are attributed to ionized, excited oxygen atoms that are present due to the higher electron temperatures at lower pressures.[47,71] For comparisons with the 147 nm emission peak (fig. 3(*b*)) from the Xe VUV source, the presence of the emissions from these ionized, excited species complicates interpretation of the results. Furthermore, the absorption coefficient of VUV radiation at different wavelengths varies greatly within this range for SiO_2.[72] Because of this, emissions coming from higher wavelengths must be minimized, so operating at higher pressures was considered. However, higher pressures begin to cause radiation trapping,

as denoted by a drop in intensity of the dominant 130 nm VUV emission line. As a result, the 10 mT plasma condition was chosen as the optimal treatment.

In order to understand and possibly rule out the effects of certain species, plasmas containing a chemically simple species, i.e. argon, were studied. Plasma conditions of 10 mT and 70 W for Ar/O_2 plasma at various oxygen concentrations were examined. A 70 W plasma was used in this case in order to minimize the difference between the VUV fluxes in the plasma exposures and the Xe source. At power settings lower than 150 W, it was noted that plasmas containing mostly O_2 were unstable in this ICP system, likely because the plasma density became too low.

Figure 4.3 shows the spectra of the VUV emission lines for Ar/O_2 plasma mixtures at various oxygen concentrations. For a pure Ar plasma, emission lines at 104 nm and 106 nm are observed. The high intensity peaks at 209 nm and 213 nm have been shown to be detector-induced double-peaks of the 104 nm and 106 nm emission lines.[10,58] With the addition of O_2, a peak at 130 nm was observed, while the Ar emission lines decreased. At higher concentrations of O_2, the O_2 emission line appears to saturate, while the Ar emission lines continue to decrease rapidly. The resulting VUV fluxes, calculated to hit the p-ULK samples, are shown in table 4.1.
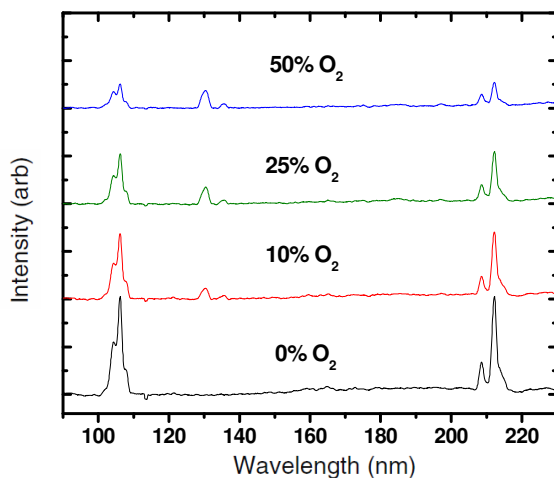
Figure 4.3 VUV spectrum for Ar/O_2 plasma at 70 W and 10 mT for various O_2 concentrations. As O_2 concentration increases, the 104/106 nm emission lines for Ar plasma drop rapidly, while an emission line at 130 nm for O_2 plasma emerges and saturates at higher concentration.

4.4.2 Comparison of Vacuum Beam and Plasma Exposures with p-ULK

Exposures conducted in the ICP system were performed for pure Ar and O_2 plasmas first. Two conditions were initially examined: Ar plasma at 10 mT and 70 W; and O_2 plasma at 10 mT and 150 W. While the study focuses on the role of VUV photons, other species can complicate the study. In the case of O_2 plasmas, oxygen radicals are expected to be generated and possibly affect the samples along with molecular O_2. Although direct measurement of the radical flux was not performed in this system, this issue was addressed later in this section. Vacuum beam

experiments, using the Xe VUV source, were performed at an O_2 background pressure of 10^{-5} Torr. The samples receive only 147 nm VUV photons and molecular O_2 during this vacuum beam exposure, which will be referred to as "VUV/O_2" henceforth. The resulting bulk chemical modifications are examined using FTIR analysis.
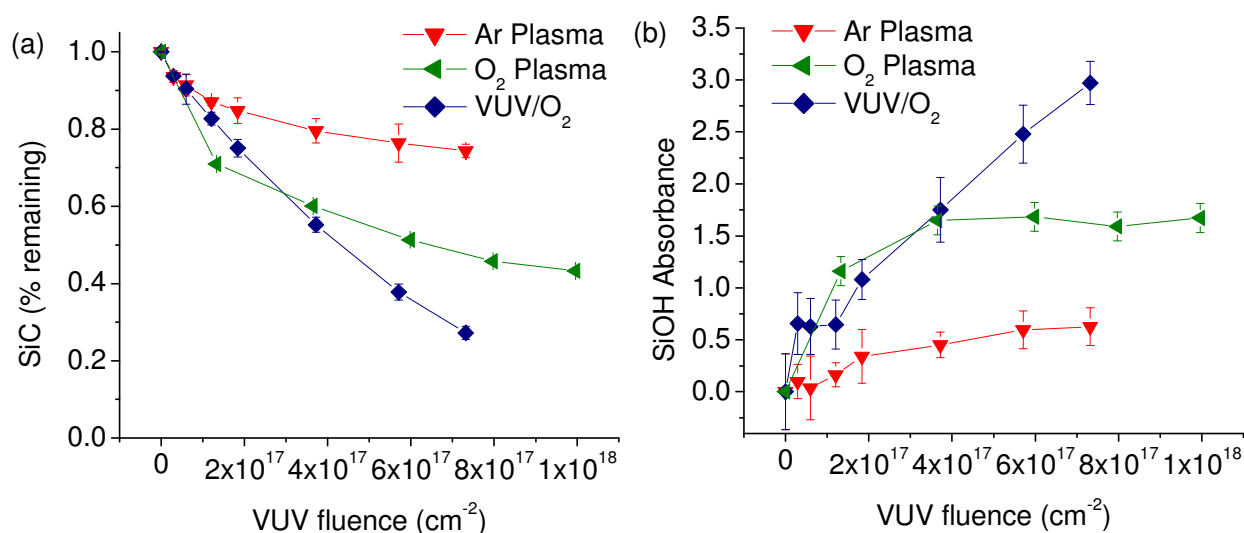
Figure 4.4 Integrated FTIR peak values for *(a)* Si-C content and *(b)* Si-OH absorption in the porous-ULK material as a function of VUV fluence for Ar plasma, O_2 plasma, and VUV/O_2 in the vacuum beam system.

Figure 4.4 plots the changes of the primary peaks of importance (Si-C and Si-OH) as a function of VUV fluence for each case. The changes in the FTIR spectra clearly show that all exposures have a significant effect on the loss of Si-C bonds, which are then reflected by increases in the Si-OH peak. Si-C drop in the low-*k* material indicates removal of carbon species, such as methyl compounds, and has been observed to cause a loss of hydrophobicity. This allows for water vapor to absorb into the material, increasing the Si-OH broad peak.[18,73]

Comparing the relative drops in the Si-C bonds for each case (Ar plasma, O_2 plasma, and VUV/O_2), the loss of carbon species through VUV radiation appears to be significant. The VUV/O_2 case in particular causes the greatest chemical modification, while the O_2 plasma and Ar plasma cases appear to saturate at higher VUV fluences. The trend of carbon loss for the plasma exposures suggests that the VUV radiation does not fully penetrate the low-*k* film in these samples, while the radiation emitted by the VUV source on the vacuum beam system does. When carbon species are lost, the composition of the p-ULK material will change to silicon dioxide. Furthermore, the scissioned methyl radicals closer to the surface of the material will be lost, creating a SiO_x layer that will become deeper over time as more carbon is lost.[19] The absorption of VUV radiation in this damaged, SiO_x layer will be significantly different from the pristine p-ULK material.

While the absorption coefficients remain fairly high for Si-C bonds within the entire VUV regime, this behavior is quite different in the case of Si-O bonds, greatly impacting the transmission of these photons into the material. The penetration depth of VUV photons through amorphous SiO_2 is estimated to be ~10 nm for Ar plasma radiation (104, 106 nm), ~200 nm for O_2 plasma radiation (130 nm), and >2000 nm for VUV/O_2 radiation (147 nm).[9] Consequently, the extent of bulk chemical modification will be different in each case, especially since the film thickness of the p-ULK material is ~220 nm. Secondly, the rate at which the Si-C FTIR peak drops for O_2 plasma exposure appears to be initially much faster than with either Ar plasma or the vacuum beam VUV/O_2 exposure. This increased rate can possibly be attributed to additional damage by atomic oxygen and oxygen ions, which are known to damage low-*k* materials.[12] However, oxygen ions do not travel into the film, and atomic oxygen has been observed to have low penetrability even at significantly high pressures (1 Torr).[65] After an initial drop of ~30%, the rate of carbon loss decreased dramatically, possibly indicating the penetration limit of atomic oxygen. While radical flux was not directly measured, the dissociation fraction [O]/[O_2] has been estimated by Booth *et al.* through the optical emission line at 844 nm to be around 1% at similar power and pressure.[74] Even at 1% dissociation (~0.1 mT), the partial pressure of reactive atomic oxygen can contribute to significant levels of loss in carbon species. While the roles of O radicals and VUV photons from O_2 plasma remain questionable, the next chapter aims to isolate these effects.
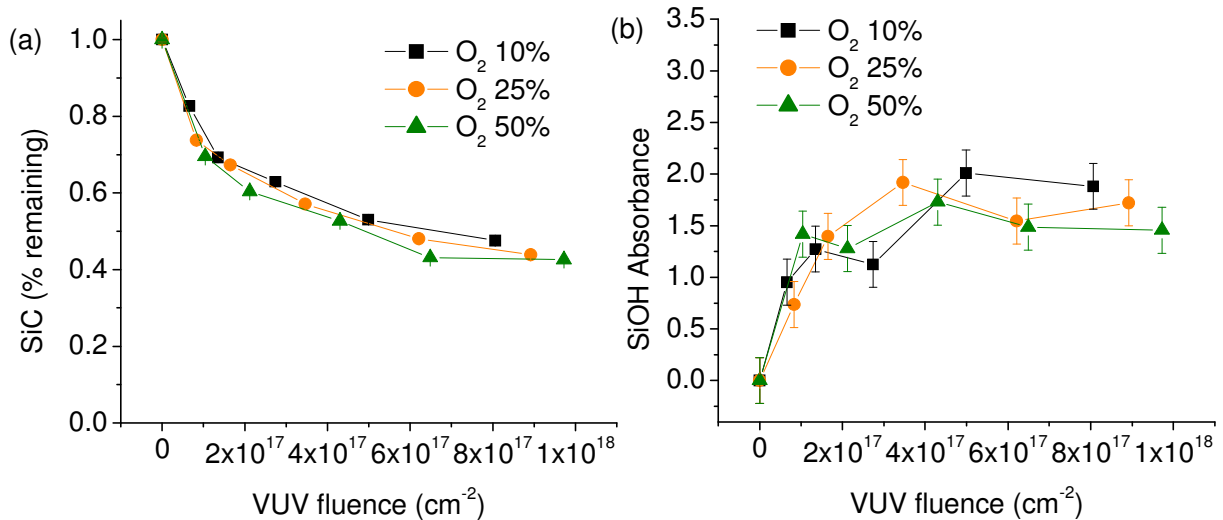
Figure 4.5. Integrated FTIR peak values for *(a)* Si-C content and *(b)* Si-OH absorption in the porous-ULK material as a function of VUV fluence for Ar/O_2 plasmas at 10%, 25%, and 50% O_2 concentration. Note that Si-OH concentration varies due to sensitivity of samples to absorption of water vapor from the atmosphere prior to FTIR analysis.

In order to examine the sensitivity of chemical modification to oxygen concentration, samples of p-ULK were exposed to Ar/O_2 plasma mixtures. The change in the FTIR peaks for Si-C and Si-OH are plotted in figure 4.5 for Ar/O_2 plasma at three oxygen concentrations: 10%, 25% and 50% O_2. Changing the oxygen concentration in this range appears to show little effect

on the rate of chemical modification of p-ULK. Furthermore, the extent of chemical modification appears to be roughly the same as the case of pure O_2 plasma. This result implies that even very low O_2 concentrations are detrimental when treating these low-k films with plasma processes, which is consistent with vacuum beam exposures done previously that used oxygen pressures orders of magnitude lower.[66] Slight increases of carbon loss at higher VUV fluences are observed for higher oxygen concentrations, but this may be due to a slightly higher flux of the 130 nm VUV radiation at these concentrations. Differences in Si-OH increase are more difficult to determine accurately due to the sensitivity of this peak to atmospheric water vapor. Regardless, the increase of the Si-OH peak is in the same range for all O_2 concentrations.

Mercury probe measurements were used as a method to quantify the dielectric damage to the p-ULK material after VUV/O_2 or plasma treatments. Table 4.2 summarizes the relative capacitance increases and estimated dielectric constant increases as compared to a pristine sample at the highest VUV fluences from each exposure. The thickness of the films was assumed to remain constant for these estimates. However, some studies have observed a shrinking effect in the range of 10% of the film after treatment with ultra-violet radiation.[52,64] This film-shrinking effect would translate into an equivalent overestimation of the change in the dielectric constant.

Table 4.2 Capacitance increase as measured by a mercury probe for (a) Ar plasma, (b) Ar/O_2 plasma, (c) O_2 plasma, and (d) VUV/O_2 from the vacuum beam system at similar VUV fluences. Δk was calculated from the increase in capacitance.

		VUV fluence ($\times 10^{17}$ photons/cm^2)	Capacitance Increase	Δk
(a)	Ar Plasma	7.32 ± 0.30	- 7% $\pm$ 13%	- 0.27 ± 0.11
(b)	Ar/O_2 Plasma	8.90 ± 0.83	81% $\pm$ 8%	1.95 ± 0.03
(c)	O_2 Plasma	9.96 ± 1.67	72% $\pm$ 10%	1.82 ± 0.24
(d)	VUV/O_2	7.32 ± 0.30	158% $\pm$ 32%	3.77 ± 0.48

Larger increases in the dielectric constant are observed to occur with exposures that correspond to greater carbon loss and increase in Si-OH. Surprisingly, the Δk for the VUV/O_2 exposure in the vacuum beam system increased beyond the value for SiO_2 ($k = 3.9$) in some cases, likely due to post-exposure absorption of water ($k = 70$), demonstrating the destructive potential of only VUV radiation and molecular O_2. For the O_2 plasma and Ar/O_2 plasma mixtures, nearly equivalent Δk values obtained from the mercury probe measurements agree with the changes in the FTIR peaks for both cases. The dielectric constant after Ar plasma treatment remained similar to the pristine sample, despite a small reduction in the carbon content. While the dielectric constant should increase due to the observed uptake of water, as seen by the increase of the Si-OH peak, it is possible that the Ar plasma acts as a 'curing' process, similar to

ones used for porogen removal to create porous films. The loss in carbon species could create free volume, which decreases k, thereby balancing out any increase of k due to water absorption. Overall, changes in the dielectric constant are shown to follow similar trends as chemical modification from FTIR analysis.

4.4.3 Modeling the Propagation of VUV Radiation Through p-ULK

Since VUV radiation has been determined to be a major contributor to dielectric damage, a transient model for VUV photon penetration has been proposed that can be compared to experimental FTIR results. The absorption of VUV radiation through the p-ULK film is simulated by employing a model where photo-absorption mainly occurs through Si-C and Si-O bonds. Due to the significantly different photo-absorption coefficients for Si-C and Si-O bonds, the transient behavior of the photon flux through the material becomes important because the film composition changes over time. Therefore, to account for this transient photon flux through the film, a net photon attenuation coefficient for the p-ULK material can be estimated based on the chemistry (Si-C, Si-O, and porosity) of the film using equation (4.1). The parameter, $\alpha_i(x, t)$, represents the attenuation coefficient of the respective species (Si-C, Si-O, porosity and total), which can be obtained from literature,[72] and is assumed to control the transient photo-absorption in time and space for the following model:

$$\alpha_t(x,t) = \alpha_{SiC}n_{SiC}(x,t) + \alpha_{SiO}n_{SiO} + \alpha_p n_p \qquad (4.1)$$

$$\frac{dI}{dx} = -\alpha_t(x,t)I(x,t) \qquad (4.2)$$

$$\frac{dn_{SiC}}{dt} = -I(x,t)\sigma_{SiC}n_{SiC}(x,t) \qquad (4.3)$$

The initial relative concentration of each component, n_i, has been estimated as 17.5% for Si-C, 52.5 % for Si-O, and 30% for porosity. The loss of Si-C bonds during VUV exposure leads to changing bond concentration as a function of time and depth of the material, changing the total attenuation coefficient throughout the film over time. From FTIR measurements, little Si-O bond loss has been observed, so changes in Si-O concentration have been assumed to be negligible. The observed slight drops in the FTIR peak in the range of 1200-1000 cm^{-1} associated with the Si-O-Si network and cage structures may be due to the restructuring of these structures into α-SiO$_x$, rather than actual Si-O bond scissioning.[50] Porosity was also assumed to not vary following VUV exposure in this model. Therefore, the total attenuation coefficient will change as a function of carbon loss, which then impacts the VUV flux in equation (4.2). The intensity of the photon flux, I, follows an exponential decay dictated by the attenuation coefficient, which changes as a function of depth, x, and time, t. As the photons penetrate through the film, a portion of the photons scissions Si-C bonds as shown in equation (4.3), creating methyl radicals that are later removed from the film. An effective photolysis cross-

section for the loss of Si-C, σ_{SiC}, can be fitted to describe the rate of carbon removal, which can then be compared to the total Si-C loss from experimental results.
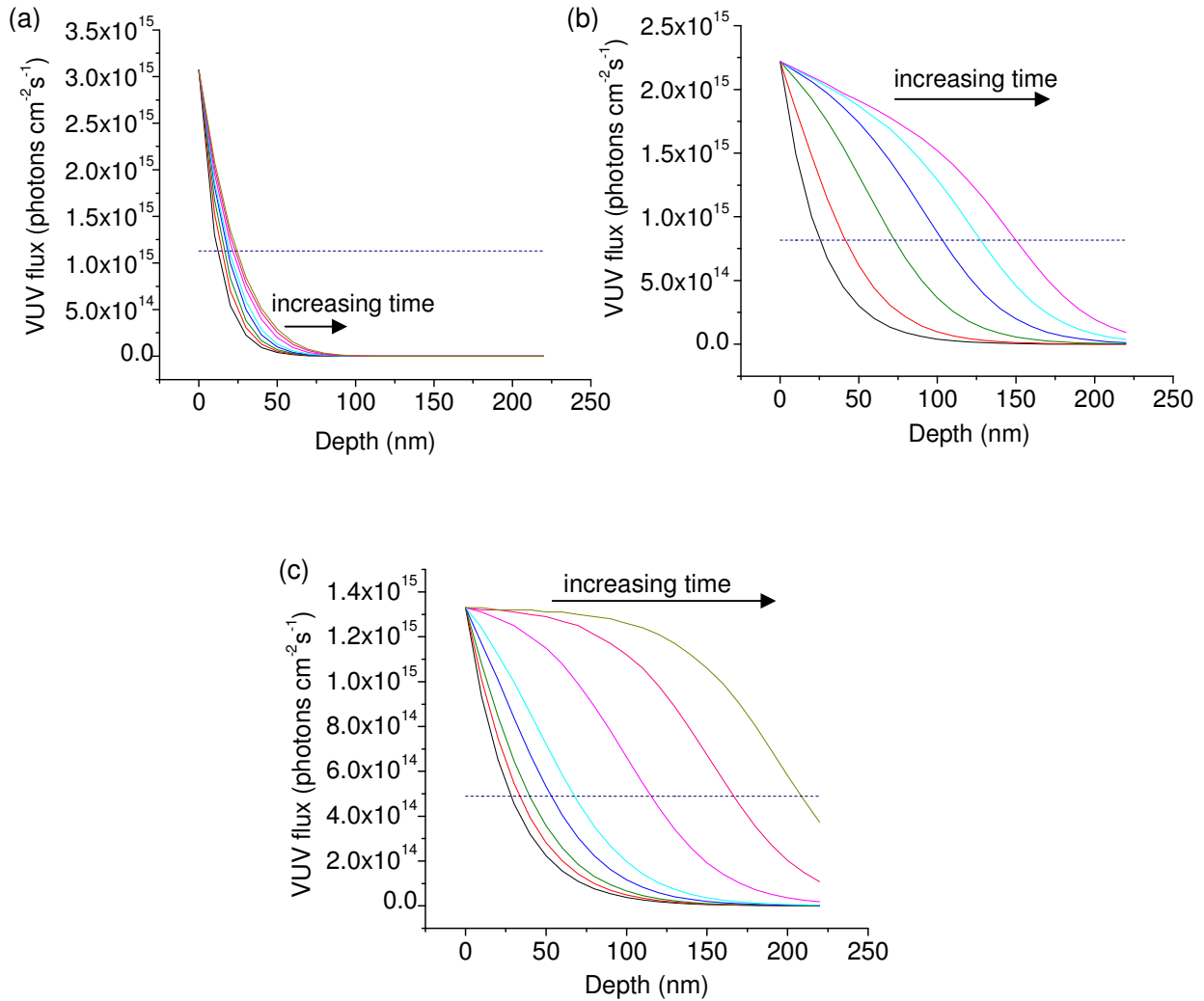
Figure 4.6 Transient profile of VUV flux as a function of depth in the p-ULK film for *(a)* Ar plasma, *(b)* O$_2$ plasma, and *(c)* the Xe source as predicted by the model. The horizontal dotted-line denotes the 1/*e* penetration depth.

Figure 4.6 shows the model predictions for the intensity of the VUV flux as it penetrates through the p-ULK film for Ar plasma, O$_2$ plasma, and the Xe source, respectively. By increasing the photon wavelength used in the exposure, the VUV intensity decays more slowly and penetrates deeper into the film. Yet, the energy of these photons is high enough to scission Si-C bonds for all of these cases, which results in a change in the Si-C concentration. Initially, the penetration depth is < 30 nm for all exposures because of the relatively high Si-C absorption cross section. As Si-C is lost over time, the film composition changes, so the photons penetrate

41

through a modified, SiO_x-like surface layer. The absorption coefficient for this SiO_x layer is higher for VUV wavelengths < 120 nm,[9] which means that photons generated from Ar plasma will continue to be mostly absorbed near the surface, as seen in figure 4.6(a). For O_2 plasma and the Xe source, photons penetrate deeper into the SiO_x surface layer and scission Si-C bonds deep within the film, increasing the depth of the modified layer. The depth profiles of the Si-C concentration in figure 4.7 reflect the relative VUV penetration for each case. From this model, the effective $1/e$ penetration depth for the porous-ULK material can be approximated as a function of VUV wavelength and fluence, as noted by the horizontal, dotted lines in figure 4.6.
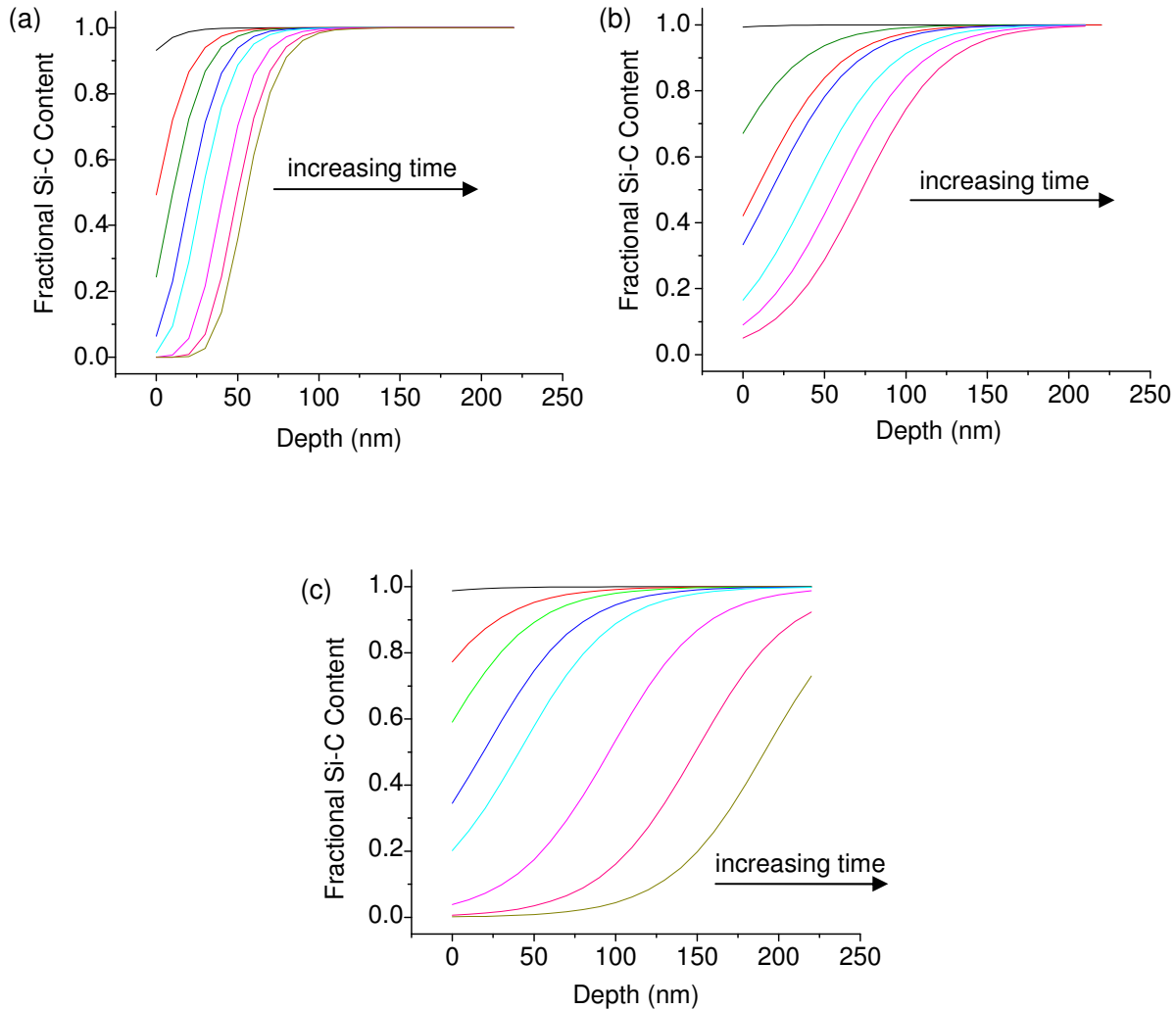
Figure 4.7 Transient profile of the Si-C content as a function of depth in the p-ULK film for *(a)* Ar plasma, *(b)* O_2 plasma, and *(c)* the Xe source as predicted by the model. As Si-C content is lost, the film converts into a SiO_x-like material.
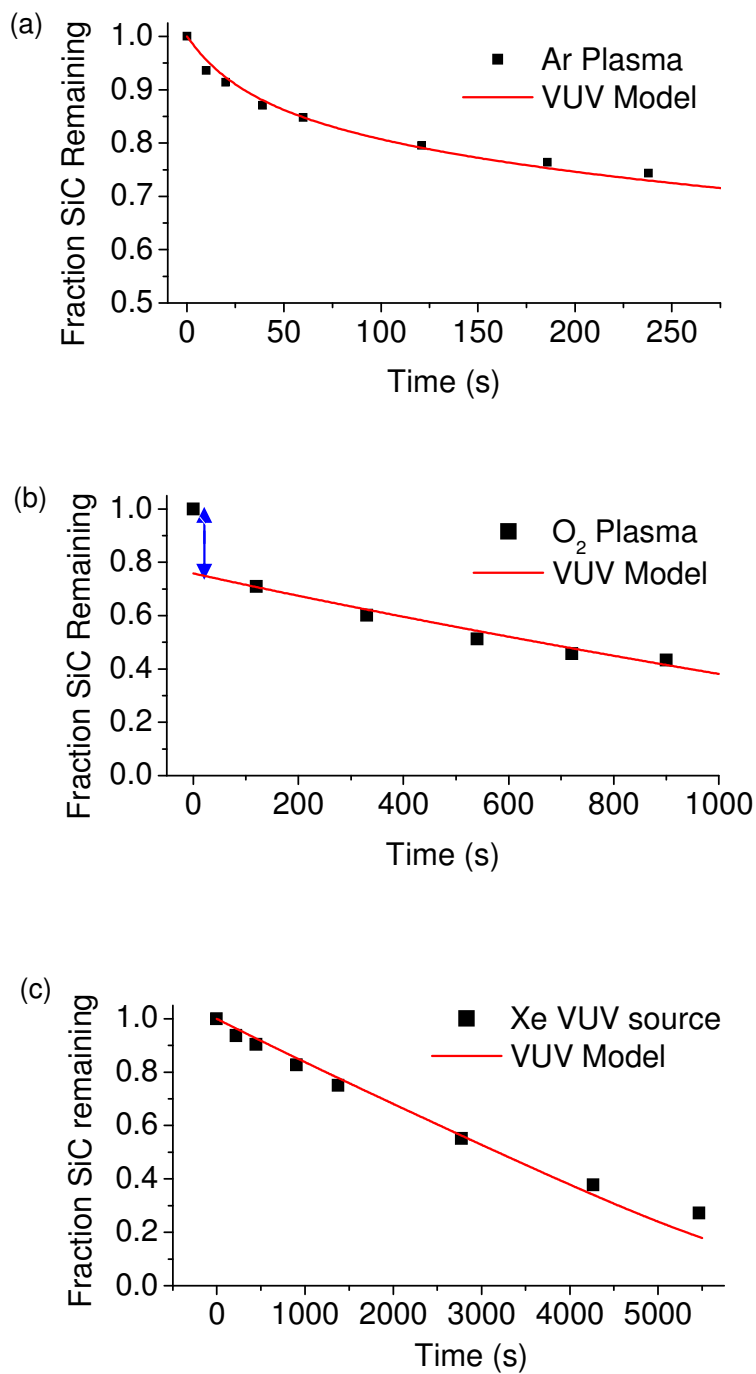
Figure 4.8 Comparison of model results for the bulk Si-C content to experimental exposures for *(a)* Ar plasma, *(b)* O_2 plasma, and *(c)* the Xe source as a function of time. While the VUV penetration model fits well for Ar plasma and the Xe source, other species in O_2 plasma may be contributing to the initial rapid drop observed.

By integrating the Si-C concentration throughout the entire depth of the film, the bulk concentration of Si-C obtained from the model can be quantitatively compared to the corresponding experimental studies as shown by carbon loss from FTIR measurements. Figure 4.8 shows the comparison between the model and the experimental results for all three cases. For Ar plasma and the Xe source, the fitted photolysis cross sections used in the model were $\sigma_{SiC,Ar} = 2.3 \times 10^{-17}$ cm^2 and $\sigma_{SiC,Xe} = 8.8 \times 10^{-18}$ cm^2. A smaller cross section for photons from the Xe source versus Ar plasma is consistent with studies examining the penetration of these photons in polymer materials.[68,75] The model shows good agreement with the experimental results for these two cases. In contrast, the model examining the effect of VUV photons in O$_2$ plasma was shown to be more complicated. While the model could be used to find an adequate fit of the later exposure times, with $\sigma_{SiC,O} = 3.1 \times 10^{-18}$ cm^2, the initial drop in the Si-C content cannot be accounted for by photons alone. This initial drop is likely due to the presence of other reactive species that are only present in O$_2$ plasma, such as oxygen radicals or low energy ions. At this point, the effect of these species on Si-C loss could not be independently measured in the experimental setup. From the model, it appears that these species only have an effect at short times near the surface, implying that their penetration depths are relatively low compared to the 130 nm VUV photons. As the modified layer grows, these species are likely quenched before reaching carbon species contained deeper in the film. As a result, the effect of VUV photons mainly occurs at longer exposure times, while the effect of other species dominates at short times for O$_2$ containing plasmas.

Fitted photolysis cross-sections were compared to the absorbance cross sections for silicon carbide found in the literature. The reported cross sections were on the order of $(8-10) \times 10^{-17}$ cm^2 for VUV wavelengths between of 104 nm and 147 nm.[72] The fitted cross-sections for Si-C loss show quantum yields of between 10-25%, depending on wavelength. Furthermore, this model does not account for effects of molecular oxygen. The amount of oxygen present during the VUV exposure has been shown to affect Si-C loss rates as a function of pressure,[66] possibly leading to changes in the photolysis cross-section. However, it was found that relatively low partial pressures are needed to saturate photo-generated reaction sites. The model may be improved by incorporating the effect of other bonds observed in the p-ULK material to understand their impact on photon penetration. Furthermore, the effect of film shrinking and structural rearrangement under photon exposure has yet to be explored.

4.5   Conclusions

P-ULK dielectric films were processed under vacuum beam conditions, where exposure was limited to VUV photons and molecular O$_2$, and with Ar/O$_2$ inductively-coupled plasmas. The chemical modification from these exposures was examined with FTIR spectroscopy, and the contribution of damage from VUV radiation was found to be significant. Through characterization of the VUV spectrum, the wavelength of these VUV photons from each exposure was found to be an important parameter in determining the extent of film modification. Ar plasma exposure, emitting 104 and 106 nm wavelength photons, was observed to mainly contribute to near-surface modification. In contrast, O$_2$ plasma (130 nm) and the Xe source (147 nm) caused modification through the majority of the film. With Ar/O$_2$ plasma mixtures, even an O$_2$ concentration of ~10% affected the films in a manner similar to a pure O$_2$ plasma exposure.

Evidently, the carbon loss is sensitive to any oxygen present in the background, probably because methyl radicals scissioned from VUV radiation can react with O_2 to remove them from the film. As a result, the film becomes increasingly hydrophilic, which causes water absorption when the samples are exposed to the atmosphere. Increases in the dielectric constant, as measured by the mercury probe, are consistent with this theory.

Through a simple photolysis model, the transient effect of the VUV photons and the decrease of the carbon concentration in the film over time can be predicted. Using absorption coefficients obtained in literature, the VUV flux profile through the p-ULK material can be seen to change over the duration of the exposures for VUV wavelengths of 130 nm and 147 nm, while remaining relatively constant for 104/106 nm wavelength radiation from Ar plasma. As a result, the higher wavelength photons penetrate more deeply into the material, modifying the entire film. By integrating the Si-C bond concentration over the entire depth of the film at various points in time, the total Si-C content from the model was compared to experimental results through a fitted parameter for the photolysis cross section of Si-C. This fitted parameter was found to be reasonably close to absorption cross-sections reported in literature. While the model accurately simulated the behavior of VUV photons from Ar plasma and the Xe source, O_2 plasma proved to be more complex, likely due to the presence of other reactive species. However, these reactive species appear to contribute mainly to the modification of the near-surface, while VUV radiation is possibly the major concern of bulk modification.

Chapter 5
Separation of Plasma Species to Study Individual Effects on Low-k Materials

5.1   Abstract

One important class of low-k materials used as interconnect dielectrics employ methyl groups added to nanoporous SiO_2 matrices. These carbon-doped oxide materials are known to be susceptible to damage from plasma species during various stages of plasma processing. Two key active species generated in O_2 plasma are oxygen radicals (O) and vacuum-ultraviolet (VUV) photons. These species are known to cause carbon loss, resulting in damaging increases in dielectric constant throughout the film. However, the mechanisms through which this damage is incurred are poorly understood. By capping the substrate in different ways during plasma exposure, it is possible to expose films to either photons alone or O atoms alone. This chapter reports measurements of damage induced by VUV photons only; O radicals only; and the combination of O radicals and photons. Through HF stripping, it is noted that carbon extraction from photons and from radicals yields different outcomes; the profile of carbon concentration within the modified region is different for each case. Damage from photons alone can be modeled and model predictions are in good agreement with measurements. Damage from O atoms alone can only be modeled if it is assumed that the near-surface region has a significantly reduced diffusivity compared to the bulk of the film. Experiment and model agree that both photons alone and O radicals alone damage the material by removing carbon. When radicals and photons are present simultaneously during plasma exposure, however, more carbon removal appears to be occurring in the model than experimentally observed. Remarkably, if only radicals are exposed to the film after short (10 – 30 second) plasma exposures, very little additional damage is incurred during this radical-only exposure. The most straightforward interpretation of these results appears to be that photons combine synergistically with radicals in the pores to narrow the pores, thereby reducing film diffusivity in the carbon-poor, plasma-damaged regions.

5.2   Introduction

Implementation of nanoporous low-k materials into interconnect technology has undergone numerous hurdles due to the chemical modification of the dielectric material after plasma processing. Plasma exposures used for various processes such as etching, stripping, and cleaning, are well known to cause damage to low-k materials, leading to failure of semiconductor devices.[7,26,27]   Furthermore, the introduction of nanoporosity to further lower the dielectric constant has allowed damaging, reactive species to travel even deeper into the material. Investigations of plasma-induced damage has attracted keen interest, and new plasma processing techniques for this material are often targeted at finding conditions or chemistries that minimize damage. For example, O_2-containing plasmas are well-established as being the most damaging and are, as a result, usually avoided. Most studies have attributed damage to the actions of highly reactive oxygen radicals that are responsible for oxidizing carbon species that have been doped into the material to lower the dielectric constant.[12,65,76] Because of this, investigators have tried to shift to less reactive plasma chemistries.

Reducing plasma chemistries, such as N_2/H_2 plasmas, have been investigated as an alternative to oxidizing chemistries. However, plasma-induced damage also occurs for these exposures, albeit at slower rates.[21,22,32] Plasma chemistries using fluorocarbon containing gases have also been explored. However, polymer build-up on the surface of the low-k material post-treatment complicates later processing steps.[77-79] By changing plasma chemistry, the effect on the material post-plasma treatment can change dramatically, yet fundamental mechanisms have not been widely investigated. There is still much that needs to be understood about the effects of individual plasma species and their interactions with porous low-k materials. Radical species are not the only plasma-generated species that can cause modification. Vacuum ultraviolet (VUV) photons are known to be a significant source of chemical modification and have been shown to cause significant damage to low-k materials.[57,66,80]   By changing the gas chemistry, the wavelength of photons coming from the plasma changes. This in turn alters the level of photo-chemical modification, depending on how easily the photons pass through the material.[9,81] High energy ions impacting surfaces can also play different roles.   At certain energies, ion bombardment has been shown to suppress plasma-induced damage, apparently by densification of the surface of a low-k film, which may impede subsequent diffusion of damaging reactive species.[82] With the simultaneous interaction of these species, it is difficult to identify how each component affects the low-k material.   As a result, even plasma exposures using the same chemistry can yield varying outcomes based on the plasma conditions (e.g. power, pressure, gas flow, etc.).

The focus of this chapter is to explore how individual plasma species interact with low-k materials, particularly oxygen radicals and VUV photons, and whether the impact of these species on low-k films can be generalized in the form of a mathematical model. In order to achieve this goal, a method designed to filter certain plasma species, created in an inductively-coupled plasma, allowed for observation of the individual effects of either oxygen radicals or VUV photons. Plasma damage was measured by noting the change of the Si-C bending peak (~1270 cm^{-1}) using Fourier-transform infrared spectroscopy (FTIR). This was assumed to be proportional to the rate of carbon removal by either radicals or photons. By examining the change of the FTIR peaks before and after removing the damaged portion of the film using a dilute HF solution, the penetration of radical and photon damage into the film was observed to

occur in different ways. Using these experimental results, models were developed to predict the removal of carbon species from the low-*k* film as a function of dose of either radicals or photons. These models appear to accurately predict carbon removal for a wide range of plasma conditions for these species acting individually. However, it was found that the prediction of plasma-induced damage cannot be obtained by simply combining these two effects. This chapter discusses the implications of these observations and suggests steps to better understand the complex interactions occurring at surfaces exposed to plasmas relevant to the challenge of minimizing plasma-induced low-*k* damage.

5.3   Experimental Setup

Samples of p-ULK (*k* = 2.4) blanket films, 230 nm in thickness, deposited onto a Si substrate were used as the low-*k* material in the following experiments. This material is an organosilica glass, containing high porosity (~30%) and high pore interconnectivity, allowing for diffusion of gaseous species into the film.[83] Small wafer samples, measuring ~ 1cm^2, were cut and used for all exposures. In order to achieve photon-only or radical-only exposures, special sample holders were designed to isolate the sample from other plasma species. These samples holders are composed of a circular copper stand and Teflon cylindrical caps, screwed onto the copper stand, to block out certain plasma species. A diagram of the cross-sectional view of the sample holders is shown in figure 5.1. More details of this setup are provided in Appendix A.
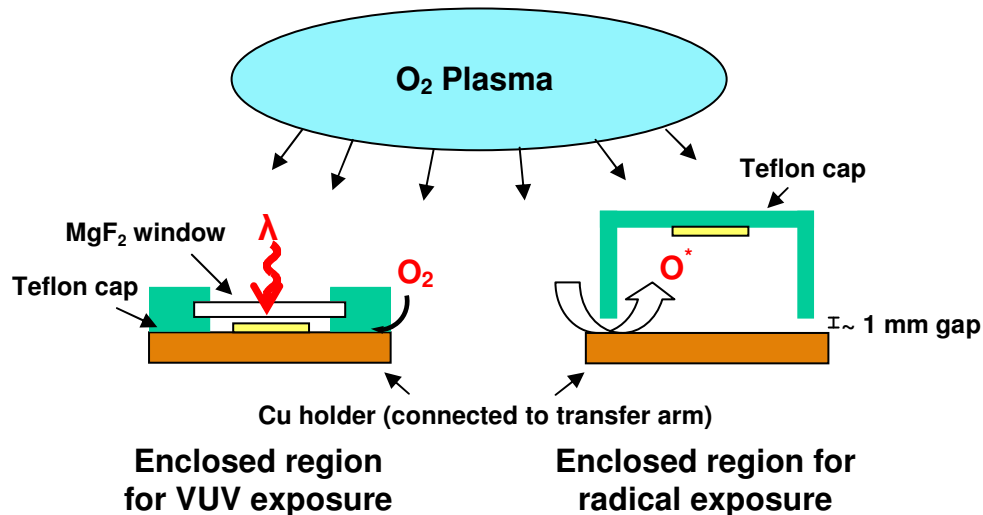
Figure 5.1 Cross-section view of the cylindrical sample holders used for VUV and radical exposures. Low-*k* film samples are placed into these sample holders and transferred into the ICP system. VUV photons from O_2 plasma can pass through the MgF$_2$ window to the sample (left), while oxygen radicals diffuse through a 1.5 mm gap to the sample inverted underneath the cap (right), allowing for exposure of isolated species. Molecular O_2 can diffuse into the region in both cases.

In the case of photon-only exposure, the sample is enclosed inside an isolated region, behind a MgF$_2$ window that is held in place by the Teflon cap. The MgF$_2$ window is only transparent to VUV photons with emission wavelengths above 115 nm. For O$_2$ plasma, the main emission line of importance is at 130 nm. The region inside the cap is not airtight, allowing for molecular O$_2$ to leak inside, yet the aperture is small enough to block out the great majority of oxygen radicals. By replacing the MgF$_2$ window with a stainless steel plate, no chemical modification was observed in the samples, concluding that radical species are unable to reach the p-ULK film. For radical-only exposures, the sample was placed within an elevated Teflon cap, so that only molecular O$_2$ and oxygen radicals can diffuse into the region through a small slit (~1.5 mm), while other line-of-sight species are blocked. The sample can be further covered with a MgF$_2$ window while in this configuration to examine for residual photon exposure. A lack of chemical modification observed here ensured that VUV photons do not reach the p-ULK film during the radical-only exposure. Other studies have used similar techniques in order to achieve isolation of either photons or radicals.[33,84,85]

Low-k samples placed into the holders were first mounted onto a transfer arm, pumped down, and transferred to the main chamber of an inductively-coupled plasma (ICP) system. This system consists of a cylindrical, stainless steel chamber, 20 cm in diameter and 10cm in height.[81] The ICP system is maintained at a base pressure of 10^{-7} Torr, and a Faraday shield between the coil and dielectric plate prevents capacitive coupling to the plasma. For all exposures, O$_2$ plasma was used at an input coil power of 150 W. Pressures of 1.5, 10, and 30 mTorr were used, yielding different photon and radical fluxes. While the flux of VUV photons can be measured using a calibrated Resonance LTD VSFS92 VUV spectrometer mounted on the side of the chamber, accurate estimation of the atomic oxygen concentration is not currently available. O atom density was estimated to be on the order of 10^{12} cm^{-3}, based on previous measurements made in the same system.[86] Due to the presence of a Faraday shield between the coil and the top dielectric plate, there is little capacitive coupling from the coil to the plasma. The plasma potential is therefore pinned near the floating potential since the chamber walls are mostly grounded. As a result, the impacting ion energy at the substrate surface should be at or near the plasma floating potential, which is estimated to be about 15-20 eV. At this relatively low energy, the effect of ions can likely be ignored for plasma exposures due to their low penetration ability. Since even energetic ions typically penetrate less than 1 nm, the direct effects of ions on a film several hundred nanometers thick is restricted to the very near surface. At energies above about 100 eV, ion bombardment can make a significant difference to plasma-induced damage in p-ULK films.[29,66] These effects are likely due to changes in surface porosity, but in any case, ion impact energy in the experiments reported here are much lower than this.

Bulk chemical changes on the p-ULK samples were examined using *ex-situ* transmission FTIR spectroscopy (Digilab FTS-3000). The integrated FTIR peak at 1270 cm^{-1}, the Si-C bending peak, was used as the main indicator of carbon content remaining in the film. Measured absorbance values for all exposed samples were compared on a fractional basis to the pristine, as-deposited blanket films. HF stripping of the modified region and analysis of the broad peak for the Si-O-Si network in the range of 950-1250 cm^{-1} were also performed to estimate the depth profile of the damage. This technique can yield an estimation of how much carbon is removed within the near-surface modified region, indicating the gradient of the carbon concentration as a function of depth. As will be shown, the depth profiles of damage from radical-only exposure and from photon-only exposure are significantly different.

5.4   Results and Discussion

5.4.1   Low-*k* Damage from Exposure to VUV Photons and Oxygen Radicals

In this section, the damage effects of VUV photons and oxygen radicals, isolated from O_2 plasma, on p-ULK blanket films will be shown. The fraction of carbon loss from the entire film is typically used to characterize the extent of plasma-induced damage. But as noted above, the penetration depth of this carbon removal, along with the profile of carbon left behind in the modified region, provides more complete information regarding the degree of film damage. By stripping this modified region with a dilute HF solution, differences between photon-induced damage and radical-induced damage can be observed.

5.4.1.1 HF Strip as a Technique for Depth-Profiling

After plasma processing, carbon species are selectively removed from low-*k* films via volatile products, while leaving the Si-O-Si network intact. As a result, the affected region of the film converts into a SiO_x modified layer.[87] HF stripping is typically used after plasma processing for patterned wafers in order to remove the hydrophilic SiO_x region. If not removed, this region will attract water vapor and increase the film dielectric constant. The benefit of using a dilute HF solution is that the SiO_x layer can be readily removed, while the pristine, unmodified layer underneath remains mostly untouched.[56] Ideally, the underlying material composition should be the same as the pristine material before plasma processing. This can be tested by examining the Si-C bending peak (1270 cm^{-1}) and the Si-O network (950-1250 cm^{-1}) in FTIR. In an unaltered film, the ratio of changes in these peaks should be similar.

Figure 5.2a shows the change in the normalized peak intensities of Si-C and Si-O after O_2 plasma exposure at 150W and 10 mTorr as a function of exposure time. Samples of p-ULK were subjected to O_2 plasma at various intervals for up to 30 minutes. While the Si-C peak drops with time, there is little change in the Si-O peak. The small drop for the Si-O peak is reportedly caused by the removal of carbon from the Si-O-Si network, causing network restructuring rather than physical loss of Si-O bonds.[87] Afterwards, each of the samples were submerged in a ~1% HF solution for 1 min. Figure 5.2b shows the resulting change of the Si-C and Si-O peaks after the HF strip.   While both FTIR peaks drop significantly after the HF strip, it appears that the ratio of the intensities is roughly equal, signifying that the remaining portion is similar in composition to the pristine material, minus a change in film thickness.[56] There is some deviation between points, but this could be due to variation in sampling. By using the fraction of Si-O remaining in the film and the original film thickness, the modification depth can therefore be estimated. Another major point to note is the drop of the Si-C peak caused by HF stripping. The carbon removed by the HF strip is mainly the carbon remaining within the modified region. This brings up the question of the tolerance of carbon loss that is necessary before the region becomes vulnerable to the HF solution. This point will be addressed later in the modeling portion.
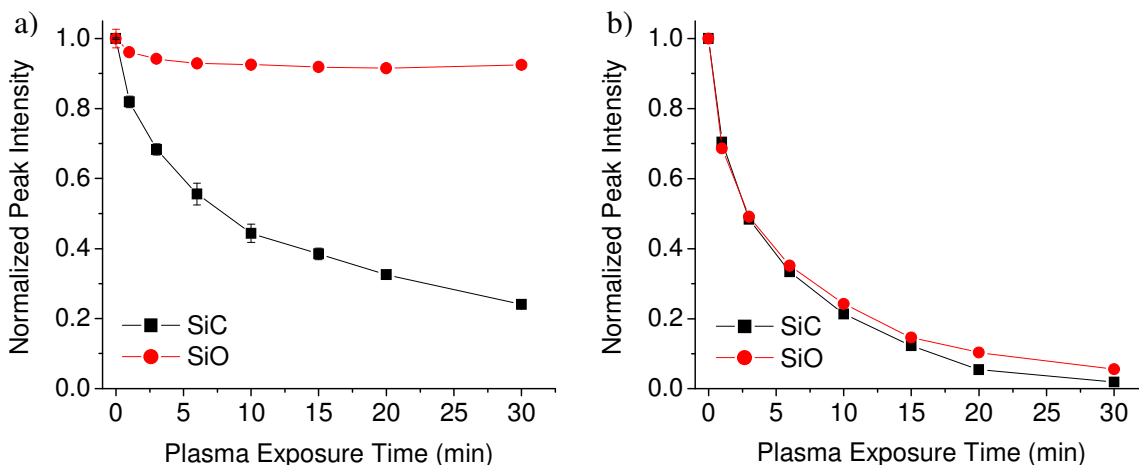
Figure 5.2 The integrated FTIR peaks for SiC (1270 cm^{-1}) and SiO (950-1250 cm^{-1}) as a function of O$_2$ plasma exposure time (a) directly after plasma exposure and (b) after the HF strip. Plasma conditions of 10 mTorr and 150 W were used.

5.4.1.2 Effect of VUV Photons

Many parameters must be considered in understanding damage caused by VUV photons. VUV photons are believed to cause Si-C bond scissioning, yet it has been observed that other species are required in order to permanently remove the carbon species from the film. These carbon species, typically terminating –CH$_3$ groups, need to react with background gases in order to form volatile species. Under vacuum, small amounts of water vapor can cause this reaction, but this can be enhanced by the presence of molecular oxygen as well. In fact, only a small background of oxygen is needed to completely saturate the photolyzed reaction sites.[66] When enclosing the p-ULK film sample, analysis needs to be performed to ensure that the VUV effects remain the same within the cap. There needs to be enough molecular oxygen inside to saturate the reaction sites, yet the aperture must be able to block oxygen radicals. Another issue is that the VUV flux arriving at the film surface changes at different plasma pressures. At pressures of 1.5, 10, and 30 mTorr, the respective VUV fluxes were measured to be 1.3, 1.0, and 0.6 × 10^{15}cm^{-2} s^{-1}. At higher pressures, molecular absorption and subsequent collisional quenching occurs, lowering the effective VUV flux at the film surface. Furthermore, since the VUV photons have to pass through the MgF$_2$ window to impact the sample, the flux is reduced by less than complete window transparency. Window transparency was found to be ~46% by placing the MgF$_2$ window in front of the spectrometer.

First, the effect of different O$_2$ pressures on photon-induced carbon removal from the p-ULK films was examined. Exposures were conducted in the ICP system with the photons-only configuration under these three pressures. In order to make a proper comparison, changes in the Si-C peak magnitude were plotted against VUV fluence, as seen in figure 5.3. When plotted with VUV fluence, there is little observed difference in the rate of carbon removal. Therefore, the reaction sites appear to be saturated sufficiently with O$_2$ even at the lowest pressure such that changes in the background pressure affect the reaction minimally. As a result, the damage

caused by VUV photons in this case can be generalized to occur as a function of VUV dosage (equivalently, fluence) only, thereby simplifying the interpretation.
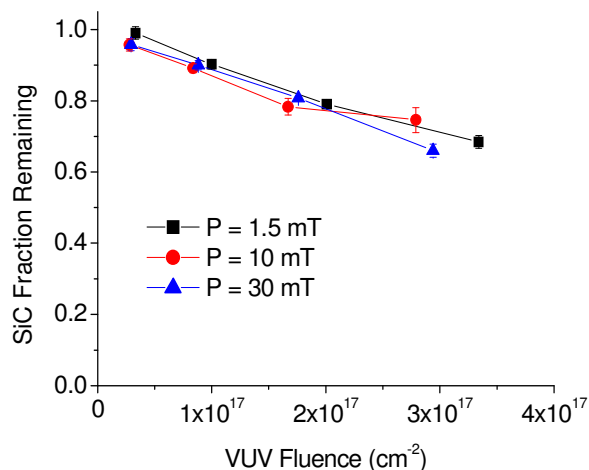
Figure 5.3 Fraction of SiC remaining in the film as a function of VUV fluence. O_2 pressures of 1.5, 10, and 30 mTorr were used, yielding different VUV fluxes. Because of this, exposures were compared based on total VUV fluence.
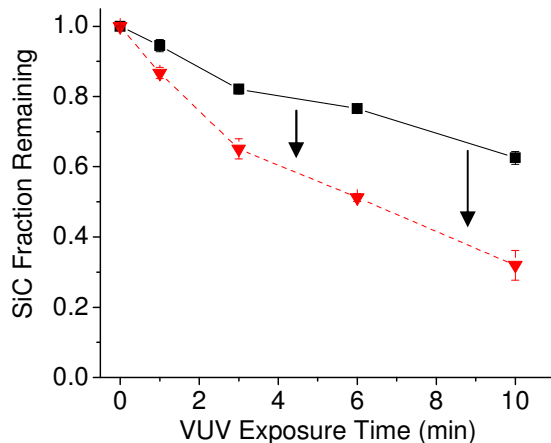
Figure 5.4 Fraction of SiC remaining in the film as a function of VUV exposure time. O_2 plasma conditions of 10 mTorr and 150 W were used. The solid line shows carbon removal after VUV exposure, whereas the dotted line shows a drop in carbon from the HF strip. A large amount of carbon is lost during the HF strip, indicating that removal of carbon by VUV gradually occurs through the bulk of the film.

For this reason, further analysis concentrated on samples exposed to VUV photons under a single plasma condition (10 mTorr, 150 W). Figure 5.4 shows the fraction of Si-C remaining as seen in FTIR after VUV exposure of up to 10 minutes, as denoted by the solid line. The subsequent HF strip caused a significant removal of carbon species, dropping the curve to the

dotted line. As mentioned earlier, HF stripping likely removes residual carbon that remains within the damaged/modified layer. Since a relatively large amount of carbon was shown to be removed in this manner, it appears that the VUV photons (130 nm) do not photolyze all Si-C bonds. In other words, the material is fairly transparent to photons of this energy. This results in photons penetrating and removing carbon deep in the bulk of the film, which is in agreement for estimations seen in literature.[9] However, this also implies that exposure to VUV photons creates carbon density profiles within the damage layer in which C varies relatively gradually. As observed later, this profile is also seen in the model of photon-only removal.

5.4.1.3 Effect of Oxygen Radicals

Due to the orientation of the radical-only sample holder, the magnitude of oxygen radical flux to the film surface was difficult to estimate. Oxygen radicals generated from the O_2 plasma diffuse through the 1.5 mm slit to impact the sample located on the underside of the Teflon cap. As a result, these radicals undergo multiple surface collisions before colliding with the sample, instead of directly impacting the sample as in the case of a direct plasma exposure. These radicals would similarly undergo numerous collisions while diffusing through the porous network of the p-ULK film. Since it has been observed that oxygen radicals can travel deep into porous low-k films, the lifetime of these radicals appears to be fairly long.[65] Consequently, the presence of the relatively unreactive Teflon cap is not likely to hinder the flow of radicals into the isolated region.
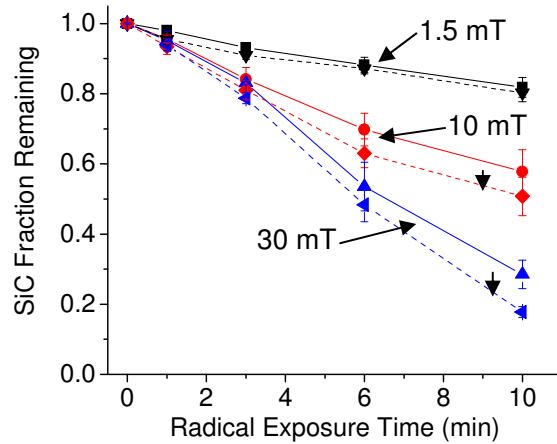
Figure 5.5 Fraction of SiC remaining in the film as a function of radical exposure time. O_2 plasma pressures of 1.5, 10 and 30 mTorr, and a power of 150 W were used. The solid lines show carbon removal after radical exposures, whereas the dotted lines show drops in carbon from the HF strips. Only small amounts of carbon are lost during the HF strip, signifying that the modified layer is mostly carbon-free.

Radical exposures were performed in this manner with O_2 plasma pressures of 1.5, 10, and 30 mTorr. Figure 5.5 shows the resulting fraction of carbon remaining as seen in FTIR after radical exposures of up to 10 minutes, as denoted by the solid lines. At higher pressures, the concentration of oxygen radicals increases, causing higher rates of carbon loss. The rate of carbon loss appears to show an almost linear trend with exposure time, which normally indicates that O radical diffusion and carbon removal is not a diffusion-limited process. Other studies have also observed similar trends when examining radical-only exposures.[65,88] However, damage region propagation results obtained from HF stripping show that very little carbon was removed from these films, indicating that the SiO_x modified layer etched by the HF strip is nearly carbon-free. This result implies a relatively sharp front of carbon and therefore a diffusion-limited removal process. This seems to contradict the conclusion reached with the removal rate of the carbon observed in figure 5.5. One explanation for this apparent inconsistency could stem from an inherent resistance for diffusion at the surface of the film, effectively slowing down diffusion and changing the carbon removal rate.

From these profiles obtained through the HF strip, a significant distinction has developed between photon-induced damage and radical-induced damage as shown in figure 5.6. The SiO_x modified layer develops in different manners in exposures involving solely VUV photons or radicals. VUV exposure causes removal of carbon throughout the depth of the film, which is dictated by the rate photons are absorbed by the film. This results in a relatively gradual depletion of carbon throughout the film rather than the sharp front of a propagating damaged region. In contrast, radical exposure appears to fully deplete the carbon from the film layer-by-layer, as the radicals slowly diffuse into the film, removing carbon and being lost in the process, forming various reaction products. As a result, there is apparently a relatively sharp front of carbon-depleted modified layer that grows deeper with time. Before attempting to understand how these two effects act in concert, models were developed that can quantitatively predict the damage progression in each case with only a single damage-causing agent.
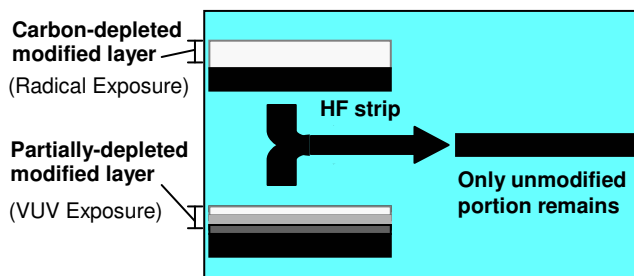
Figure 5.6 Schematic of radical and VUV-induced damage on low-*k* films. The carbon profile versus depth is different for each case. After HF stripping, only the unmodified portion remains.

5.4.2 Modeling Carbon Removal by Photons and Radicals

The objective of this section is to demonstrate that the effects of photons alone or radicals alone can be modeled in a relatively simple fashion. These models take advantage of plasma parameters that are measurable, such as photon fluxes or radical concentrations, and inherent properties of the film, like absorption coefficients and reaction/diffusion rates. In principle, the model can predict damage from plasma/material interactions regardless of differences in plasma settings. Comparison with measurements allows a test of the predictive capability of the models.

5.4.2.1 Modeling Damage from VUV Photons

The interaction of VUV photons with the p-ULK film occurs through photolysis of various chemical bonds in the material. For this material, VUV photons primarily interact with Si-C and Si-O bonds. As stated earlier, photons scission Si-CH$_x$ bonds, and an irreversible reaction occurs when oxygen in the background reacts with the methyl (-CH$_x$) groups.[66] Since varying O$_2$ background pressure was shown to have negligible effects, the photo-generated reaction sites are thought to be saturated and need not be explicitly included in the model. Furthermore, Si-O concentration did not change dramatically following exposure, so this parameter was held constant as well. Photons are absorbed by Si-C bonds, and there is a chance that these bonds will remain broken if O$_2$ is nearby to form a stable reaction product, removing the carbon groups from Si. This breaking probability (per photon) is denoted by the effective photolysis cross section, σ_{SiC}. Since the attenuation coefficients of Si-C bonds and Si-O bonds are known to be significantly different for photons in the VUV region,[72] the spatial profile of photon flux through the film, *I(x),* will also change as a function of time. This transient photon flux will then result in changes in the Si-C bond profile in time and depth.

$$n_{SiC} = c_{SiC}/c_{SiC,0} \tag{5.1}$$

$$\alpha_t(x,t) = \alpha_{SiC}n_{SiC}(x,t) + \alpha_{SiO}n_{SiO} + \alpha_p n_p \tag{5.2}$$

$$\frac{dI}{dx} = -\alpha_t(x,t)I(x,t) \tag{5.3}$$

$$\frac{dn_{SiC}}{dt} = -I(x,t)\sigma_{SiC}n_{SiC}(x,t) \tag{5.4}$$

This 1-D model assumes that the total attenuation coefficient (α_t (*x*, *t*), cm^{-1}) is the sum of the attenuation coefficients from each of the two types of bonds weighted by the fractional bond densities ($\alpha_{SiC} \times n_{SiC}$ and $\alpha_{SiO} \times n_{SiO}$) plus a component associated with the pores ($\alpha_p \times n_p$) which is set to zero. The divergence of the photon flux then is set equal to the product of the total attenuation coefficient and the photon flux. The final equation equates the time rate of change of fractional SiC bonds to the loss of these bonds by photolysis. By using fractional concentrations, the percentage of carbon loss from FTIR can be compared to experimental results. Similar

equations were previously used to predict the effects of VUV emissions from Ar plasma and photons from a VUV lamp in a high vacuum chamber.[81]

The initial relative concentration of each component, n_i, was estimated to be 0.175 for Si-C, 0.525 for Si-O and 0.30 for porosity. For 130 nm wavelength emissions from O_2 plasma, the respective attenuation coefficients are 3.7×10^{-2} cm^{-1} for Si-C and 2.9×10^{-3} cm^{-1} for Si-O,[72] while porosity was treated as empty volume with zero attenuation. Given that the VUV flux impacting the surface of the film was measured to be 4.6×10^{14} photons/cm^2·s for a 10 mTorr, 150W O_2 plasma, the photolysis cross section, the only unknown parameter, was adjusted in the model until the carbon removal was matched to that observed experimentally (fig. 5.7). By fitting this model parameter to experimental data, an effective photolysis cross section of 1.4×10^{-17} cm^2 was obtained. This value corresponds to a photodissociation quantum yield of ~15% since the total cross section is known to be 9.3×10^{-17} cm^2.
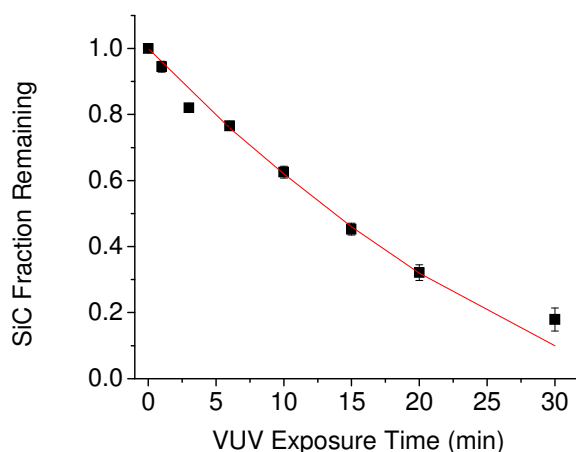
Figure 5.7 Comparison of carbon loss from experimental results and the VUV model as a function of exposure time. The photolysis cross section can be obtained through fitting with experimental results.

Using these parameters, figure 5.8a shows how the VUV flux changes as a function of time and position in the film. Near the beginning of the exposure, the VUV flux drops rapidly near the surface of the film due to relatively strong absorption by Si-C bonds. Only a small fraction of photons are able to penetrate deeper than 50 nm. As exposure time increases, carbon is lost, predominately near the surface. With fewer Si-C bonds in the relatively transparent SiO$_x$ modified layer, VUV photons penetrate deeper in the film due to an effectively lower attenuation coefficient. After 30 minutes of exposure, the VUV photons are able to pass through the entire film (230 nm), retaining roughly one-quarter of the flux at the surface. At this point, almost all of the carbon has been removed from the film. The predicted carbon depth profile (fig. 5.8b) was noted to be consistent with the experimental results shown earlier in figure 5.4: a gradual spatial profile of carbon loss as predicted in fig. 5.8b would yield the relatively large decrease in integrated carbon post HF dip, as shown in fig. 5.4. This assertion depends on the exact location of the boundary between the modified layer and the pristine material (i.e. where the removal of material by HF stripping ends). The reduction of the FTIR Si-C peak before and after the HF

strip (fig. 5.4) can thus be compared to the area underneath the carbon concentration curves in figure 5.8b. Furthermore, a rough estimation of the modified layer thickness can be obtained from the Si-O peak remaining after the HF strip, using FTIR. Using these two techniques, the dilute HF solution was observed to strip the damaged low-*k* material when the carbon percentage drops below ~85% of its pristine value. After the HF strip, the remaining film is mostly undamaged. Therefore, analyses typically used to characterize damage using total carbon removal (i.e. integrated through the film) can underestimate the true extent of damage. Bulk characterization techniques generally fail to capture the spatial distribution of the carbon loss throughout the film. As a result, the total carbon loss may not directly correlate to the thickness of the damage layer, and ultimately the dielectric change, when a spatial profile of residual carbon exists.
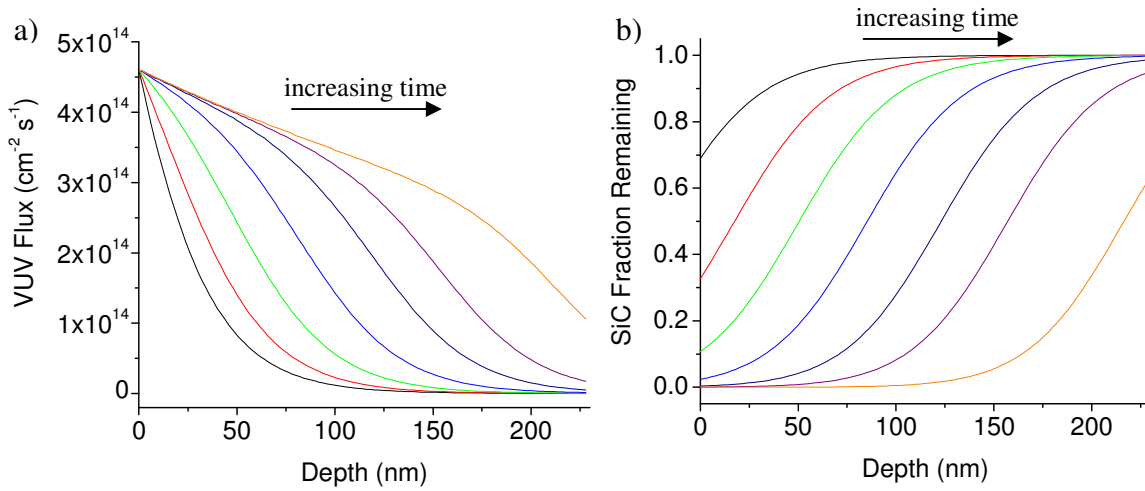
Figure 5.8 VUV model predictions of (a) VUV flux and (b) carbon concentration as a function of depth and time. The VUV photons travel deep into the film due to a lower film attenuation coefficient at longer exposure times.

Summarizing, the model appears to reproduce the observed damage layer profile evolution in time and matches, at least qualitatively, the relatively gradual spatial profile of Si-C bonds following VUV only exposure. The model used only a single fitted parameter (Si-C photolysis cross section) and this parameter is consistent with literature values.

5.4.2.2 Modeling Damage from Oxygen Radicals

The surface of the film is assumed to be exposed to a given oxygen radical concentration, $c_{o*,0}$, and the film contains a starting concentration of carbon compounds, $c_{SiC,0}$. Oxygen radicals diffuse through the film with an effective diffusion coefficient, D. The reaction rate between oxygen radicals and carbon compounds is dictated by a reaction rate coefficient, k. O atom

recombination to form O_2 and reaction products generated in the film were ignored in this model. With this depiction, a 1-D reaction-diffusion model can be written as follows:

$$\frac{\partial c_{o*}}{\partial t} + \nabla\left(-D\frac{\partial c_{o*}}{\partial x}\right) = -kc_{o*}n_{SiC} \tag{5.5}$$

$$\frac{dc_{SiC}}{dt} = -kc_{o*}c_{SiC} \tag{5.6}$$

where diffusion of oxygen radicals and subsequent reaction with carbon compounds is expressed by equations 5.5 and 5.6. However, carbon removal as a function of time as dictated by these equations alone does not yield the experimentally observed trend. Given these model equations, only the diffusion and the reaction coefficients need to be changed to obtain an appropriate fit with the experimental data. These two parameters can be related through the Damkohler number, defined below for this case.

$$Da = \frac{kL^2}{D} \tag{5.7}$$

This dimensionless parameter defines the ratio of the reaction rate versus the transport rate, or the k versus D, through a characteristic length, L. In this case, the characteristic length is the film thickness. By varying the ratio of k/D, no single value was able to fit the experimental data accurately. As shown in figure 5.9, the model results only fit for shorter or longer time periods, but not the entire time frame. The possibility of a non-constant radical flux at the surface of the film was explored next in the model. With the addition of this parameter, the model predictions were able to fit quite accurately with experimental results. As a result, several factors were investigated that could cause a change in radical flux over time. First, obstruction of radical diffusion into the Teflon cap was examined. However, calculations show that with a 1.5 mm aperture, the concentration within the cap equilibrates almost instantaneously. Furthermore, reported recombination rates on Teflon do not show significant loss of oxygen radicals to the cap surface.[89] As a result, the design of the sample holder is not expected to significantly hinder diffusion. Next, the possibility of a thin, less diffusive layer on top of the film was examined. Given that these materials are stored under atmospheric conditions, it is possible that a layer of adventitious carbon or densified oxide is present on the surface of the film. In such a scenario, this overlayer would limit permeability of oxygen radicals into the film initially, such that the concentration within the film would slowly equilibrate with the environment.
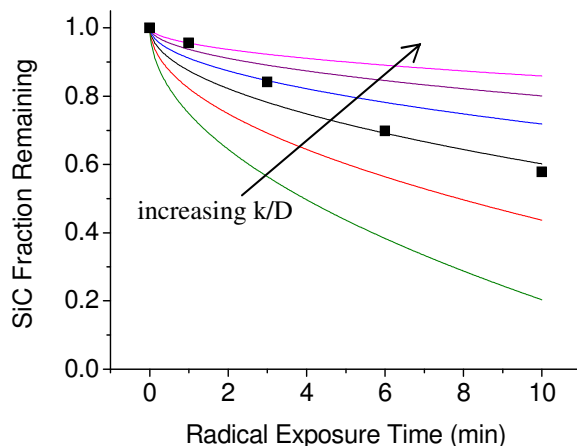
Figure 5.9 Model predictions of the carbon loss under varying values for *k/D*. Comparison with experimental data shows that good fits cannot be obtained by simply changing this parameter.

To examine this hypothesis in the model, a thin, less diffusive overlayer (~ 5 nm) was assumed to be present at the surface of the film. By adding a less diffusive overlayer, the effective radical flux through the overlayer and into the surface of the low-*k* film would gradually increase as a function of exposure time. The resulting radical flux and carbon concentration profiles for the 10 mTorr plasma condition can be seen in figure 5.10. As observed in figure 5.10a, the radical concentration at the surface of the film would slowly increase with longer exposure time. By hindering the flux in this manner, the total carbon removal shows reasonable agreement with experimental findings. Although an overlayer thickness of 5 nm was arbitrarily chosen for the model, the respective diffusivity needed to match the experimental data changed proportionally with thickness. As a result, the permeability value (ratio of diffusivity to thickness) of oxygen radicals into this overlayer is reported, which remains constant for a given treatment. For all radical exposures shown here, the best fit permeability was observed to be a value of ~20 cm/s.

Figure 5.11 shows a comparison of the carbon removal from the model and experimental data for plasma pressures of 1.5, 10, and 30 mTorr. The respective O radical concentrations inferred from the fits to the data, $c_{o*,0}$, used in the model were 1.3, 7.0, and 16×10^{12} cm^{-3}. While the radical concentrations were not directly measured in this study, the values inferred from fitting experimental data are in reasonable agreement with values reported in an earlier study using the same ICP system.[86] With a reaction constant of $k = 2.0 \times 10^{-13}$ cm^3/s and film diffusivity of $D = 1 \times 10^{-4}$ cm^2/s, good agreement with the experimental data can be obtained. The diffusivity used here is noted to be similar to that measured for toluene diffusing through a similar low-*k* film containing 30% porosity.[83] While no estimates for reaction rate constants have been reported so far, the value for *k* can be adjusted to achieve the near-carbon free profiles observed from experimental results. Despite the simple equations and rough estimates of parameters used in this model, the effect of radical treatment on the low-*k* film appears to be captured reasonably well.
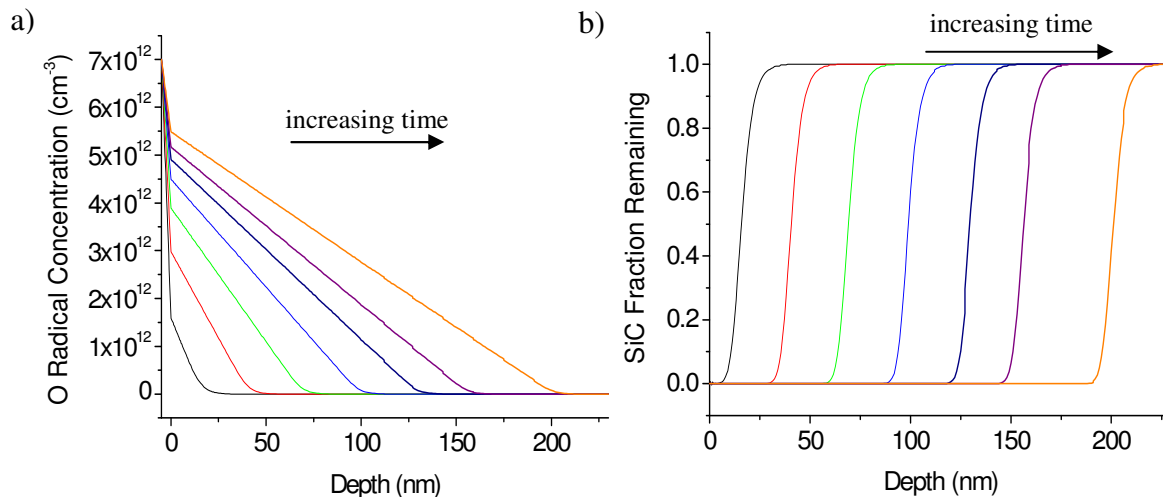
Figure 5.10 Radical model predictions of (a) radical concentration and (b) carbon concentration as a function of depth and time. A thin overlayer hinders diffusion of radicals into the film. The modified layer can be easily identified by steep drops in the carbon concentration.
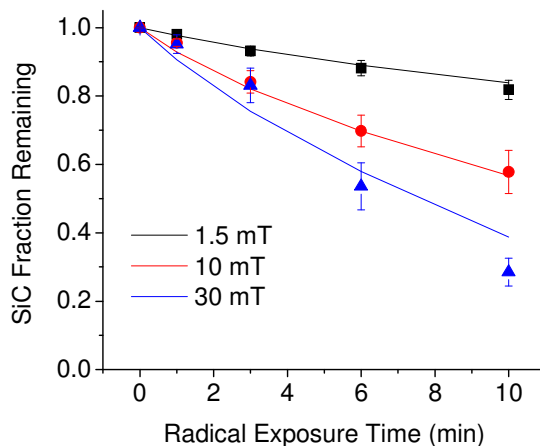
Figure 5.11 Comparison of carbon loss from experimental results and the radical model as a function of exposure time. Radical model parameters were refined through fitting with experimental data at operating pressures of 1.5, 10, and 30 mTorr.

5.4.3   Radical and Photon Effects During Plasma Treatment

While VUV photon and oxygen radical effects can be isolated for individual study, these effects must ultimately be studied for O_2 plasma, where they occur simultaneously. One has to take care to ensure that radical and photon fluences are similar to the emissions from plasma, especially since the sample holders intrinsically decrease the flux of the species compared to samples undergoing direct plasma treatment. During these plasma studies, differences in radical and photon-induced damage were encountered that were not observed when each species acted alone.

60

5.4.2.1 Growth of the Modified Layer

Differences in carbon extraction from the film versus depth demonstrate the importance of VUV through HF stripping (fig. 5.12). For the 10 mTorr case, the profile caused by VUV photons alone was observed to be similar to direct plasma exposure. While the damage layer growth rate for direct plasma exposure was faster, this could be explained by lower effective photon and radical fluxes caused by the design of the sample holder. Although the total carbon loss was noted to be similar for photons and radicals alone (from fig. 5.4 and 5.5) at 10 mTorr, the growth of the modified layer was different because VUV photons penetrated deeper into the film, while radicals caused layer-by-layer carbon removal. Conclusively, the modified layer during plasma exposure appears to be photon-controlled, signifying that VUV induced damage is most significant.
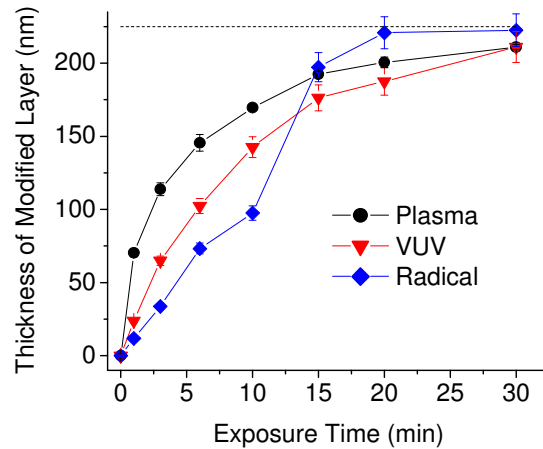
Figure 5.12 Comparison of the thickness of the modified layer for direct plasma, VUV, and radical exposures as a function of time. The film thickness is 230 nm, indicated by the dotted line.

5.4.2.2 Plasma Damage to Low-k

While radicals and photons are believed to be the main contributors of plasma-induced damage, the behavior of carbon loss appears to differ during direct plasma exposure versus radical or photon alone. The actual carbon loss during a direct O_2 plasma exposure did not correspond to the addition of effects from VUV and radicals individually. In figure 5.13a, the carbon removal from O_2 plasma is shown for 3 pressure conditions: 1.5, 10, and 30 mTorr. The low-k samples were treated for periods of up to 30 minutes. Model predictions for the combined VUV and radical effects, based on fits from the individual treatment cases described above, are included in this figure. In these model predictions, the VUV and radical models were combined, and fluxes representative of the plasma exposure were used. However, they appear to grossly overestimate the amount of carbon removal, especially at longer exposures. This shows that the presence of both species is less than the damage that might be expected from the sum of photons and radicals alone. Interestingly, large differences were observed in the carbon removal rate by radicals alone at these pressures, yet only small differences were observed between plasma

treatments. Damage from radical effects alone considerably exceeds carbon loss compared to direct plasma treatment at similar times. Horizontal-dotted lines on figure 5.13b denote the carbon loss by O_2 plasma after 30 minutes, showing that radical exposures after 15 minutes for 10 mTorr and 30 mTorr clearly surpass that of its counterpart. This result is surprising, especially since the radical flux from direct plasma exposure should be higher, not to mention that damage from VUV photons would be present as well. This behavior suggests that a mechanism exists to reduce radical-generated carbon loss during direct plasma exposures.
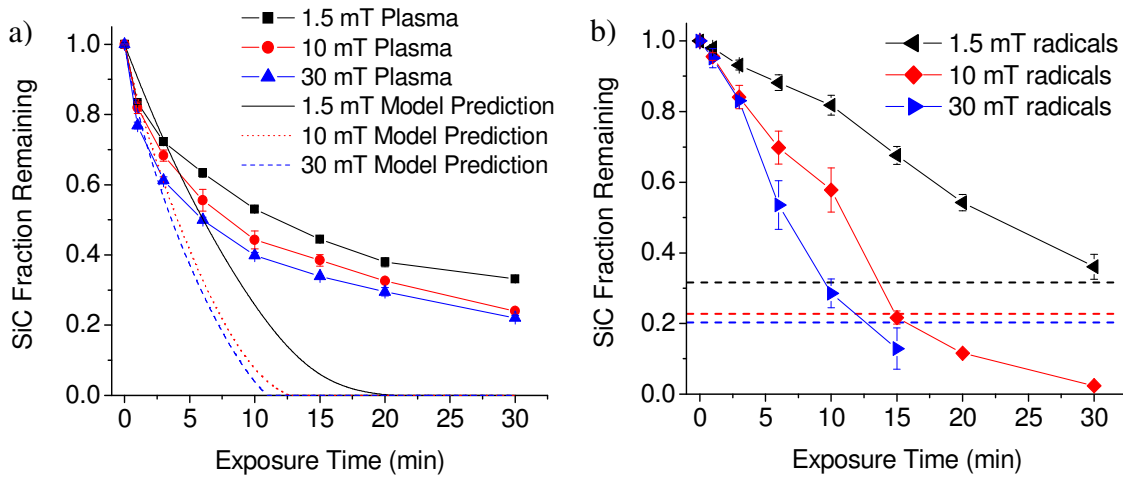
Figure 5.13 Comparison of carbon loss for (a) plasma exposures and (b) radical exposures as a function of time. Pressure conditions of 1.5, 10, and 30 mTorr and power of 150 W were used in each case. Model predictions show a rate of carbon removal that is greatly overestimated compared to experimental results. Horizontal dotted lines show that carbon loss from radicals alone can exceed that of equivalent plasma treatment for longer exposures.

5.4.2.3 Plasma Inhibition of Radical and Photon Effects

By performing short exposures of direct O_2 plasma on the low-k films before subsequent photon-only or radical-only exposure, it becomes clear that subsequent carbon loss is inhibited. Figure 5.14 shows the carbon removal from samples that are first subjected to O_2 plasma for 10 seconds or 30 seconds, followed by exposure to VUV photons or oxygen radicals for up to 10 minutes. A large drop in carbon occurs initially due to direct plasma exposure, but the subsequent exposures to photons and radicals demonstrate very different results when compared to a non-plasma pre-treated sample. The short plasma pre-treatments seem to have little impact on subsequent damage by VUV photons alone, as evidenced by similar carbon removal rates compared to the control. However, subsequent radical damage appears to have almost completely stopped for most cases. For both 10 second and 30 second plasma pre-treatments, oxygen radicals appear to have little further effect on the film. Only after 10 minutes of subsequent radical exposure did a large drop of carbon occur for after the 10 second plasma pre-treatment. These results indicate that very short plasma exposures can greatly reduce subsequent

carbon loss by radicals. Such behavior appears to explain the differences between the plasma and radical-only damage profiles. Both photon and radical damage occurs simultaneously at the start of the exposure, but then radical damage is hindered as the exposure continues. These findings indicate that plasma damage is likely controlled by VUV photons at later times.
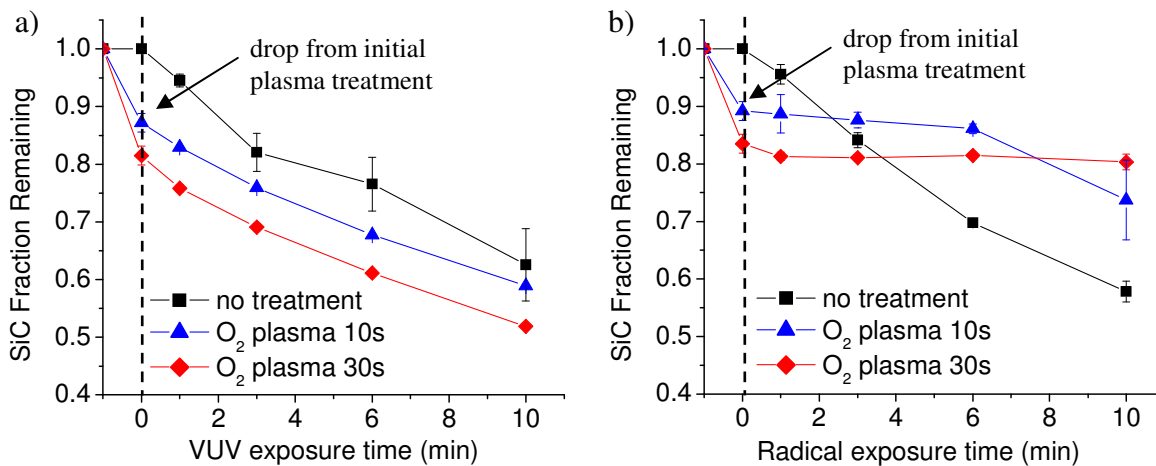
Figure 5.14 Comparison of carbon loss for (a) VUV exposures and (b) radical exposures as a function of time. Samples were pre-treated with O_2 plasma for 10 seconds or 30 seconds, with non-plasma treated samples shown for comparison.
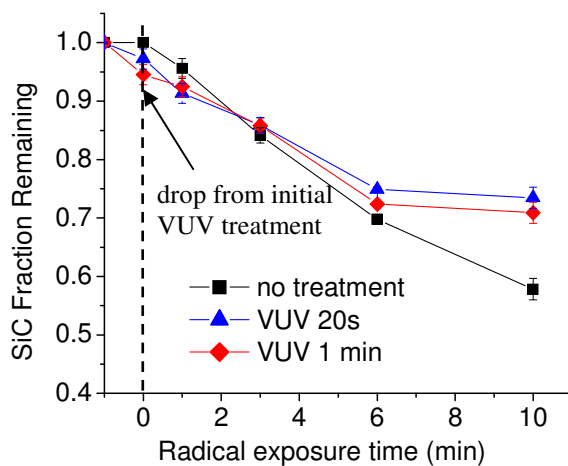
Figure 5.15 Comparison of carbon loss for radical exposures after pretreatment to VUV photons for 20 seconds or 1 minute. Non-VUV treated samples are shown for comparison.

The inhibition of radical damage after a short VUV-only treatment was examined as well. Figure 5.15 shows pre-treatment of low-k samples for 20 seconds and 1 minute of VUV radiation, followed by oxygen radical exposure for up to 10 minutes. The exposure time for VUV irradiation was doubled to match the actual photon fluence of direct plasma, due to window absorption. In this case, the rate of carbon loss does appear to be slower compared to non-VUV pre-treated samples. However, the effect is much less than that of the direct plasma treatment. It is possible that the combined effect of various species in the plasma synergistically acts to prevent further radical damage. Interactions such as these make it difficult to understand the behavior of plasma, even when the individual species can be isolated and characterized.

While plasma exposures appear to inhibit radical damage, the mechanism is not well understood. Various mechanisms of radical inhibition have been proposed. Studies involving plasma treatments using other gas chemistries, like He, H_2, N_2 and NH_3, have been proposed to block subsequent O_2 plasma damage through pore sealing.[21,90-92] These techniques range from forming a thin, densified layer near the surface to depositing an overlayer that fills pores, with the ultimate goal of hindering diffusion of plasma species into the film. Molecular dynamics simulations have shown that oxygen radical damage can differ significantly due to changes in the organosilicate network structures.[93,94] Since VUV photons from O_2 plasma have enough energy to not only break Si-C bonds, but Si-O bonds as well, these photons may be forming reaction sites that allow oxygen radicals to be incorporated into the material network. Through restructuring of this network, the pores may shrink, leading to a densification of the film. These changes to the material typically lead to a decrease in the effective diffusivity, lowering the rate at which oxygen radicals can penetrate into the film and remove carbon species. After the short plasma treatments (10 or 30 seconds), the carbon-depleted layer can be observed to be ~10-20 nm thick. Utilizing the the radical reaction-diffusion model described above, it was observed that the effective diffusivity would have to decrease by at least an order of magnitude in the modified region to achieve the drastic reduction of the carbon removal as seen in figure 5.14b. As a result, the oxygen radical permeability (the ratio of diffusivity and thickness) in the plasma-exposed carbon-depleted layer shows similar values as the proposed near-surface reduced diffusivity region that was needed to explain the radical-only data. The formation of a much thicker reduced diffusivity region appears to be the most reasonable explanation to account for the observed plasma-induced damage behavior. In addition, such a large decrease in the diffusivity may even impact the photon-induced damage, by limiting molecular O_2 diffusion as well. While the carbon loss by VUV photons was shown earlier to not depend on the operating background pressure, this may not be the case after a large drop in the diffusivity, which could hinder the replenishing of oxygen to the photo-generated reaction sites. As a result, carbon loss from VUV photons may be overestimated by the models, since the current VUV damage model does not account for diffusion of O_2 or reaction products. Further techniques would be necessary to analyze how the diffusivity of the modified regions in the film changes with plasma treatment in order to obtain accurate predictions of the carbon loss in a combined exposure.

5.5   Conclusions

The effect of individual plasma species on porous low-k damage, such as VUV photons and radicals, has been studied for O_2 plasma. By using specifically designed sample holders, the carbon removal by photons and radicals can be isolated and individually examined. By examining the depth profile using FTIR and HF stripping, VUV photons were observed to gradually remove carbon compounds throughout the penetration depth, creating a modified layer that still contains a considerable amount of carbon. In contrast, oxygen radicals remove carbon compounds layer-by-layer, creating a nearly-carbon free modified layer. As exposure time increases, the modified layer grows deeper, mainly due to changes in the film attenuation coefficient for photon exposures and diffusion rate of reactive species for radical exposures. Models were created to predict the VUV and radical damage for varying conditions, fitting them to experimental data to account for unknown parameters. Model predictions of VUV effects (fitting the photolysis cross section) show good agreement with experimental results. On the other hand, radical effects can only be modeled accurately by including in the model a less diffusive overlayer that inhibits the radical flux at the surface of the film. However, these models cannot be combined to predict behavior under simultaneous exposures. Adding the effects of individual photon and radical exposures leads to a large overestimation of carbon removal. Brief, direct O_2 plasma exposures were observed to greatly hinder subsequent radical damage, but not VUV damage. The mechanism responsible for this behavior is not well understood, but simultaneous VUV and O radical exposure is postulated to cause a reduction in pore diffusivity in addition to loss of carbon, in analogy with what was found in the near-surface overlayer. A model calculation that assumes the same reduced radical diffusivity in the damaged region exposed to simultaneous VUV and O radicals yields results in reasonable agreement with observations. One important implication is that plasma-induced modifications of pore diffusivity are possible and this might be exploited in future technologies to minimize damage during subsequent processing.

Chapter 6
Treatment Methods to Reduce Plasma-Induced Damage on Low-k Materials

6.1 Abstract

As demonstrated in Chapters 3-5, plasma species, such as VUV photons and radicals, impact low-k materials in negative ways. Fundamental understanding of the factors that influence these effects can lead to beneficial techniques to reduce plasma-induced damage. Consequently, various methods have focused on blocking out selected plasma species from entering the material, both through the design of the material and through fine tuning of treatment methods. This chapter focuses on the examination of some of these methods and presents topics for consideration in the future. Methods to reduce the diffusion of plasma species into the film will be highlighted in detail.

6.2 Introduction

The increase in the dielectric constant of porous low-k materials due to exposure to plasma is a significant problem in advanced microelectronics processing. The lower dielectric constant of low-k relative to SiO_2 stems from enhanced porosity and the incorporation of methyl (-CH_3) groups, which make the material susceptible to various reactive species originating from plasma exposures.[7,26] Among various types of plasma exposures, oxygen plasma is seen to be most damaging. Oxygen radicals created from the plasma cause removal of methyl groups within the film, turning the film hydrophilic and allowing a significant amount of water to absorb into the film.[12,29,65] Similar effects can occur due to the diffusion of molecular oxygen species into the bulk in the presence of vacuum ultra-violet (VUV) radiation.[66] Under long plasma exposures, Si-C bond scissioning is induced by the diffusion of radicals and molecular oxygen species in the bulk of the low-k film, in conjunction with vacuum ultraviolet (VUV) radiation, creating even more sites for water absorption and ultimately resulting in significant increase in the dielectric constant.[84]

Plasma etching often uses fluorocarbon-containing plasmas.[77,78] However, the residual CF_x polymer that remains behind can pose issues for subsequent processing steps, like reaction with diffusion barrier metals, and must be removed. Ashing steps using oxygen-containing plasmas have been used in the past for post-etch cleaning, as well as photoresist removal.[76] Therefore, a number of pretreatments have been used to limit low-k damage during CF_x removal. These include He plasma pretreatments that appear to densify the surface and inhibit subsequent diffusion of O radicals or O_2 into the bulk of the film.[93,95] Reducing plasmas containing H_2 and N_2 have been of great interest because radicals generated in these cases appear to induce significantly less carbon removal compared to oxygen containing plasmas.[20-22,79,96]

As stated in the previous chapter, the role of film diffusivity appears to be an important factor. By decreasing the film diffusivity, the plasma species are potentially blocked from entering the film, reducing carbon extraction and preserving the dielectric properties in the bulk of the film. The first section will briefly examine how material choice, with different diffusivities, will affect plasma-induced damage. The following sections examine techniques to densify the near-surface region of the film, effectively creating a diffusive barrier. These techniques include Ar/He ion bombardment and NH_3 plasma treatments. In the process, the effects of individual plasma species can be inferred, leading to specific methods to improve the treatments.

6.3   Experimental Setup

In these studies, p-ULK (k = 2.54) and d-ULK (k = 2.54) films, both obtained from Novellus Inc., were examined. These two materials have similar chemical compositions and undergo similar behavior under plasma treatment, as shown by the FTIR spectra in figure 6.1. However, these films have different pore structures, which affect the diffusivity and thus the rate of plasma-induced damage. Due to smaller pore sizes and lower pore connectivity, the effective diffusivity of d-ULK was reported to be 6 times smaller than p-ULK.[29] Films of p-ULK used in these experiments varied from 220-300 nm thick, while the d-ULK films were 500 nm thick. Studies involving VUV-induced carbon removal were performed in the beam system, which is equipped with a Xe VUV source (Resonance Ltd.) giving off 147 nm radiation. The photon flux at the sample for all experiments was 1.3×10^{14} photons/(cm^2 s). During exposure to VUV radiation, a background oxygen pressure of 1×10^{-4} Torr is present. Molecular oxygen diffused into the pores reacts with scissioned carbon species, forming volatile leaving groups.

Plasma studies with various chemistries (Ar, O_2, He, NH_3) were performed in the inductively-coupled plasma (ICP) system. Measurements of plasma parameters under different conditions are listed in Appendix B. The chamber contains a Faraday shield between the coil and dielectric plate to prevent capacitive coupling. During these plasma exposures, the energy of the plasma-generated ions was estimated to be in the range of 15-25 eV. However, these ions can be accelerated towards the sample using an independently-biased substrate electrode positioned on the copper sample holder. Consequently, the energy of ions impacting samples can be manipulated to several hundred eV with minimal changes to plasma density and ion flux to the surface of the film. Further details are given in Chapter 2. In this manner, the effects of other plasma species can be partially distinguished from those of high energy ions. Further

description of the treatment parameters will be given in the next section for each respective treatment.
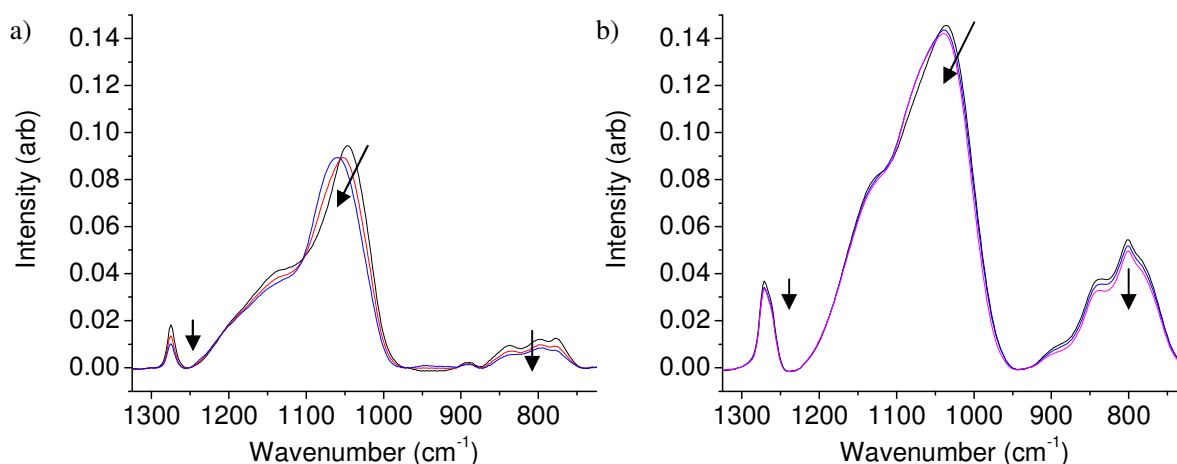
Figure 6.1 FTIR spectra of the (a) p-ULK and (b) d-ULK films show similar chemical composition. The absorbance values for d-ULK are higher mainly due to a thicker film. Plasma exposure of these films affects the chemical structure in a similar manner, as indicated by the peak drops.

The bulk chemical effects on the samples were examined using *ex-situ* transmission Fourier-transform infrared (FTIR) spectroscopy (Digilab FTS-3000). The integrated FTIR peak was used for the comparison of results, primarily looking at changes in the Si-C bending peak (1270 cm^{-1}) to compare the levels of damage.

6.4   Results and Discussion

6.4.1   Comparison of Plasma Effects on p-ULK and d-ULK

From studies performed in Chapter 3, it was found that VUV radiation had a significant effect on p-ULK materials. Furthermore, the mechanism for carbon extraction from the film depended on the presence of gas species, such as O_2, to generate volatile products after photo-scission of the Si-C bond. Consequently, materials with lower diffusive properties restrict the flow of oxygen into the porous material, possibly preventing this carbon removal. VUV treatment of d-ULK samples were first performed in the beam system using a calibrated Xe lamp. During the exposure, a background O_2 pressure of 10^{-4} Torr was maintained. After the exposure, FTIR spectra were obtained to examine the relative drop in the Si-C bending peak for various VUV fluences. These results were compared to previously obtained FTIR spectra on VUV/O_2 treatment of p-ULK, as shown in figure 6.2. While the p-ULK material loses up to 70% of the original carbon content within this fluence range, less than 10% is lost for the d-ULK material under an equivalent exposure. Even when accounting for a higher starting amount of carbon due to film thickness differences, the d-ULK material clearly shows high resistance to VUV/O_2

exposure. This resistance is likely to be due to the lack of oxygen diffusion into the film, as photon transparency for 147 nm radiation is fairly high.[81] As a result, photo-scissioning of the Si-C bonds is still believed to occur, but carbon removal is prevented because the resulting CH_3 radical is relatively involatile and/or immobile. With the presence of O_2, these CH_3 radicals would react to form CO_2 and H_2O, which are volatile.[60] With a lack of oxygen present, reattachment of the CH_3 radical onto the Si reaction site would then occur. In contrast, previous studies showed that oxygen diffusion into p-ULK was not limited, provided that the background pressure was at least 10^{-5} Torr.[66]
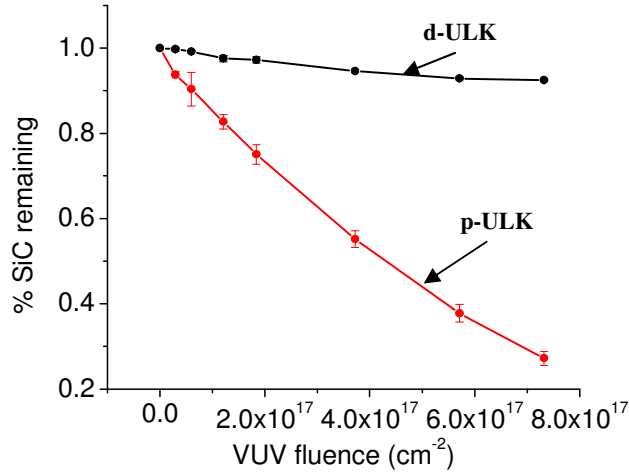
Figure 6.2 Integrated carbon peaks from FTIR for p-ULK and d-ULK after VUV/O_2 exposure in the beam system for a range of VUV fluences.

Under plasma treatment in the ICP system, similar behavior was observed for the d-ULK material. Figure 6.3 shows the resulting carbon losses for Ar plasma and 75% Ar/ 25% O_2 plasma on the p-ULK and d-ULK materials. The plasma conditions used in these exposures were 10 mTorr and 70 W. Carbon loss from VUV/O_2 exposure is also plotted for comparison. In Chapter 4, the primary factor for carbon removal from p-ULK was determined to be due to differences in the wavelength, and therefore penetration ability into the film. In contrast, the rate of carbon removal for d-ULK appears to be roughly similar in all cases, signifying that another mechanism, diffusion, is limiting the rate of damage. Slightly higher carbon removal may occur under plasma treatments due to a larger concentration of oxidizing species, such as residual water vapor. Furthermore, oxygen radicals generated from the Ar/O_2 plasma also contribute to the carbon removal. From these observations, a lower diffusivity is thus strongly linked to prevention of plasma-induced damage. However, resistance to plasma-induced damage alone does not make a functional low-k material. Methods to continually decrease the dielectric constant of the material and integrate it into processing must be viable. For the d-ULK material, further increases in the porosity to decrease k would have the negative effect of increasing pore interconnectivity. As a result, other treatment methods must be investigated to mimic this plasma resistance.
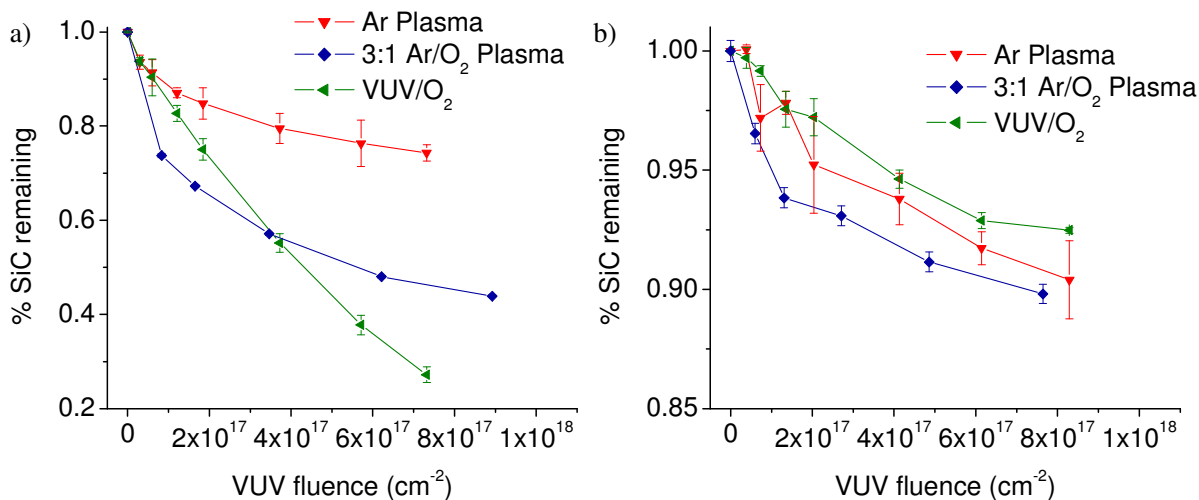
Figure 6.3 Integrated carbon peaks from FTIR for p-ULK and d-ULK after various exposures: Ar plasma, 75% Ar/ 25% O_2 plasma, and VUV/O_2. Plasma conditions of 10 mTorr and 70 W were used.

6.4.2   The Role of Ion Bombardment in Plasma Exposures

While diffusivity has been observed to play a large role in plasma resistance, formulation of materials that exhibit this resistance, while still remaining practical for plasma processing, is not a trivial process.[7]   However, application of this concept to the material as a whole is not necessary. Modification of a thin layer of the material may be enough to block out plasma species from entering the film via the pores. This section explores methods to densify the near-surface of the p-ULK material in an attempt to mimic the plasma resistance found from d-ULK. The affected depth of the material must be minimized to avoid impacting the dielectric constant. These treatments focus on plasma species that have low penetration ability, such as ions or low-λ photons. Noble gas plasmas, such as Ar and He, were used to look for instances of densification that would lead to damage prevention during a subsequent O_2 plasma exposure. By using a sample holder that can be biased independently, the effects of ions and photons can be separated, at least in part.

6.4.2.1 Effect of Neutral (Unbiased) Plasmas on O_2 Plasma Damage Protection

First, unbiased plasmas were examined for differences concerning effects of VUV radiation. He and Ar plasmas were explored because both emit high energy VUV photons (He: λ = 58.4 nm, Ar: λ = 104.8, 106.7 nm) that are estimated to have relatively low penetration depths (~ 10-20 nm) into p-ULK films. Since VUV photons are able to break Si-C bonds, it is beneficial to have photons with low penetration ability to limit carbon loss to the near-surface of the film. To obtain comparable results between Ar plasma and He plasma treatments, plasma conditions were used such that similar trends for carbon loss were observed with time. As a result, the

conditions for plasma power/pressure used were 70W/10 mTorr for Ar plasma and 100W/30mTorr for He plasma. Figure 6.4a shows the FTIR based carbon loss from the CH_3 bending peak (1270 cm^{-1}) as a function of treatment time for unbiased Ar and He plasma. The loss of carbon for Ar or He plasma exposures, as determined by FTIR, reaches ~20% of the total initial amount after 3 minutes of exposure. This corresponds to an affected depth of at least 50 nm into the film.[81] Photon penetration depth is not the only factor in determining carbon loss; the photon flux is also important. For the above-described plasma conditions, the photon flux is estimated to be in the range of 10^{15} photons/(cm$^2 \cdot$s). While the photon penetration depth, as defined by a 1/e reduction of the initial photon flux, is roughly 10 nm, the absolute flux remaining still appears to be high enough to cause carbon loss far below that point.

After the initial treatment in figure 6.4a, each of the pretreated samples was subjected to an additional O_2 plasma exposure (150W, 10 mT) for a period of 1 minute. This subsequent exposure led to additional carbon loss, dropping each of the carbon peaks further, as shown in figure 6.4b. The drop in carbon due to O_2 plasma is consistently around 15% of the total amount regardless of Ar plasma pretreatment time. In contrast, longer He pretreatment times cause a noticeable reduction of O_2 plasma-induced carbon loss, from 10% down to 5%. Furthermore, some He pretreated samples appear to show slight improvement over non-treated samples after the O_2 plasma exposure. As a result, He plasma appears to have an advantage over Ar plasma in this respect. Since the VUV photons emitted from He plasma (22 eV) are higher energy than from Ar plasma (12 eV), it is possible that the photons may play a larger part in breaking and restructuring the SiO_x network within the film during the He pretreatment.[93] Especially in regard to nanoporous materials with interconnectivity, slight restructuring of the material may change the diffusion of reactive species into the bulk, thereby affecting its resistance to plasma.[97] For these reasons, photons from He plasma have a significant potential for modifying low-k material and seem to offer some protection from O_2 plasma.
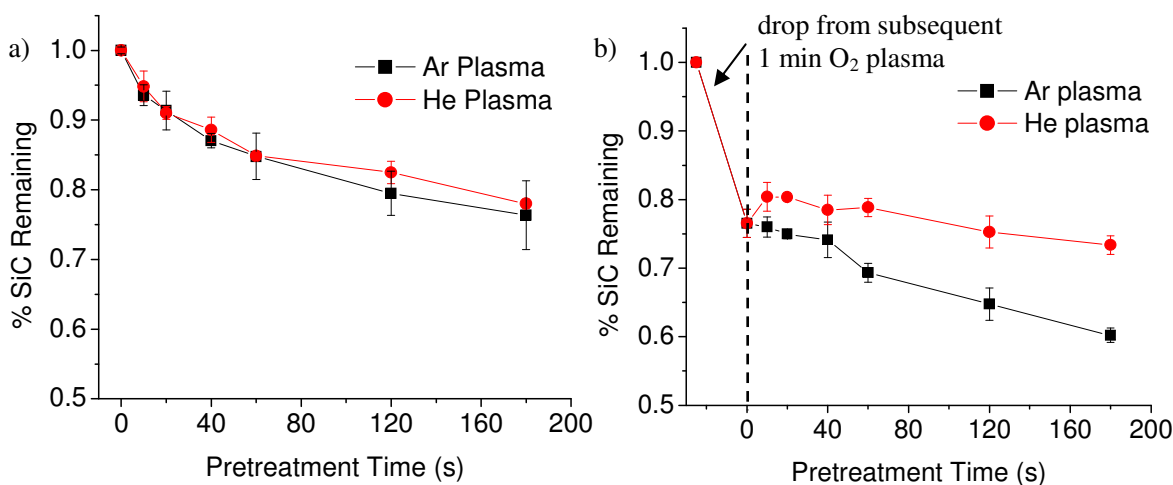
Figure 6.4 Carbon loss in p-ULK after (a) unbiased Ar and He plasma treatments, as indicated by the integrated Si-C peak obtained from FTIR. Plasma conditions were found such that the rate of carbon loss was equivalent for both exposures. Subsequent O_2 plasma exposures (b) were performed, removing more carbon from the films. However, some He pretreatments show improvement over the untreated samples after O_2 plasma.

While VUV photons are known to alter the film chemically, the unique outcome found from photons emitted from He plasma needs to be explored. Ultimately, He plasma treatments are only successful if the combined treatment and subsequent O_2 plasma exposure yield less damage compared to O_2 plasma alone. For this reason, examination of He plasma treatments and how they influence subsequent O_2 plasma exposure for a range of times was performed.
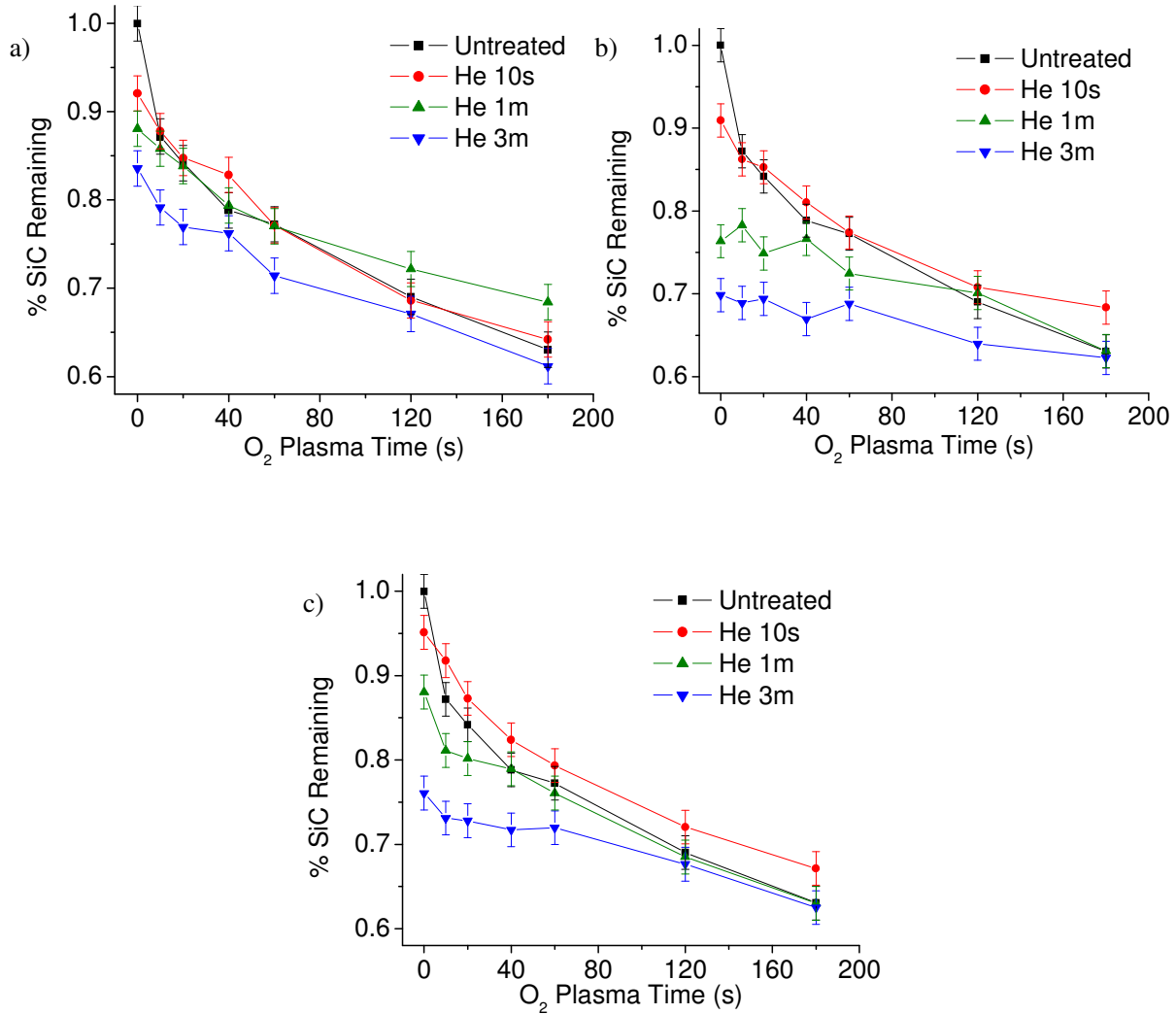
Figure 6.5 Carbon loss in p-ULK after unbiased He plasma treatments followed by O_2 plasma exposure. A range of processing conditions was examined for the He plasma treatments to minimize carbon loss: (a) 100 W/30 mTorr, (b) 200 W/30 mTorr, and (c) 100 W/50 mTorr. Results show that the unbiased He plasma treatments do not show significant improvement compared to untreated samples after O_2 plasma. In general, damage caused by VUV photons appears to outweigh any protection from O_2 plasma.

Figure 6.5a shows the effects of varying the treatment time (10 s, 1 min, 3 min) of an unbiased He plasma (100 W, 30 mTorr) on subsequent O_2 plasma-induced carbon loss. Similar to figure 6.4, He pretreatments are observed to cause more carbon loss with increasing time. Interestingly, little or no reduction of O_2 plasma-induced carbon loss is observed for all He pretreatments, when compared to untreated samples. For the 1 min He plasma treatment, slight improvement is only seen towards longer O_2 plasma exposures, where the rate of carbon loss appears to slow down. Yet, the longest pretreatment time of 3 minutes places all points below the control, signifying that the loss of carbon due to the VUV radiation during pretreatment is a bigger issue than any reduction of damage that could be obtained from hindering oxygen diffusion. Furthermore, the relatively low plasma power input in this case was used to minimize the photon flux. By increasing plasma power to 200W (Figure 6.5b), the photon flux also increases. As a result, the carbon loss due to He plasma pretreatment alone is more detrimental, making He plasma at higher powers worse. Changing the plasma pressure to 50 mTorr (Figure 6.5c) also seems to produce the same outcome, causing carbon loss without providing any protection. Overall, the data in figure 6.5 indicate that VUV photons alone are ineffective in reducing the total carbon loss for the range of O_2 plasma exposures under these conditions.

6.4.2.3 Effect of High Energy Ion Bombardment in He Plasma Treatment

Although VUV photons emitted from He plasma seem to be more damaging than beneficial, inclusion of high energy ion bombardment shows more promise. By using a separately-biased electrode on the sample holder, the He ions can be accelerated to the film surface up to a desired impacting energy. By doing this for He plasma treatments under the same conditions as shown in figure 6.5a (100W, 30 mT), the profile of carbon loss after subsequent O_2 plasma exposure appears remarkably different. The He plasma treatments in figure 6.6 involve ions that were accelerated from floating potential (~22eV) to 200 eV and 390 eV.

High energy ion bombardment appears to cause slight carbon loss during the He plasma pretreatment, in addition to that caused by VUV photons. However, the rate of carbon loss from subsequent O_2 plasma exposure appears to be significantly reduced, more so for longer He plasma pretreatments. As a result, the treatment appears to work quite well in preventing carbon loss depending on the length of O_2 plasma exposure needed. For short O_2 plasma exposures, it seems that short He plasma pretreatments are best. In fact, a He plasma pretreatment of 10 seconds with 200eV ions appeared to offer the best protection, preserving 90% of the total carbon content even after 40 seconds of O_2 plasma. This is likely because the carbon loss from the treatment is minimized while still maintaining protective properties. The results hint that possibly greater benefits could be obtained at even shorter He plasma treatments and/or lower ion energies, but it remains to be determined at what point the damage prevention begins. For longer O_2 plasma exposures, there is no clear advantage, possibly due to O_2 plasma etching through the protective layer. The preventative effect of He plasma treatment at 10 seconds seems to disappear after a certain amount of O_2 plasma, so longer treatments may be needed despite the negative effect of VUV radiation. Other than affecting initial carbon loss, the effect of varying ion energies is also not clear within this range. In general, higher energy ions during He plasma treatment appear to provide better O_2 plasma damage prevention, while the VUV radiation leads to more damage than any obtainable benefit. As a result, there is a need to optimize the He plasma treatment to reduce unnecessary damage by VUV radiation. Operation

of He plasma at higher pressures is one possibility, because radiation trapping is shown to occur for Ar plasmas at higher pressures.[10]
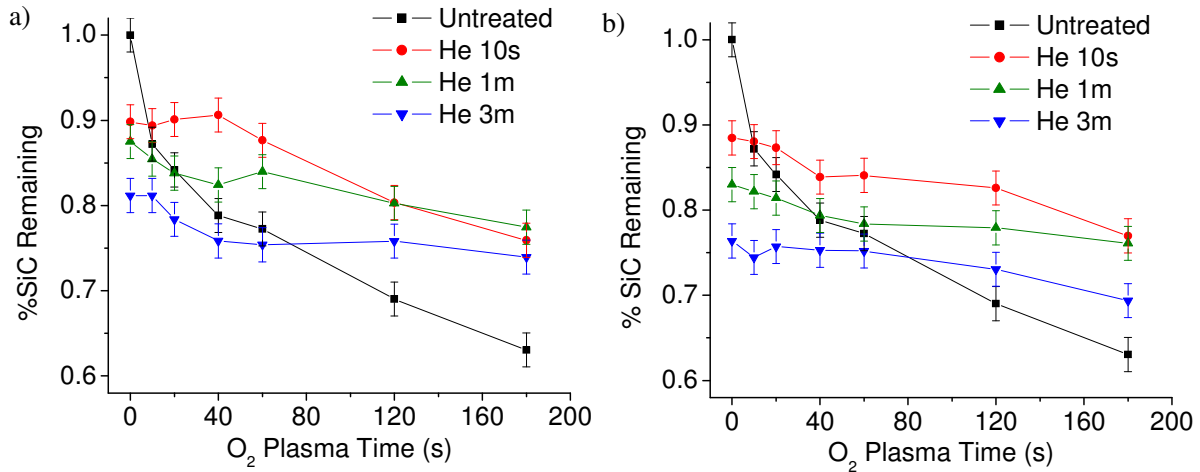
Figure 6.6 Carbon loss in p-ULK after biased He plasma treatments followed by O_2 plasma exposure. He plasma conditions of 100 W/30 mTorr were used. He ions were accelerated to energies of (a) 200 eV and (b) 390 eV. Results show that protection from O_2 plasma can be obtained and that high energy ions are responsible for this behavior.

6.4.2.4 Analysis of the Protection Mechanism for Ion Bombardment

While the emission of VUV photons can be reduced somewhat through tuning of plasma conditions, elimination of these damaging species can be obtained through the use of an independent ion source. By using an ion gun, protection of the p-ULK film by high energy ion bombardment can be obtained, without significant carbon removal by photon exposure. In particular, this method allows for the testing of different ion species without needing to worry about other residual emissions. Ions with much larger mass, like Ar^+ ions, are likely to behave differently. However, it has been reported that ion species in other plasma chemistries also lead to damage prevention.[13,82,98]

Since ions usually do not travel very far into low-*k* films, there are limitations to bulk characterization techniques, such as FTIR, due to sensitivity to variation. As a result, surface techniques to detect changes in chemistry such as X-ray photoelectron spectroscopy (XPS) would be needed to detect carbon removal near the surface of the film. In general, surface characterization techniques are becoming increasingly more important as the dimensions of semiconductor components continue to shrink. For this reason, further analysis of ion bombardment and surface characterization has been performed in collaboration with Prof. Jeff Kelber and graduate student Haseeb Kazi at University of North Texas.[99] This study involves the treatment of p-ULK to high energy ions from an ion gun, followed by O_2 plasma exposure. Ion bombardment has been observed to form a thin, densified oxide layer with a thickness of 1-10 nm that hinders plasma damage. More surprisingly, a significant amount of carbon near the

film surface is still present even after extended O_2 plasma exposure. These measurements were performed through XPS, where the sampling depth is at most 5 nm. In contrast, the carbon peak was reported to disappear almost immediately for samples with no ion treatment beforehand. The presence of carbon near the surface after O_2 plasma exposure suggests that densification of the material is not the only protection mechanism induced by ion bombardment. Transformation of terminating –CH_3 groups to linear –CH_2 chains has been shown in molecular dynamics simulations to greatly increase oxidation resistance.[94] A similar mechanism may be occurring with ion bombardment, but this effect remains to be investigated.

6.4.3   The Effect of a NH_3 Reducing Plasma

To reduce dielectric damage during ashing processes, oxygen-containing plasmas have been replaced with reducing plasma gas chemistries, such as N_2 and H_2.[100-101] Reducing plasmas are known to remove less carbon from low-k materials due to lower reactivity of the generated radical species, but thorough characterization of these damage effects has yet to be investigated. Characterization of plasmas containing gas mixtures can be fairly difficult due to the multitude of species that can be generated. Furthermore, ignition and stable emission of a pure N_2 plasma has been reported to be difficult.[102] For this reason, H_2 is normally added to supplement the process. In contrast, NH_3 plasmas have been found to be easier to ignite and stabilize, thus avoiding the need to control the gas proportions in the case of N_2/H_2 plasma. In this section, NH_3 plasma under various conditions was investigated to examine the generation of photons and radical species. These emissions were used to infer effects on p-ULK low-k materials.

6.4.3.1 Analysis of Photon/Radical Emissions Using Spectroscopy

For gas species such as NH_3, more dissociation and excitation paths are possible compared to monotomic and diatomic gases. As a result, the emissions of radicals and photons are more complicated, and thus their effects are more difficult to characterize. By examining the photon emissions in the VUV and optical ranges, the types and relative quantities of radical species can be inferred. Measurements obtained from the VUV spectrometer (Resonance Ltd.) in figure 6.7 shows that the VUV emission spectra are complicated, giving off a few strong emission lines along with a large amount of residual emissions. Characteristic emission lines at 122 nm and 124 nm indicating dissociated hydrogen and nitrogen, respectively, are observed. These emission lines have been reported to appear in plasma emissions containing either solely H_2 or N_2.[103-105] However, strong emission lines also appear in the range of 155-160 nm, which have not been characterized extensively in literature and do not appear when the plasma only contains H_2 or N_2. For this reason, it is believed that these VUV emissions may be due to NH_x species created by the NH_3 plasma, which may show up for N_2/H_2 mixtures as well. Summing up the flux of these main emission peaks, figure 6.8 shows the total VUV flux obtained from the plasma at different power and pressure conditions. The VUV flux appears to vary linearly with ICP power, but reaches a local maximum at around a pressure of 2.5 mTorr. Lower flux at 1 mTorr is likely due to lower gas density, while quenching of photons seems to occur at higher pressures. In fact, NH_3 plasma at a pressure of 1 mTorr cannot be ignited at ICP powers lower

than 150 W. Similar quenching of photons at higher pressures have also been observed in Ar and O_2 plasmas.[7,81]
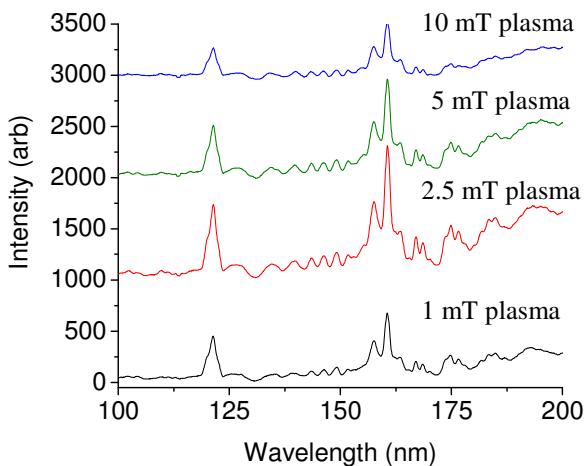
Figure 6.7 VUV spectra for NH_3 plasma at plasma pressures of 1-10 mTorr. ICP power input was 150 W.
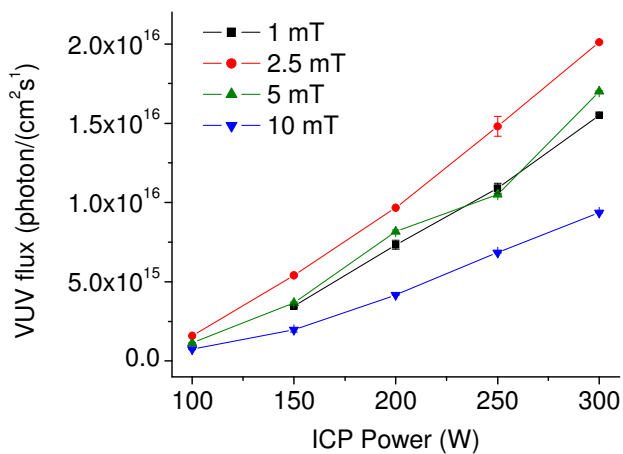
Figure 6.8 The total VUV flux of the major emission peaks for pressures of 1-10 mTorr and ICP power input of 100-300 W.
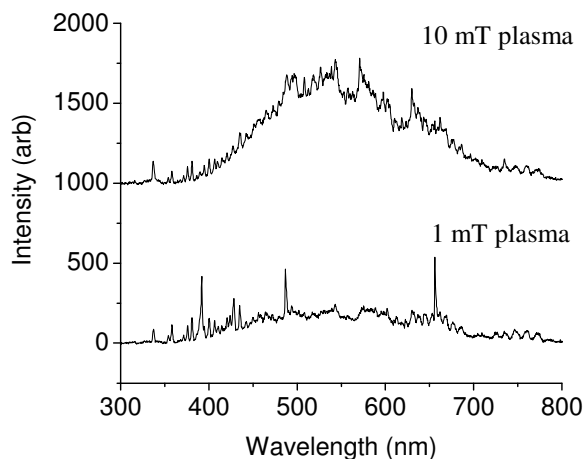
Figure 6.9 Optical emission spectra of NH_3 plasma (150 W) at 1 mTorr and 10 mTorr conditions.

Spectra captured with an optical emission spectrometer (Ocean Optics) show different emission peaks at different pressures, as shown in figure 6.9. For 1 mTorr NH_3 plasma, sharp peaks indicate dissociation of hydrogen (486 nm, 656 nm) and the excited states of molecular N_2 (391 nm, 427 nm).[105] The presence of these emissions indicate that a significant amount of NH_3 is fully dissociated, making the plasma similar to plasmas containing N_2 and H_2. More

76

dissociation would occur at lower pressures due to a higher electron temperature. Langmuir probe measurements shown in Appendix B support this observation. At higher pressures, these sharp peaks begin to disappear, and a broad emission band begins to dominate. The formation of a broad band occurs due to numerous nonradiative transitions that are present in NH_x compounds.[106,107] At 10 mTorr, only this broad band is visible, suggesting that the dissociation rate is much lower and mainly NH_x species are present. By changing the plasma pressure, two distinct emissions can be examined for NH_3 plasma.

6.4.3.2 Effect of NH₃ Plasma on Low-k Materials

By using NH_3 plasma under low and high pressure conditions, the effect on p-ULK films was examined. The effect of VUV radiation and radical species, such as atomic N/H and NH_x, can be investigated. As reported in earlier chapters, VUV photons typically break the Si-C bond and penetrate deep into the film. To minimize VUV flux, exposures were performed at the lowest power setting. Because of this, conditions of 100 W/10 mTorr and 150 W/1 mTorr were used. As noted earlier, the plasma density is too low to ignite NH_3 plasma at 100 W/1 mTorr. Under these conditions, the VUV flux was calculated to be 2.3×10^{14} and 1.5×10^{15} photons/(cm^2·s), respectively.
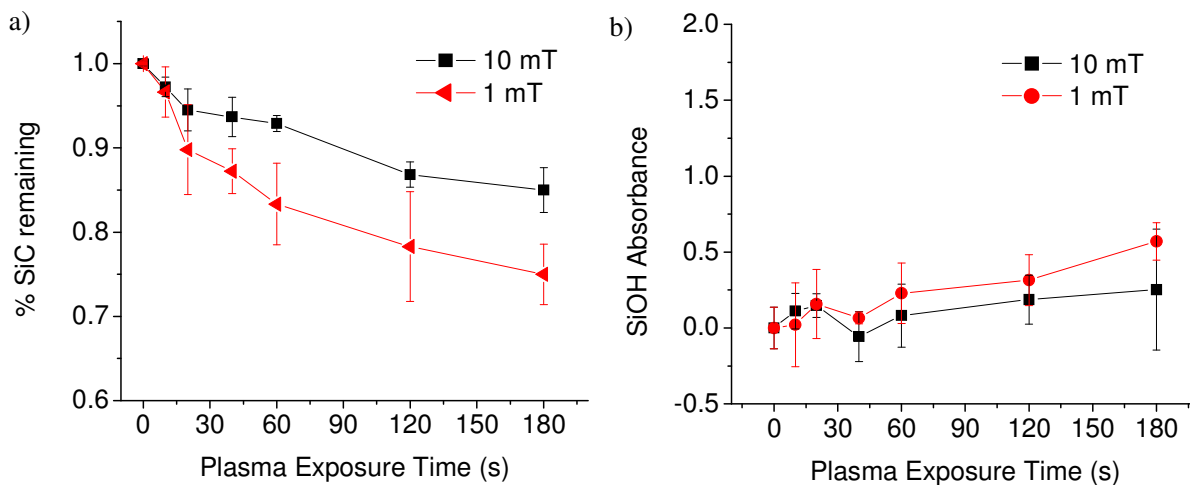
Figure 6.10 (a) Carbon loss and (b) growth of the SiOH water peak as measured by FTIR after NH_3 plasma exposure. Plasma conditions were 100 W/10 mTorr and 150 W/1 mTorr.

Figure 6.10 shows the carbon loss and growth of the water peak as measured by FTIR after NH_3 plasma treatment for up to 3 minutes. In both cases, a sharp drop in carbon appears in the initial 20 seconds, followed by a much slower rate of removal afterwards. Similar to O_2 plasma results in Chapter 5, radical damage appears to be dominant only at short times, with later carbon loss dominated by VUV radiation. A rough comparison of the experimental data with the VUV model supports this theory. For 1 mTorr, a larger initial drop is observed due to a higher concentration of dissociated hydrogen and nitrogen and/or higher VUV flux. Interestingly,

absorption of water vapor as seen in figure 6.10b is low despite considerable loss of carbon species. This may be due to nitrogen incorporation, which is limited to mainly $Si-NH_2$ bonds.[108] However, detection of amine bonds by FTIR is difficult because their vibrational frequency overlaps with the water peak. Since amine bonds also show up as a broad peak due to hydrogen bonding, the FTIR peaks cannot be deconvoluted. In any case, the absorbance in this entire region is low, so water absorption is undoubtedly hindered after NH_3 plasma treatment. Studies looking at NH_3 plasma treatments have suggested that NH_x compounds passivate reaction sites after Si-C bond scissioning, thereby preventing the formation of Si-OH and retaining some level of hydrophobicity.[109] Furthermore, this addition of nitrogen into low-k appears to shield the material against O_2 plasma damage as well.[110] Sealing of the pores via $Si-NH_2-Si$ branch formation has been reported to be one mechanism for this protection.[91,111] As a result, damage of the low-k is reduced compared to other exposures that remove an equivalent amount of carbon. However, improvements on this technique that draw out the sealing mechanism without extensive bulk carbon removal by VUV photons would be of great importance. This may be possible by using remote[65] or pulsed plasmas[112] to minimize the VUV flux or by ion bombardment in the presence of NH_3 to activate surface sites.[99]

6.5   Conclusions

Low-k materials with lower effective diffusivities, like d-ULK, show higher plasma resistance because plasma species are hindered from travelling into the film. Treatment techniques to induce a similar resistance in p-ULK were investigated. These techniques include densification by ion bombardment from He plasma and passivation by NH_x from NH_3 plasma. Since these species were generated through inductively-coupled plasmas, VUV photons also present in the exposure were observed to be damaging to the low-k material. Studies reported in previous chapters support this observation. Therefore, improvements would require performing these treatment methods in the absence of VUV photons. Limited reduction of photon exposure can be achieved by filtering the plasma species or limiting photon generation through a pulsed power source. Alternatively, independent sources, such as ion guns, can be used to increase plasma resistance of materials without strongly impacting the bulk. By treating only a thin layer near the surface of the film, a diffusive barrier can be created to block out a majority of plasma species. However, the mechanism for how plasma resistance occurs, whether by ion bombardment or NH_x passivation, still has not been thoroughly characterized. Further investigation on the transformation of this material post-treatment would greatly improve the understanding of how these treatments work.

Chapter 7
Conclusions

Through the analysis of individual plasma species, this work studies how plasma treatment affects porous low-*k* materials. These plasma studies include exposures in a high vacuum beam system and a separate inductively-coupled plasma system. This chapter summarizes the work performed in both systems and provides a framework for a fundamental understanding of the effect of VUV photons and radicals.

The first part of this dissertation analyzes the effect of VUV radiation from a closed lamp source on porous low-*k* films. Through this study, 147 nm wavelength photons were observed to break Si-C bonds in the material, leading to carbon extraction from the film. Furthermore, this behavior was synergistically enhanced by the presence of molecular O_2 in the background. Upon examination of reaction products emitted from the sample under the presence or absence oxygen, it was determined that oxidizing species were necessary to form volatile leaving products and cause irreversible carbon removal. The removal of these carbon species would lead to absorption of water vapor upon exposure to the atmosphere. Chemical changes to this material after these VUV treatments were measured through *ex-situ* transmission FTIR, which shows clear drops in the Si-C bending peak (1270 cm^{-1}) and increases in the broad water peak (3000-3800 cm^{-1}). The uptake of moisture into the material was determined to be due to the loss of hydrophobic carbon compounds, resulting in dramatic increases in the dielectric constant.

The role of VUV induced damage was examined for inductively-coupled plasmas, which also contain other plasma species that can affect the material. Comparison of Ar and O_2 plasmas with the VUV lamp yielded vast differences in the amount of carbon loss after a given dosage of photons. Characterization of the VUV spectrum showed that the emission wavelengths (105/107 nm for Ar, 130 nm for O_2 and 147 nm for Xe lamp) were significantly different. These different wavelengths are reported to have vastly different absorption coefficients for SiO_2 materials. As a result, longer wavelength emissions are able to penetrate deeper into the bulk material after carbon extraction from the film. This occurs because the material reverts to a SiO_2-like material. In contrast, short wavelength emissions are absorbed by SiO_2 such that carbon loss remains near the surface of the film. Additionally, results from these experiments do show that VUV photons can potentially be a major cause of damage during plasma treatment.

For plasmas generating multiple reactive species, such as photons and radicals, direct analysis of damage by individual species is difficult. For this reason, methods were designed to isolate these species for independent study. Good separation of photons and radicals can be achieved by covering the low-*k* samples in different ways. Shielding the sample with a MgF_2 window would only allow VUV photons to pass through. Placing the sample out of the line-of-sight of the plasma allows for a radical only exposure, since radicals are able to diffuse around and to the material. After performing exposures to either photons or radicals, a dilute HF solution can be used to strip off the damaged SiO_2-like layer. Through HF stripping and FTIR analysis, carbon removal was observed to occur differently for photons and radicals generated from O_2 plasma. 130 nm wavelength photons are fairly transparent through the material, leading to carbon removal distributed throughout the film. In contrast, radical effects are diffusion-limited, which leads to a front-like propagation of carbon removal.

Simulation of these photon and radical effects on low-*k* can be achieved through simple modeling equations. For photon exposures, VUV photons impact the film at a specified flux, as measured by a VUV spectrometer. The quenching of these photons is dictated by absorption coefficients, obtained from literature, as they travel through the film. At the same time, these photons also cause carbon removal as indicated by the photolysis cross section. VUV model predictions show good agreement with experimental results. For radical exposures, a diffusion-reaction model is used to describe radical transport and carbon removal within the film. However, damage by radicals can only be modeled if a region of low permeability is assumed to be present at the surface of the film.

While the experiment and model results agree under radical or photon exposure alone, carbon removal under direct plasma exposure is predicted to be much faster in the model than observed experimentally. Short plasma treatments followed by radical exposure show that very little additional damage occurs by the radicals alone. In contrast, photon damage is not significantly affected by a short plasma treatment beforehand. The most straightforward interpretation of these results appears to be that photons combine synergistically with radicals to narrow the pores during a simultaneous exposure, restructuring the SiO_2 network and effectively reducing the film diffusivity in carbon-poor, plasma-damaged regions. Modeling results support these findings.

These studies have shown that plasma species, such as radicals and photons, damage porous low-*k* materials. Furthermore, factors such as the photon wavelength and radical diffusion have been shown to play significant roles in the extent of carbon removal from this material. Treatment methods that are designed to limit plasma damage through reduction of film diffusivity show promise. These treatment methods are typically combined with adjustment of plasma processing parameters in order to reduce the generation of photons or reactive radicals. Optimization of these treatment methods to further restrict damage to thinner regions of the film is still necessary. Furthermore, fundamental understanding of the protection mechanisms that results from these treatments have yet to be investigated thoroughly.

In summary, this dissertation shows that fundamental understanding of plasma/material interactions is necessary for the advancement of interconnect technology. The reduction of dielectric permittivity while maintaining plasma resistance is a major challenge for continuous miniaturization of semiconductor devices. Therefore, knowledge of how plasma species behave and what factors contribute to the generation/transport of these species is of crucial importance. This study demonstrates how a complicated plasma discharge can be dissected and analyzed independently, systematically leading to the understanding of damage mechanisms and the subsequent design of methods to improve plasma processing.

Appendix A
Isolation of Plasma Species

During a plasma discharge, a multitude of species are generated, including ions, electrons, photons, and radicals. Even when dealing with relatively simple chemistries, such as with a pure O_2 plasma, it becomes quite difficult to identify the reasons for differences in plasma-induced effects under different plasma exposures. To some extent, dominating effects can be observed by certain species under certain plasma conditions. However, the outcome of plasma treatments, especially at more complicated chemistries, is discovered usually by trial-and-error. Thus, it is desirable to understand fundamentally how the plasma species interact individually with the material.

One method of achieving this is to use beam sources that generate specific species. While this method has been shown to work, both in this study and in the past, often these beam sources have very low flux or operate under limited conditions.[9,66] As a result, they work well in a mechanistic study, but results are not always comparable to a plasma exposure. Other methods look to filter a plasma discharge by using a window or shield to block certain species from passing.[32,84] These methods hold much promise, and the current ICP system can be adapted to perform such studies.

Re-design of the sample holder was performed in order for this study to occur. The objective was to create an enclosed region that would isolate the samples from the main plasma discharge. Since the importance of the study was to examine the effects of VUV photons and radicals, the shielding caps were designed around methods that permit these species to pass (Figure A.1). For exposure to only VUV photons, the sample would have to be sealed off from the plasma with a MgF_2 window, which allows for radiation >115 nm to pass through. To achieve this, two Teflon rings were created, one with a slot cut out to allow for the MgF_2 window to rest flush between the two rings, which were screwed down onto the copper plate. This created an enclosed region, just small enough to fit a sample of the low-k film. While this holder was not airtight, the aperture for diffusion was small enough to prevent any radicals from entering, so only molecular gas species would enter. By replacing the MgF_2 window with a metal plate, the absence of any effect by radicals was confirmed. In fact, having an airtight seal is not desirable because that would make pumping the enclosed region very difficult. If the pressure inside does not decrease, the VUV radiation will inevitably be absorbed by air. For radical exposures, blocking line-of-sight species was the most important aspect, since radicals

can survive multiple collisions while diffusing to the sample. As a result, a larger Teflon cap, oriented with the sample facing away from the plasma emission, with an aperture wide enough for radical species to diffuse through was needed. This cap would be elevated by ~1 mm by some screws to create an opening for the radicals. To check for any residual transmittance of VUV radiation, the sample was covered with a MgF_2 window under this configuration. Through this, it appears that the setup successfully filters out all radiation, leaving only radical effects.
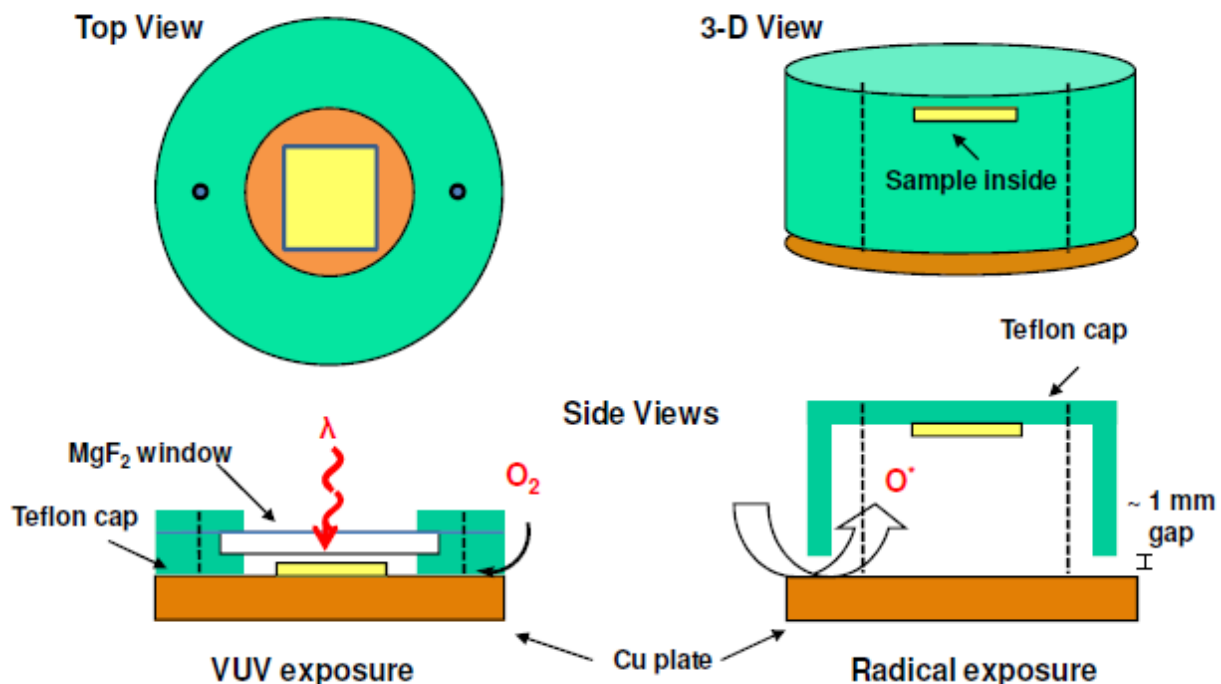
Figure A.1 Various views of the shielding caps used to filter out plasma species. The setup on the left is used for VUV-only exposures, while the setup on the right is used for radical-only exposures.

Another issue encountered by filtering plasma species is that the flux of the desired specie will inevitably be reduced in the process. For radical exposures, the setup creates more surfaces and a longer diffusion path in which the chance that radicals can recombine increases. The recombination rate is greatly affected by the type of surfaces that are present in the chamber.[86,89] Unfortunately, this makes estimation of the decrease in the radical flux difficult to perform. For VUV exposure, the photons have to pass through the MgF_2 window to impact the sample. Transparency curves for MgF_2 are available, typically from the manufacturer's website, for a range of wavelengths. However, the thickness of the window is crucial, especially in the range of 115-150 nm, where the absorption coefficient changes rapidly. As a result, it is necessary to measure the reduction of VUV flux manually using the VUV spectrometer. This process can be performed by inserting the MgF_2 window between the plasma and the detector of

the VUV spectrometer. Comparison of the VUV spectra in the presence and absence of the window yields the fractional transmittance. For O_2 plasma (λ = 130 nm), the transmittance was found to vary between 46% and 70% from window to window, despite being of approximate similar thickness (2 mm).

In addition to MgF_2, other windows can be used to obtain radiation at different ranges. LiF and CaF_2 windows have different cutoff ranges in the VUV regime, while materials such as fused silica and sapphire cutoff radiation below 170 nm, allowing for UV radiation only. Having different cutoff points allow for the study of specific radiation wavelengths, useful for when the emission spectrum is more complex. Furthermore, SiOCH dielectric materials are still susceptible to higher wavelength emissions (up to 265 nm), since the respective bonding energy of Si-C is reported to be 451 kJ/mol.[57] Through choice of plasma chemistry and the material of the filter, the working wavelength can be changed to allow for controlled UV/VUV emissions. Thus, it becomes possible to experiment with multiple wavelengths without the need of independent sources. The benefit of this technique works not only for exposure to dielectrics and can possibly extend to other materials, such as polymers, semiconductors, biofilms, etc.[58,113,114]

Appendix B
Supplemental Plasma Characterization Data

B.1   Introduction

B.2   Supplemental Langmuir Probe Measurements

B.3   Supplemental VUV/Ion Measurements

B.4   Flux Conversion Parameters

B.1   Introduction

This appendix contains documentation of key parameters in the characterization of inductively-coupled plasmas. This documentation is for supplementing plasma exposures used in the studies in Chapters 4-6. Choice of plasma conditions during these studies was considered after examining the plasma emissions at various pressures and input powers. A variety of gas chemistries were also examined, though not all of the examined conditions were put to use. Emphasis on comparable VUV photon fluxes with the Xe VUV lamp was most important in these studies, and as a result, plasmas at low power inputs were necessary for study. The plasmas mainly examined here are He, O_2, and NH_3, with Ar to a lesser extent, under low pressure and power conditions. Further documentation of Ar, O_2 and Cl plasmas can also be found in the dissertations of Cheng-Che Hsu and Monica Titus.[45,46] Data of VUV flux measurements were also used as modeling parameters for estimation of carbon removal from porous SiOCH films through photolysis. Further details of this modeling are explained in Appendix C.

B.2 Supplemental Langmuir Probe Measurements

Table B.1 Experimental He plasma Langmuir probe measurements. The probe was 2.54 cm above the lower electrode and rested at various radial distances within the chamber, i.e. center (r = 0 cm), middle (r = 4.1 cm), and edge (r = 8.6 cm).

Pressure (mT)	ICP Power (W)	Electron Density (n_e/cm³)			Te (eV)			Plasma Potential (eV)		
		Center	Middle	Edge	Center	Middle	Edge	Center	Middle	Edge
20	150	5.6E+09	5.2E+09	1.9E+09	9.2	10.0	7.9	38.1	38.1	27.5
20	200	9.4E+09	7.8E+09	3.0E+09	9.7	9.7	8.4	38.7	36.9	27.9
30	150	8.7E+09	7.3E+09	2.5E+09	8.4	8.1	6.8	33.0	31.1	22.5
30	200	1.4E+10	1.1E+10	3.4E+09	9.3	9.0	6.3	35.0	33.0	21.3
40	100	7.1E+09	5.9E+09	2.1E+09	7.5	7.3	6.1	29.9	27.9	20.5
40	150	1.3E+10	1.1E+10	3.9E+09	8.4	8.2	6.2	31.4	29.5	20.5
40	200	1.8E+10	1.5E+10	5.5E+09	9.1	8.7	7.1	32.6	30.7	22.5
50	100	9.4E+09	7.6E+09	2.7E+09	7.4	7.1	5.8	28.3	26.4	18.9
50	150	1.6E+10	1.3E+10	4.9E+09	8.6	8.0	6.1	30.3	28.3	19.7
50	200	2.1E+10	1.8E+10	6.9E+09	9.3	8.7	6.9	31.8	29.5	21.3
60	100	1.2E+10	9.6E+09	3.6E+09	7.7	7.4	6.2	28.3	26.4	19.3
60	150	1.8E+10	1.5E+10	5.3E+09	8.4	7.9	5.9	29.5	27.3	18.8
60	200	2.4E+10	2.0E+10	7.5E+09	9.6	8.8	6.7	31.6	29.1	20.5

Table B.2 Experimental O_2 plasma Langmuir probe measurements. The probe was 2.54 cm above the lower electrode and rested at various radial distances within the chamber, i.e. center (r = 0 cm), middle (r = 4.1 cm), and edge (r = 8.6 cm).

Pressure (mT)	ICP Power (W)	Electron Density (n_e/cm^3)			Te (eV)			Plasma Potential (eV)		
		Center	Middle	Edge	Center	Middle	Edge	Center	Middle	Edge
1	150	1.1E+10	1.0E+10	4.6E+09	6.9	6.7	7.6	39.3	38.5	35.7
1	200	2.1E+10	1.3E+10	7.0E+09	6.1	7.6	8.9	38.1	38.9	37.3
1	250	1.9E+10	1.9E+10	9.1E+09	10.7	10.2	10.8	44.3	43.6	40.4
1	300	1.9E+10	2.0E+10	1.1E+10	12.7	10.7	11.6	46.3	43.2	41.6
2.5	150	1.3E+10	1.2E+10	7.3E+09	9.1	8.8	7.8	34.6	33.8	29.5
2.5	200	1.8E+10	1.7E+10	9.3E+09	10.8	10.8	8.3	37.3	36.9	29.5
2.5	250	2.4E+10	2.3E+10	1.3E+10	12.5	11.6	9.3	40.0	38.1	31.1
2.5	300	2.9E+10	2.8E+10	1.6E+10	13.2	11.9	8.8	41.2	38.7	29.9
5	150	1.4E+10	1.3E+10	7.5E+09	6.6	6.6	5.6	27.1	26.8	22.9
5	200	1.9E+10	1.8E+10	1.1E+10	8.6	8.5	6.7	30.3	29.9	24.4
5	250	2.1E+10	2.0E+10	1.4E+10	9.7	9.5	7.9	31.8	32.0	26.4
5	300	2.8E+10	2.7E+10	1.6E+10	11.6	11.1	8.4	35.0	33.8	27.1
10	150	1.3E+10	1.3E+10	7.4E+09	5.1	5.1	4.4	22.1	21.7	18.9
10	200	1.5E+10	1.5E+10	9.9E+09	7.0	7.0	5.4	24.8	24.8	20.5
10	250	2.1E+10	2.0E+10	1.3E+10	7.8	7.4	5.6	26.4	25.4	20.7
10	300	2.5E+10	2.5E+10	1.5E+10	8.4	8.0	7.7	27.1	26.4	24.4
20	150	1.1E+10	9.8E+09	6.0E+09	5.7	5.5	4.3	20.9	20.3	17.0
20	200	1.6E+10	1.6E+10	9.7E+09	5.6	5.5	4.5	20.5	20.5	17.2
20	250	2.0E+10	1.9E+10	1.2E+10	6.2	6.3	5.3	21.7	21.7	18.6
20	300	1.9E+10	2.3E+10	1.4E+10	7.3	7.8	6.3	23.0	24.0	20.5

Table B.3 Experimental NH₃ plasma Langmuir probe measurements. The probe was 2.54 cm above the lower electrode and rested at various radial distances within the chamber, i.e. center (r = 0 cm), middle (r = 4.1 cm), and edge (r = 8.6 cm).

Pressure (mT)	ICP Power (W)	Electron Density (n_e/cm^3)			Te (eV)			Plasma Potential (eV)		
		Center	Middle	Edge	Center	Middle	Edge	Center	Middle	Edge
1	150	1.1E+10	9.7E+09	5.3E+09	5.3	5.4	6.0	33.8	33.4	31.4
1	200	1.7E+10	1.6E+10	8.8E+09	5.9	5.9	6.6	35.0	34.6	32.6
1	250	2.3E+10	2.0E+10	1.2E+10	6.1	6.3	7.0	35.7	35.4	33.4
1	300	2.8E+10	2.5E+10	1.4E+10	6.5	6.7	7.8	37.3	36.9	35.4
2.5	100	1.0E+10	9.2E+09	5.9E+09	4.9	4.8	4.5	25.6	24.8	22.5
2.5	150	1.8E+10	1.6E+10	1.1E+10	5.0	5.0	5.3	26.0	25.6	24.0
2.5	200	2.3E+10	2.5E+10	1.5E+10	4.8	4.4	5.6	25.6	24.8	24.8
2.5	250	3.3E+10	3.0E+10	1.6E+10	4.6	4.8	5.9	26.0	25.6	24.2
2.5	300	3.9E+10	3.7E+10	2.4E+10	4.8	4.9	5.2	26.4	26.0	24.4
5	100	1.5E+10	1.5E+10	8.2E+09	3.1	3.3	3.4	19.3	19.3	17.4
5	150	2.6E+10	2.3E+10	1.5E+10	3.4	3.5	3.8	20.1	19.7	18.6
5	200	3.3E+10	3.0E+10	2.0E+10	3.6	3.6	4.0	20.5	20.1	18.9
5	250	4.0E+10	3.6E+10	2.4E+10	3.7	3.8	4.1	20.9	20.5	19.3
5	300	4.7E+10	4.3E+10	2.9E+10	3.8	3.9	4.3	21.3	20.9	19.7
10	100	2.0E+10	1.8E+10	1.1E+10	2.8	2.8	3.1	16.6	16.2	15.0
10	150	2.9E+10	2.8E+10	1.8E+10	2.9	3.0	3.1	16.6	16.6	15.4
10	200	3.7E+10	3.6E+10	2.3E+10	3.0	3.1	3.2	17.0	17.0	15.8
10	250	4.5E+10	4.0E+10	2.6E+10	3.1	3.1	3.2	17.4	17.0	15.8
10	300	4.8E+10	4.8E+10	3.2E+10	3.1	3.2	3.3	17.4	17.4	16.2

Table B.4 Experimental Ar plasma Langmuir probe measurements. The probe was 2.54 cm above the lower electrode and rested at various radial distances within the chamber, i.e. center (r = 0 cm), middle (r = 4.1 cm), and edge (r = 8.6 cm).

Pressure (mT)	ICP Power (W)	Electron Density (n_e/cm^3)			Te (eV)			Plasma Potential (eV)		
		Center	Middle	Edge	Center	Middle	Edge	Center	Middle	Edge
10	35	2.2E+10	2.1E+10	1.2E+10	3.1	3.2	3.4	16.2	16.2	14.6
10	70	4.8E+10	4.8E+10	2.7E+10	3.4	3.4	3.4	16.2	16.2	14.3
10	160	1.2E+11	1.1E+11	7.0E+10	3.5	3.5	3.5	16.6	16.2	14.6
20	35	3.3E+10	2.9E+10	1.5E+10	3.1	3.1	3.1	14.6	14.3	12.3
20	70	7.7E+10	7.0E+10	3.6E+10	3.1	3.1	3.0	14.6	14.3	12.3
20	160	1.9E+11	1.7E+11	1.3E+11	3.0	3.0	3.0	14.6	14.3	13.5
50	35	8.0E+10	7.0E+10	3.2E+10	2.7	2.7	2.6	13.1	12.7	10.7
50	70	1.8E+11	1.8E+11	8.0E+10	2.4	2.5	2.4	12.7	12.7	10.7
50	160	4.4E+11	4.5E+11	2.2E+11	2.3	2.3	2.2	12.3	12.3	10.7

B.3   Supplemental VUV/Ion Measurements

Table B.5 Experimental Ar plasma VUV/ion measurements. VUV flux was measured through a calibrated VUV spectrometer. The ion flux was measured using a probe at the wall of the chamber.

Pressure (mT)	ICP Power (W)	VUV flux (photons/cm²/s)			Ion Current (mA)	Ion Flux (ions/cm²/s)	VUV/ion Ratio
		105 nm	107 nm	Total			
10	70	1.2E+15	2.3E+15	3.4E+15	0.34	5.2E+15	0.64

Table B.6 Experimental O_2 plasma VUV/ion measurements. VUV flux was measured through a calibrated VUV spectrometer. The ion flux was measured using a probe at the wall of the chamber.

Pressure (mT)	ICP Power (W)	VUV flux (photons/cm²/s)			Ion Current (mA)	Ion Flux (ions/cm²/s)	VUV/ion Ratio
		130 nm	135 nm	Total			
1	150	1.1E+15	3.2E+14	1.5E+15	0.35	5.4E+15	0.27
1	200	2.0E+15	5.0E+14	2.5E+15	0.57	8.9E+15	0.29
1	250	3.0E+15	6.6E+14	3.6E+15	0.76	1.2E+16	0.31
1	300	4.0E+15	8.1E+14	4.8E+15	0.95	1.5E+16	0.32
2.5	150	2.0E+15	5.1E+14	2.5E+15	0.51	8.0E+15	0.31
2.5	200	3.4E+15	7.8E+14	4.2E+15	0.75	1.2E+16	0.36
2.5	250	4.6E+15	1.0E+15	5.5E+15	0.95	1.5E+16	0.37
2.5	300	5.0E+15	1.2E+15	6.2E+15	1.16	1.8E+16	0.34
5	150	1.9E+15	3.9E+14	2.2E+15	0.47	7.4E+15	0.30
5	200	3.2E+15	6.4E+14	3.8E+15	0.69	1.1E+16	0.35
5	250	4.4E+15	8.5E+14	5.3E+15	0.89	1.4E+16	0.38
5	300	5.1E+15	1.1E+15	6.2E+15	1.11	1.7E+16	0.36
10	150	1.2E+15	1.9E+14	1.4E+15	0.38	5.9E+15	0.23
10	250	3.5E+15	5.0E+14	4.0E+15	0.73	1.1E+16	0.35
10	200	2.0E+15	3.0E+14	2.3E+15	0.55	8.6E+15	0.27
10	300	4.8E+15	6.8E+14	5.4E+15	0.92	1.4E+16	0.38
20	150	1.2E+15	9.9E+13	1.3E+15	0.29	4.6E+15	0.29
20	200	2.2E+15	1.9E+14	2.3E+15	0.43	6.7E+15	0.35
20	250	3.1E+15	2.7E+14	3.4E+15	0.55	8.6E+15	0.39
20	300	4.4E+15	3.7E+14	4.8E+15	0.70	1.1E+16	0.43

Table B.7 Experimental NH_3 plasma VUV/ion measurements. VUV flux was measured through a calibrated VUV spectrometer. The ion flux was measured using a probe at the wall of the chamber.

Pressure (mT)	ICP Power (W)	VUV flux (low λ) (photons/cm²/s)			VUV flux (high λ) (photons/cm²/s)			Ion Current (mA)	Ion Flux (ions/cm²/s)	VUV/ion Ratio
		121 nm	124 nm	Total	158 nm	161 nm	Total			
1	150	5.6E+14	9.7E+14	1.5E+15	9.5E+14	1.5E+15	2.5E+15	0.28	4.4E+15	0.34
1	200	1.2E+15	2.1E+15	3.3E+15	2.0E+15	3.2E+15	5.2E+15	0.48	7.5E+15	0.44
1	250	2.0E+15	3.2E+15	5.2E+15	3.1E+15	4.6E+15	7.7E+15	0.65	1.0E+16	0.51
1	300	2.7E+15	4.6E+15	7.3E+15	4.2E+15	6.7E+15	1.1E+16	0.81	1.3E+16	0.57
2.5	100	2.1E+14	4.3E+14	6.4E+14	4.1E+14	7.5E+14	1.2E+15	0.29	4.5E+15	0.14
2.5	150	7.4E+14	1.4E+15	2.2E+15	1.5E+15	2.5E+15	4.0E+15	0.50	7.9E+15	0.27
2.5	200	1.5E+15	2.6E+15	4.0E+15	2.7E+15	4.4E+15	7.1E+15	0.70	1.1E+16	0.37
2.5	250	2.2E+15	3.9E+15	6.1E+15	4.1E+15	6.8E+15	1.1E+16	0.90	1.4E+16	0.43
2.5	300	3.2E+15	5.5E+15	8.7E+15	5.5E+15	9.1E+15	1.5E+16	1.09	1.7E+16	0.51
5	100	1.2E+14	3.0E+14	4.2E+14	2.8E+14	5.6E+14	8.4E+14	0.32	5.0E+15	0.08
5	150	4.2E+14	9.1E+14	1.3E+15	9.8E+14	1.8E+15	2.7E+15	0.51	8.0E+15	0.17
5	200	9.7E+14	2.1E+15	3.1E+15	2.3E+15	3.8E+15	6.1E+15	0.70	1.1E+16	0.28
5	250	1.5E+15	2.9E+15	4.4E+15	3.2E+15	4.4E+15	7.6E+15	0.88	1.4E+16	0.32
5	300	2.4E+15	4.3E+15	6.7E+15	4.7E+15	8.0E+15	1.3E+16	1.06	1.6E+16	0.40
10	100	1.2E+13	2.2E+14	2.3E+14	1.8E+14	3.5E+14	5.3E+14	0.29	4.5E+15	0.05
10	150	1.4E+14	4.8E+14	6.3E+14	5.0E+14	9.7E+14	1.5E+15	0.45	7.0E+15	0.09
10	200	4.1E+14	1.0E+15	1.4E+15	1.1E+15	2.0E+15	3.1E+15	0.60	9.4E+15	0.15
10	250	7.6E+14	1.7E+15	2.4E+15	1.9E+15	3.3E+15	5.2E+15	0.76	1.2E+16	0.21
10	300	1.2E+15	2.4E+15	3.6E+15	2.8E+15	4.1E+15	6.9E+15	0.91	1.4E+16	0.26

B.4   Flux Conversion Parameters

B.4.1   VUV Flux

Measurements of photon emissions performed by the VUV spectrometer were conducted during plasma exposures. The intensities of the emissions within the wavelength range of 100-200 nm were recorded. In order to obtain absolute flux values, calibration was performed on the VUV spectrometer using a VUV lamp of known flux, and an adjustment was made to account for the distance of the spectrometer from the lamp. The arbitrary intensity values obtained from the spectrometer were input into the following equation to obtain the equivalent VUV flux, Γ, at each wavelength:

$$\Gamma = \frac{I}{I_0}\Gamma_0\Omega a \tag{B.1}$$

where I is the intensity of the measured signal, Ω is the solid angle factor to account for distance, and a is the spectrometer sensitivity factor. I_0 and Γ_0 are the intensity and flux of the VUV lamp used for calibration, respectively. When examining the VUV emissions, only major emission peaks are examined. Note that the spectrometer sensitivity factor will change at different emission wavelengths as according to the grating efficiency of the detector. Furthermore, the intensity collected by the detector is typically performed at an integration time of 4 seconds. For certain plasma conditions, the integration time must be decreased because the detection limit has been reached. As a result, adjustments to the equation above to account for the intensity must be made.

B.4.2   Ion Flux

During a plasma discharge, the positive ion current can be measured with a probe located at the wall of the chamber. The negative bias has been set to 40V to collect ions as current. This current value is recorded by a multimeter at set intervals, allowing for real time measurement throughout the plasma emission. The total positive ion flux, Γ_i, can thus be calculated as such:

$$\Gamma_i = \frac{i}{eA} \tag{B.2}$$

where i is the positive ion current collected by the probe, e is the charge of an electron, and A is the probe area. The ion species are not examined extensively in this study due to their relatively low energy and low penetration ability when generated by an unbiased inductively-coupled plasma. However, the distribution of ion species can still be examined by using an ion mass spectrometer. Furthermore, the measured ion current during a plasma discharge allows for easy monitoring of the plasma stability. Changes in the ion current are displayed instantaneously, making it useful when the plasma conditions are changed and the matching network for the coil needs to be optimized.

Appendix C
COMSOL Modeling

Modeling of VUV photon and radical effects on porous low-k films was performed using COMSOL simulation package (Version 3.5a). The flux of species was assumed to be constant along the surface of the film, such that only 1-D modeling was necessary. The models represent a constant concentration of either photons or radicals impacting the surface of the film and track the decay of the flux as a function of depth into the film, up to 230 nm. Through kinetic parameters, these species react with a given concentration of carbon within the film, creating a profile as a function of depth as shown in figure C.1.

Figure C.1 Schematic of VUV/radical transport into a porous low-k film. Species travel through the film and react with carbon to create a concentration profile.

When constructing the model in COMSOL, three separate core equations were used to track the change in the photon intensity, radical concentration, and carbon concentration, which were specified in the subdomain settings. A line with x-coordinates of $(0, 2.3 \times 10^{-5}$ cm) was specified to examine the dependency of parameters as function of depth into the film. Global equations were used to calculate other transient parameters, such as the film attenuation coefficient. To specify an in-flux of photons and radicals, a boundary setting was input at x = 0. The model was solved for a period of 1800 seconds, using a time step of 1 second. Due to the large numbers used in the model, the simulation would occasionally have difficulty converging. This can be solved by specifying non-zero constants for the initial conditions of some parameters. Formulation of the equations and specified constants are described in detail below.

The properties in the p-ULK film were estimated to simplify the model calculations. This material is basically silicon oxide doped with carbon species, which are lost after plasma treatment. For this reason, the composition of the p-ULK material was assumed to be a homogenous distribution of Si-C bonds, Si-O bonds, and porosity. Values of 25% carbon and 75% oxide were chosen for the model. The porosity of the film was stated to be ~30% by the supplier of the material. Given these parameters, a rough estimate of the carbon concentration in the film can be calculated. For SiO_2, 2.65 g·cm^{-3} for the density of SiO_2 and 3.9 for the dielectric constant are typical values. By reducing the density based on the ratio of the dielectric constants, this would be converted to a molecular concentration of 1.6×10^{22} cm^{-3}, resulting in a carbon concentration of 4.0×10^{21}. However, for the purposes of this model, a normalized carbon concentration can be used in order to compare with experimental data as measured by FTIR. In FTIR, the drop in the Si-C bending peak at 1270 cm^{-1} is used to indicate carbon loss. The ratio of the integrated peak before and after plasma treatment shows the fractional carbon loss in the film.

$$\alpha_t(x,t) = \alpha_{SiC}n_{SiC}(x,t) + \alpha_{SiO}n_{SiO} + \alpha_p n_p \tag{C.1}$$

$$\frac{dI}{dx} = -\alpha_t(x,t)I(x,t) \tag{C.2}$$

$$\frac{dn_{SiC}}{dt} = -I(x,t)\sigma_{SiC}n_{SiC}(x,t) \tag{C.3}$$

The modeling equations for VUV penetration and carbon removal from the film are shown above. In these equations, the concentrations of the film species are normalized. It has also been assumed that changes in the Si-O concentration are negligible and that the porosity remains constant, yet small changes in these parameters are possibly occurring. During the course of plasma exposure, only the Si-C concentration changes, affecting the total attenuation coefficient, α_t. The individual attenuation coefficients are calculated from values reported in literature.[72] The decay of the photon intensity, I, through the depth of the film is dictated by this total attenuation coefficient. Lastly, this photon intensity profile dictates the reduction of carbon, n_{SiC}, through a photolysis cross section, σ_{SiC}. As a result, the carbon removal relies heavily on how easily the photons can travel through the p-ULK film and the probability that a photon will find a Si-C bond and break it.

While this photolysis cross section technically does not rely on the interaction of other species, the fitting of this parameter can be influenced by the O_2 concentration during VUV exposures. While the photons break the Si-C bonds, it is necessary for O_2 to be present to complete the carbon removal, which is then detected by FTIR. In the case of p-ULK films, it was found that the diffusion was sufficiently high to neglect variations in pressure of oxidizing species under VUV exposure alone. This was shown to be not the case under direct plasma exposure. Table C.1 shows the modeling parameters that were used in the VUV model for emissions from different plasma chemistries.

Table C.1 Modeling parameters used for the VUV model.

Parameters	Xe lamp	O_2 plasma	NH_3 plasma†	Ar plasma	He plasma*
Pressure (mTorr)	--	10	10	10	30
Power (W)	--	150	100	70	100
Photon Wavelength, λ (nm)	147	130	124	105	58
VUV Flux (photons/(cm^2·s))	1.3×10^{14}	1.0×10^{15}	2.3×10^{14}	1.1×10^{15}	4.0×10^{15}
α_{SiC}	3.58×10^{-2}	3.74×10^{-2}	3.69×10^{-2}	3.51×10^{-2}	1.73×10^{-2}
α_{SiO}	1.42×10^{-4}	2.85×10^{-3}	2.01×10^{-2}	5.30×10^{-2}	5.36×10^{-2}
σ_{SiC} (cm^2)	8.8×10^{-18}	1.4×10^{-17}	2.2×10^{-17}	3.1×10^{-18}	1.3×10^{-17}

* (For He plasma, accurate measurement of the VUV flux could not be obtained.)
$\dagger$ (For NH_3 plasma, these parameters were obtained without isolating the radical effects.)

In general, the photon flux was measured using a VUV spectrometer attached to the inductively-coupled plasma system, and σ_{SiC} was fitted to experimental data obtained from FTIR. As noted above, accurate measurement of the VUV flux could not be obtained in the case of He plasma, and radicals generated in a NH_3 plasma were not isolated before modeling. As a result, σ_{SiC} values shown for these two exposures may be affected by these issues. In the case of O_2 plasma, the presence of radicals was observed to affect the fitted photolysis cross section, resulting in a value of 3.1×10^{-18} cm^2, about an order of magnitude lower than VUV exposure only. During plasma treatment, the diffusivity is believed to decrease significantly, which would also affect molecular O_2 transport and decrease the rate of carbon removal. This effect could account for a lower photolysis cross section needed to fit the carbon loss. However, the VUV model appears to work reasonably with a range of VUV wavelengths, despite the presence of radical species or imperfect VUV measurements. The basic trend of carbon loss as a function of VUV fluence seems to be predicted reasonably, and the carbon profile along the depth of the film appears to be consistent with theory.

$$\frac{dc_{o*}}{dt} + \nabla\left(-D\frac{\partial c_{o*}}{\partial x}\right) = -kc_{o*}n_{SiC} \tag{C.4}$$

$$\frac{dn_{SiC}}{dt} = -kc_{o*}n_{SiC} \tag{C.5}$$

The modeling equations for radical effects are shown above and represent typical diffusion-reaction behavior. In this study, only the effect of oxygen radicals was examined, but it could potentially be applied to other radical species. For these equations, it is presumed that the surface of the film is subjected to oxygen radicals at a given concentration, c_{o*}. These radicals diffuse into the film with an effective diffusivity, D, and react with carbon at a rate

constant, k. The oxygen radical concentrations can be estimated based on previous results,[86] and concentrations on the order of 10^{12}-10^{13} were used. However, little information was available for the diffusivity and rate constant. Rough calculations based on average pore diameters would yield a diffusivity of about ~10^{-4} cm^2/s, with the possibility of it being significantly lower with high tortuosity. Since radical damage was experimentally observed to produce a sharp carbon front, the reaction must be diffusion-limited, resulting in a high k/D ratio. By comparing with experimental data, the resulting reaction rate can be adjusted to match the observed carbon front. As a result, a diffusivity of 1.0×10^{-4} cm^2/s and a rate constant of 8.0×10^8 cm^3/s were used in the model. Using these parameters, along with some adjustments as detailed in Chapter 5, the carbon removal by radical exposure could be simulated approximately.

References

[1]   C. C. Hu, *Modern Semiconductor Devices for Integrated Circuits*. (Pearson, New Jersey, 2010).

[2]   C. Steinbruchel, *Appl. Surf. Sci.* **91**, 139 (1995).

[3]   K. Maex, M.R. Baklanov, D. Shamiryan, F. Iacopi, S. H. Brongersma, and Z. S. Yanovitskaya, *J. Appl. Phys.* **93**, 8793 (2003).

[4]   V. Rouessac, L. Favennec, B. Remiat, V. Jousseaume, G. Passemard, and J. Durand, *Microelectron. Eng.* **82**, 333 (2005).

[5]   A. Grill and D. A. Neumayer, *J. Appl. Phys.* **94**, 6697 (2003).

[6]   S. Yasuhara, J. Chung, K. Tajima, H. Yano, S. Kadomura, M. Yoshimaru, N. Matsunaga, T. Kubota, H. Ohtake, and S. Samukawa, *J. Phys. D: Appl. Phys.* **42**, 055208 (2009).

[7]   M. R. Baklanov and K. Maex, *Philos. T. Roy. Soc. A* **364**, 201 (2006).

[8]   M. A. Lieberman and A. J. Lichtenberg, *Principles of Plasma Discharges and Materials Processing*. 2nd ed. (Wiley, New York, 2005).

[9]   J. R. Woodworth, M. E. Riley, V. A. Amatucci, T. W. Hamilton, and B. P. Aragon, *J. Vac. Sci. Technol. A* **19**, 45 (2001).

[10]   M. J. Titus, D. Nest, and D. B. Graves, *Appl. Phys. Lett.* **94**, 171501 (2009).

[11]   J. Bao, H. Shi, J. Liu, H. Huang, P. S. Ho, M. D. Goodner, M. Moinpour, and G. M. Kloster, *J. Vac. Sci. Technol. B* **26**, 219 (2008).

[12]   M. Chaudhari, J. Du, S. Behera, S. Manandhar, S. Gaddam, and J. Kelber, *Appl. Phys. Lett.* **94**, 204102 (2009).

[13]   E. Kondoh, T. Asano, A. Nakashima, and M. Komatu, *J. Vac. Sci. Technol. B*. **18**, 1276 (2000).

[14]   H. J. Lee, E. K. Lin, H. Wang, W. L. Wu, W. Chen, and E. S. Moyer, *Chem. Mater.* **14**, 1845 (2002).

[15]   W. Y. Leong, C. F. Tsang, H. Y. Li, V. Bliznetsov, L. Y. Wong, and W. H. Li, *Thin Solid Films* **496**, 402 (2006).

[16]   H. Shi, J. Bao, R. S. Smith, H. Huang, J. Liu, P. S. Ho, M. L. McSwiney, M. Moinpour, and G. M. Kloster, *Appl. Phys. Lett.* **93**, 192909 (2008).

[17]   E. Vinogradova, E. Osei-Yiadom, C. E. Smith, D. W. Mueller, and R. F. Reidy, *Microelectron. Eng.* **86**, 176 (2009).

[18]   E. Vinogradova, C. E. Smith, D. W. Mueller, and R. F. Reidy, *Electrochem. Solid-State Lett.* **11**, H255 (2008).

[19]   Y. H. Wang, R. Kumar, X. Zhou, J. S. Pan, and J. W. Chai, *Thin Solid Films* **473**, 132 (2005).

[20] T. C. Chang, P. T. Liu, Y. J. Mei, Y. S. Mor, T. H. Perng, Y. L. Yang, and S. M. Sze, *J. Vac. Sci. Technol. B* **17**, 2325 (1999).

[21] H. Cui, R. J. Carter, D. L. Moore, H. G. Peng, D. W. Gidley, and P. A. Burke, *J. Appl. Phys.* **97**, 113302 (2005).

[22] D. L. Moore, R. J. Carter, H. Cui, P. Burke, S. Q. Gu, H. Peng, R. S. Valley, D. W. Gidley, C. Waldfried, and O. Escorcia, *J. Electrochem. Soc.* **152**, G528 (2005).

[23] S. K. Singh, A. A. Kumbhar, and R. O. Dusane, *Mater. Lett.* **60**, 1579 (2006).

[24] S. Xu, C. Qin, L. Diao, D. Gilbert, L. Hou, A. Wiesnoski, E. Busch, R. McGowan, B. White, and F. Weber, *J. Vac. Sci. Technol. B* **25**, 156 (2007).

[25] K. Yonekura, S. Sakamori, K. Goto, M. Matsuura, N. Fujiwara, and M. Yoneda, *J. Vac. Sci. Technol. B* **22**, 548 (2004).

[26] A. Humbert, L. Mage, C. Goldberg, K. Junker, L. Proenca, and J. B. Lhuillier, *Microelectron. Eng.* **82**, 399 (2005).

[27] M. S. Silverstein, M. Shach-Caplan, M. Khristosov, and T. Harel, *Plasma Process. Polym.* **4**, 789 (2007).

[28] K. Yonekura, K. Goto, M. Matsuura, N. Fujiwara, and K. Tsujimoto, *Jpn. J. Appl. Phys.* **44**, 2976 (2005).

[29] M. A. Goldman, D. B. Graves, G. A. Antonelli, S. P. Behera, and J. A. Kelber, *J. Appl. Phys.* **106**, 013311 (2009).

[30] X. Hua, M. S. Kuo, G. S. Oehrlein, P. Lazzeri, E. Iacob, M. Anderle, C. K. Inoki, T. S. Kuan, P. Jiang, and W. L. Wu, *J. Vac. Sci. Technol. B* **24**, 1238 (2006).

[31] K. Kurihara, T. Ono, K. Kohmura, H. Tanaka, N. Fujii, N. Hata, and T. Kikkawa, *J. Appl. Phys.* **101**, 113301 (2007).

[32] H. Nagai, S. Takashima, M. Hiramatsu, M. Hori, and T. Goto, *J. Appl. Phys.* **91**, 2615 (2002).

[33] S. Uchida, S. Takashima, M. Hori, M. Fukasawa, K. Ohshima, K. Nagahata, and T. Tatsumi, *J. Appl. Phys.* **103**, 073303 (2008).

[34] M. A. Worsley, S. F. Bent, N. C. M. Fuller, T. L. Tai, J. Doyle, M. Rothwell, and T. Dalton, *J. Appl. Phys.* **101**, 013305 (2007).

[35] A. M. Dattelbaum, M. L. Amweg, J. D. Ruiz, L. E. Ecke, A. P. Shreve, and A. N. Parikh, *J. Phys. Chem. B* **109**, 14551 (2005).

[36] Y. Ishikawa, Y. Ichihashi, S. Yamasaki, and S. Samukawa, *J. Appl. Phys.* **104**, 063308 (2008).

[37] T. Tatsumi, S. Fukuda, and S. Kadomura, *Jpn. J. Appl. Phys. Part 1* **33**, 2175 (1994).

[38] T. Yunogami, T. Mizutani, K. Suzuki, and S. Nishimatsu, *J. Appl. Phys.* **28**, 2172 (1989).

[39] D. Nest, T.-Y. Chung, D. B. Graves, S. Engelmann, R. L. Bruce, F. Weilnboeck, G, S. Oehrlein, D. Wang, C. Andes, and E. A. Hudson, *Plasma Process. Polym.* **6**, 649 (2009).

[40] Y. Kimura, Thesis, University of California, Berkeley, 2000.

[41] M. A. Goldman, Thesis, University of California, Berkeley, 2008.

[42] D. G. Nest, Thesis, University of California, Berkeley, 2009.

[43] T.-Y. Chung, Thesis, University of California, Berkeley, 2012.

[44] H. Singh, J. W. Coburn, and D. B. Graves, *J. Vac. Sci. Technol. A* **18**, 299 (2000).

[45] C.-C. Hsu, Thesis, University of California, Berkeley, 2006.

[46] M. J. Titus, Thesis, University of California, Berkeley, 2010.

[47] H. Singh and D. B. Graves, *J. Appl. Phys.* **87**, 4098 (2000).

[48] V. A. Godyak, R. B. Piejak, and B. M. Alexandrovich, *Plasma Sources Sci. Technol.* **1**, 36 (1992).

[49] S. Eslava, G. Eymery, P. Marsik, F. Iacopi, C. E. A. Kirschhock, K. Maex, J. A. Martens, and M. R. Baklanov, *J. Electrochem. Soc.* **155**, G115 (2008).

[50] C. H. Huang, H. L. Huang, C. I. Hung, N. F. Wang, Y. H. Wang, and M. P. Houng, *Jpn. J. Appl. Phys.* **47**, 1532 (2008).

[51] Y. Shioya, T. Ohdaira, R. Suzuki, Y. Seino, and K. Omote, *J. Non-Cryst. Solids* **354**, 2973 (2008).

[52] A. Zenasni, V. Jousseaume, P. Holliger, L. Favennec, O. Gourhant, P. Maury, and G. Gerbaud, *J. Appl. Phys.* **102**, 094107 (2007).

[53] H. J. Lee, E. K. Lin, H. Wang, W. L. Wu, W. Chen, and E. S. Moyer, *Chem. Mater.* **14**, 1845 (2002).

[54] E. A. Smirnov, K. Vanstreels, P. Verdonck, I. Ciofi, D. Shamiryan, M. R. Baklanov, and M. Phillips, *Jpn. J. Appl. Phys.* **50**, 05EB03 (2011).

[55] J. Yang, S. Lee, H. Park, D. Jung, and H. Chae, *J. Vac. Sci. Technol. A* **24**, 165 (2006).

[56] Q. T. Le, M. R. Baklanov, E. Kesters, A. Azioune, H. Struyf, W. Boullart, J. J. Pireaux, and S. Vanhaelemeersch, *Electrochem. Solid-State Lett*. **8**, F21 (2005).

[57] B. Jinnai, T. Nozawa, and S. Samukawa, *J. Vac. Sci. Technol. B* **26**, 1926 (2008).

[58] F. Truica-Marasescu and M. R. Wertheimer, *J. Appl. Polym. Sci.* **91**, 3886 (2004).

[59] D. M. P. Holland, D. A. Shaw, S. M. McSweeney, M. A. MacDonald, A. Hopkirk, M. A. Hayes, *Chemical Physics* **173**, 315 (1993).

[60] M. A. Worsley, S. F. Bent, S. M. Gates, N. C. M. Fuller, W. Volksen, M. Steen, and T. Dalton, *J. Vac. Sci. Technol. B* **23**, 395 (2005).

[61] E. Vella, R. Boscaino, and G. Navarra, *Phys. Rev. B* **77**, 165203 (2008).

[62] K. Awazu and H. Kawazoe, *J. Non-Cryst. Solids* **179**, 214 (1994).

[63] T. Oszinda, M. Schaller, D. Fischer, C. Walsh and S. E. Schulz, *Microelectron. Eng.* **87,** 457 (2010).

[64] H. Ren, G. A. Antonelli, Y. Nishi and J. L. Shohet, *J. Appl. Phys.* **108,** 094110 (2010).

[65] O. V. Braginsky, A. S. Kovalev, D. V. Lopaev, E. M. Malykhin, Y. A. Mankelevich, T. V. Rakhimova, A. T. Rakhimov, A. N. Vasilieva, S. M. Zyryanov and M. R. Baklanov, *J. Appl. Phys.* **108,** 073303 (2010).

[66] J. Lee and D. B. Graves, *J. Phys. D.: Appl. Phys.* **43,** 425201 (2010).

[67] S. M. Gates, G. Dubois, E. T. Ryan, A. Grill, M. Liu and D. Gidley, *J. Electrochem. Soc.* **156**, G156 (2009).

[68] M. J. Titus, D. G. Nest, T. Y. Chung and D. B. Graves, *J. Phys. D.: Appl. Phys.* **42,** 245205 (2009).

[69] Y. Kayaba , K. Kohmura and T. Kikkawa, *Jpn. J. Appl. Phys.* **47,** 8364 (2008).

[70] S. Kuroki and T. Kikkawa, *J. Electrochem. Soc.* **153,** G759 (2006).

[71] C. E. Moore, *Tables of Spectra of Hydrogen, Carbon, Nitrogen, and Oxygen Atoms and Ions.* (Boca Raton, Florida: CRC Press, 2000)

[72] W. J. Choyke, E. D. Palik, and H. R. Phillip, *Handbook of Optical Constants of Solids.* (Academic Press, San Diego, 1998)

[73] A. M. Hoyas, J. Schuhmacher, C. M. Whelan, M. R. Baklanov, L. Carbonell, J. P. Celis and K. Maex, *J. Vac. Sci. Technol. B* **23,** 1551 (2005).

[74] J. P. Booth, O. Joubert, J. Pelletier and N. Sadeghi, *J. Appl. Phys.* **69,** 618 (1991).

[75] F. Truica-Marasescu and M. R. Wertheimer, *Macromol. Chem. Phys.* **206,** 744 (2005).

[76] J. Bao, H. Shi, H. Huang, P. S. Ho, M. L. McSwiney, M. D. Goodner, M. Moinpour, and G. M. Kloster, *J. Vac. Sci. Technol. A* **28**, 207 (2010).

[77] D. Eon, V. Raballand, G. Cartry, M. C. Peignon-Fernandez, and C. Cardinaud, *Eur. Phys. J.- Appl. Phys.* **28**, 331 (2004).

[78] G. Mannaert, M. R. Baklanov, Q. T. Le, Y. Travaly, W. Boullart, S. Vanhaelemeersch, and A. M. Jonas, *J. Vac. Sci. Technol. B* **23**, 2198 (2005).

[79] J. Shoeb and M. J. Kushner, *IEEE T. Plasma Sci.* **39**, 2828 (2011).

[80] J. Shoeb, M. M. Wang, and M. J. Kushner, *J. Vac. Sci. Technol. A* **30**, 041303 (2012).

[81] J. Lee and D. B. Graves, *J. Phys. D.: Appl. Phys.* **44**, 325203 (2011).

[82] P. Verdonck, V. Šamara, A. Goodyear, A. Ferchichi, E. V. Besien, M. R. Baklanov, and N. Braithwaite, *Thin Solid Films* **520**, 464 (2011).

[83] M. A. Worsley, M. Roberts, S. F. Bent, S. M. Gates, T. Shaw, W. Volksen, and R. Miller, *Microelectron. Eng.* **82**, 113 (2005).

[84] H. Shi, H. Huang, J. Bao, J. Liu, P. S. Ho, Y. Zhou, J. T. Pender, M. D. Armacost, and D. Kyser, *J. Vac. Sci. Technol. B* **30**, 011206 (2012).

[85] F. Weilnboeck, N. Kumar, G. S. Oehrlein, T. -Y. Chung, D. Graves, M. Li, E. A. Hudson, and E. C. Benck, *J. Vac. Sci. Technol. B* **30**, 031807 (2012).

[86] H. Singh, J. W. Coburn, and D. B. Graves, *J. Appl. Phys.* **88**, 3748 (2000).

[87] C. H. Huang, N. F. Wang, Y. Z. Tsai, C. C. Liu, C. I. Hung, and M. P. Houng, *Mater. Chem. Phys.* **110**, 299 (2008).

[88] H. Yamamoto, K. Asano, K. Ishikawa, M. Sekine, H. Hayashi, I. Sakai, T. Ohiwa, K. Takeda, H. Kondo, and M. Hori, *J. Appl. Phys.* **110**, 123301 (2011).

[89] J. A. Riley and C. F. Giese, *J. Chem. Phys.* **53**, 146 (1970).

[90] T. Frot, W. Volksen, S. Purushothaman, R. Bruce, and G. Dubois, *Adv. Mater.* **23**, 2828 (2011).

[91] J. Shoeb and M. J. Kushner, *J. Vac. Sci. Technol. A* **29**, 051305 (2011).

[92] W. Puyrenier, V. Rouessac, L. Broussous, D. Rebiscoul, and A. Ayral, *Micropor. Mesopor. Mater.* **106,** 40 (2007).

[93] S. P. Behera, Q. Wang, and J. A. Kelber, *J. Phys. D.: Appl. Phys.* **44**, 155204 (2011).

[94] M. Chaudhari and J. Du, *J. Vac. Sci. Technol. A* **30**, 061302 (2012).

[95] O. V. Braginsky, A. S. Kovalev, D. V. Lopaev, E. M. Malykhin, Y. A. Mankelevich, O. V. Proshina, T. V. Rakhimova, A. T. Rakhimov, D. G. Voloshin, A. N. Vasilieva, S. M. Zyryanov, E. A. Smirnov, and M. R. Baklanov, *J. Appl. Phys.* **109**, 043303 (2011).

[96] X. Liu, S. Gill, F. Tang, S. W. King, and R. J. Nemanich, *J. Vac. Sci. Technol. B* **30**, 031212 (2012).

[97] T. Furusawa, D. Ryuzaki, R. Yoneyama, Y. Homma, and K. Hinode, *Electrochem. Solid-State Lett.* **4**, G31 (2001).

[98] E. Kunnen, M. R. Baklanov, A. Franquet, D. Shamiryan, T. V. Rakhimova, A. M. Urbanowicz, H. Struyf, and W. Boullart. *J. Vac. Sci. Technol. B* **28**, 450 (2010).

[99] J. Lee, H. Kazi, S. Gaddam, J. A. Kelber, and D. B. Graves, (submitted 2013).

[100] N. Posseme, T. Chevolleau, T. David, M. Darnon, O. Louveau, and O. Joubert, *J. Vac. Sci. Technol. B* **25**, 1928 (2007).

[101] M. Darnon, T. Chevolleau, T. David, N. Posseme, J. Ducote, C. Licitra, L. Vallier, O. Joubert, and J. Torres, *J. Vac. Sci. Technol. B* **26**, 1964 (2008).

[102] T. Czerviec, F. Greer, and D. B. Graves, *J. Phys. D: Appl. Phys.* **38**, 4278 (2005).

[103] A. Qayyu, S. Zeb, M. Naveed, S. A. Ghauri, A. Waheed, and M. Zakaullah, *Plasma Devices Oper.* **14**, 61 (2006).

[104] K. Zaima, K. Kurihara, and K. Sasaki, *Jpn. J. Appl. Phys.* **51**, 08HC02 (2012).

[105] L. Zhang, S. Zhao, and X. Meng, *Plasma Sci. Technol.* **10**, 455 (2008).

[106] K. Dressler and D. A. Ramsay, *Philos. T. Roy. Soc. A* **251,** 553 (1959).

[107] S. Leach, H.-W. Jochims, and H. Baumgartel, *Phys. Chem. Chem. Phys.* **7**, 900 (2005).

[108] S. Behera, J. Lee, S. Gaddam, S. Pokharel, J. Wilks, F. Pasquale, D. Graves, and J. A. Kelber, *Appl. Phys. Lett.* **97**, 034104 (2010).

[109] D. A. Shutov, S. Y. Kang, K. H. Baek, K. S. Suh, and K. H. Kwon, *Jpn. J. Appl. Phys.* **47**, 6970 (2008).

[110] T. C. Chang, Y. S. Mor, P. T. Liu, T. M. Tsai, C. W. Chen, Y. J. Mei, and S. M. Sze, *Thin Solid Films* **398**, 632 (2001).

[111] A. M. Urbanowicz, M. R. Baklanov, J. Heijlen, Y. Travaly, and A. Cockburn, *Electrochem. Solid-State Lett.* **10**, G76 (2007).

[112] M. Okigawa, Y. Ishikawa, and S. Samukawa. *J. Vac. Sci. Technol. B* **21**, 2448 (2003).

[113] V. E. Skurat and Y. I. Dorofeev, *Angew. Makromol. Chem.* **216**, 205 (1994).

[114] A. von Keudell, P. Awakowicz, J. Benedikt, V. Raballand, A. Yanguas-Gil, J. Opretzka, C. Flotgen, R. Reuter, L. Byelykh, H. Halfmann, K. Stapelmann, B. Denis, J. Wunderlich, P. Muranyi, F. Rossi, O. Kylian, N. Hasiwa, A. Ruiz, H. Rauscher, L. Sirghi, E. Comoy, C. Dehen, L. Challier, and J. P. Deslys, *Plasma Process. Polym.* **7**, 327 (2010).